

# The influence of radiative feedback on star-formation

in the James Clerk Maxwell Telescope Gould Belt Survey of  
nearby star-forming regions.

Damian Jack Rumble

Submitted by Mr Damian Rumble to the University of Exeter as a thesis for the degree of Doctor of Philosophy in Physics, April, 2016.

This thesis is available for Library use on the understanding that it is copyright material and that no quotation from the thesis may be published without proper acknowledgement.

I certify that all material in this thesis which is not my own work has been identified and that no material has previously been submitted and approved for the award of a degree by this or any other University.

Signed: .....

Mr D. J. Rumble

Date: .....

## **Abstract**

I aim to show that I have spent three years usefully. Or maybe four.

# Contents

<b>1</b>	<b>Introduction</b>	<b>1</b>
1.1	Content (to be sorted) . . . . .	1
1.2	Radiative Transfer Theory . . . . .	4
1.2.1	Dust . . . . .	4
1.2.2	Dust models/assumptions - opacity . . . . .	4
1.2.3	Jayliegh Jeans limit . . . . .	4
1.3	Protostars . . . . .	4
1.3.1	Jeans mass/stability . . . . .	4
1.3.2	SED models . . . . .	4
1.3.3	Classification: Alpha . . . . .	4
1.3.4	Classification: Bolometric Luminosity . . . . .	4
1.3.5	Classification: Bolometric temperature . . . . .	4
1.3.6	Classification: Colour diagrams . . . . .	4
1.3.7	Evolution/timescale: MvsL diagrams . . . . .	4
1.3.8	IMF/CMFs . . . . .	4
1.4	Radiative feedback . . . . .	4
1.4.1	OB stars . . . . .	4
1.4.2	Winds . . . . .	4
1.4.3	RDI . . . . .	4
1.4.4	HII regions . . . . .	4
1.4.5	Jets . . . . .	4
1.4.6	Radiative heating by OB stars . . . . .	4
1.5	Accretion . . . . .	4
1.5.1	Discs . . . . .	4
1.5.2	Envelopes . . . . .	4
1.6	Emission . . . . .	4
1.6.1	IR . . . . .	4
1.6.2	Submm . . . . .	4
1.6.3	Radio . . . . .	4
1.6.4	X-ray . . . . .	4
1.7	Properties . . . . .	4
1.7.1	Flux/photometry . . . . .	4

1.7.2	Mass	4
1.7.3	Column density	4
1.7.4	Volume density	4
1.7.5	Proper motion	4
1.7.6	Extinction	4
1.8	Molecular Line emission	4
1.8.1	CO	4
1.8.2	Masers	4
1.8.3	Other	4
1.9	Triggered/none triggered star formation?	4
<b>2</b>	<b>The JCMT Gould Belt Survey of star forming regions</b>	<b>5</b>
2.1	Observational astronomy	5
2.1.1	Observing in submillimetre	5
2.1.2	SCUBA-2	5
2.1.3	Data reduction	6
2.1.4	Calibration	6
2.1.5	Related surveys - 2MASS/Spitzer/Herschel	6
2.2	Data enhancement	6
2.2.1	Selection	6
2.2.2	Mosiacs	7
2.2.3	Filtering	7
2.2.4	Clumpfinding	7
2.2.5	FINDBACK	7
2.2.6	FELLWALKER	7
2.3	Statistical noise	8
2.3.1	Methods	8
2.4	GBS regions	8
2.4.1	Serpens MWC 297	10
2.4.2	Serpens South	13
2.4.3	Serpens Main	16
2.4.4	Serpens $NH_3$ and VV Ser	17
2.4.5	W40 Complex	19
2.4.6	Serpens East	19
2.4.7	Other	19
<b>3</b>	<b>CO observations of star-forming regions</b>	<b>20</b>
3.1	Introduction to CO contamination and outflows	20
3.2	HARP	20
3.3	CO reduction	20
3.4	CO observations	20
3.4.1	PPV Clouds	20

3.4.2	Outflows	20
3.5	CO contamination of SCUBA-2 850 $\mu\text{m}$	20
3.5.1	Literature	20
3.5.2	Methodology	21
3.6	Contamination in the Serpens MWC 297	21
3.7	Contamination in the the W40 complex	22
3.7.1	Cloud velocities	24
3.7.2	Outflow analysis	26
3.8	Conclusions	29
<b>4</b>	<b>Free-Free contamination</b>	<b>30</b>
4.1	Introduction to thermal breemstralung emission	30
4.2	H II observations	32
4.3	UCH II observations	33
4.3.1	Jets	35
4.4	Free-free contribution to SCUBA-2	36
4.4.1	Direct methods	36
4.4.2	Indirect methods	38
4.5	The free-free contribution in Serpens MWC 297 results and discussion.	42
4.6	The free-free contribution in the W40 complex results and discussion.	42
4.7	Conclusions	44
<b>5</b>	<b>Temperature mapping</b>	<b>46</b>
5.1	Introduction to the temperature equation	46
5.1.1	Submillimetre Flux ratio	46
5.1.2	Beta	46
5.1.3	Alpha	48
5.1.4	Temperature	48
5.2	Dual beam method	48
5.2.1	The JCMT beam (primary and secondary)	48
5.2.2	Gaussian beam convolution	48
5.2.3	4 component dual beam convolution method	49
5.3	Propagation of error	51
5.3.1	Analytical calculation	51
5.3.2	Monte-Carlo method	51
5.4	Testing Dual beam method	51
5.5	Kernel method	51
5.5.1	Convolution kernel	51
5.5.2	Beam model/beam map	51
5.5.3	Preparing the Kernel	51
5.6	Propagation of error	51
5.6.1	Monte-Carlo method	51

5.7	Testing Kernel method . . . . .	51
5.7.1	Pixel size problem . . . . .	51
5.8	Comparing ratio methods . . . . .	51
5.9	Calculating temperature . . . . .	51
5.9.1	Edge effects . . . . .	51
5.9.2	Comparison with alternative methods . . . . .	51
5.10	The impact of CO contamination . . . . .	51
5.11	The impact of the free-free contribution . . . . .	51
<b>6</b>	<b>Radiative heating in Serpens MWC 297 region</b>	<b>54</b>
6.1	Temperature maps of Serpens MWC 297 . . . . .	54
6.2	The SCUBA-2 clump catalogue . . . . .	56
6.2.1	Fellwalker parameters . . . . .	56
6.2.2	Mass . . . . .	57
6.2.3	Jeans mass . . . . .	58
6.3	The SCUBA-2 YSO catalogue . . . . .	60
6.3.1	YSO distribution . . . . .	61
6.3.2	SCUBA-2 YSOcs . . . . .	61
6.3.3	Spectral energy distributions . . . . .	65
6.3.4	YSO classification . . . . .	65
6.4	Discussion . . . . .	69
6.4.1	The state of star formation in Serpens MWC 297 . . . . .	69
6.4.2	What does SCUBA-2 tell us about the star MWC 297? . . . . .	71
6.4.3	Is there evidence for radiative feedback in Serpens MWC 297? . . . . .	72
6.5	Conclusion . . . . .	73
<b>7</b>	<b>Radiative heating in W40 Complex</b>	<b>75</b>
7.1	Temperature maps of the W40 complex . . . . .	75
7.2	The SCUBA-2 clump catalogue . . . . .	76
7.2.1	Clumpfinding analysis . . . . .	76
7.2.2	Clump Temperatures . . . . .	78
7.2.3	Clump column density and mass . . . . .	81
7.2.4	Clump Stability . . . . .	82
7.2.5	YSO distribution . . . . .	85
7.3	Discussion . . . . .	85
7.3.1	What evidence is there of radiative feedback heating the clumps in the W40 complex? . . . . .	87
7.3.2	External heating . . . . .	87
7.3.3	Internal heating . . . . .	88
7.3.4	What is the state of star-formation in the W40 complex? . . . . .	89
7.3.5	First generation star-formation . . . . .	89
7.3.6	Second generation star-formation . . . . .	91

7.3.7	What evidence is there of radiative feedback influencing star-formation in the W40 complex? . . . . .	96
7.4	Conclusion . . . . .	97
<b>8</b>	<b>Radiative heating in JCMT GBS</b>	<b>100</b>
8.1	Temperature maps of the JCMT GBS . . . . .	100
8.2	Catalogues . . . . .	100
8.2.1	OB stars . . . . .	100
8.2.2	YSO populations . . . . .	100
8.3	The SCUBA-2 clump catalogue . . . . .	100
8.3.1	Clumpfinding analysis . . . . .	100
8.3.2	Clump Temperatures . . . . .	100
8.3.3	Clump column density and mass . . . . .	100
8.3.4	Clump Stability . . . . .	100
8.3.5	YSO distribution . . . . .	100
8.4	Global analysis . . . . .	100
8.4.1	Do populations of OB stars influence clump temperature? . . . . .	100
8.4.2	Do populations of YSOs influence clump temperature? . . . . .	100
8.4.3	How do SCUBA-2 temperatures compare to Herschel temperatures? . . . . .	100
<b>9</b>	<b>Conclusions</b>	<b>101</b>
9.1	Further work . . . . .	101

# List of Figures

2.1	Plots of optical depth due to water vapour, tau, as a function of noise level of the data in the 6 component scans of MWC 297 at 450 $\mu\text{m}$ ( <i>left</i> ) and 850 $\mu\text{m}$ ( <i>right</i> ). Tau is measured at two frequencies, 225GHz ( <i>red</i> ) and 186GHz ( <i>blue</i> ). Note how the majority of points are on linear trend (within measured errors), with the exception of one scan	450
	<i>which was subsequently rejected from the final mosaic.</i>	
2.2	A visual extinction map of the whole Serpens/Aquila region derived from 2MASS data. Of particular interest are the Serpens Main and W40/Serpens South region. Note that whilst these two last regions appears as one continuous feature on this map, they are thought to be separate features (labeled respectively with the circle and star). The dashed rectangle indicates an area examined by Herschel and discussed by Bontemps et al. (2010)	7
2.3	SCUBA-2 450 $\mu\text{m}$ ( <i>left</i> ) and 850 $\mu\text{m}$ ( <i>right</i> ) data. Contours show $5\sigma$ and $15\sigma$ levels in both cases: levels are at 0.082, 0.25 Jy/ 4'' pixel and 0.011, 0.033 Jy/ 6'' pixel at 450 $\mu\text{m}$ and 850 $\mu\text{m}$ respectively. The blue outer contour shows the data reduction mask for the region, based on <i>Herschel</i> 500 $\mu\text{m}$ observations. Noise levels increase towards the edges of the map on account of the mapping method outlined in Section 2.1.	8
2.4	850 $\mu\text{m}$ greyscale map of Serpens MWC 297. Outer contours mark the data reduction mask (Figure 1) and inner contours the $3\sigma$ detection level (0.0079 Jy/pixel). Circular markers indicate the location of YSOcs as catalogued by SGBS and crosses indicate the location of SCUBA-2 confirmed YSOs (Table 6.3). YSOcs are coded by evolutionary classification based on their spectral indices ( $\alpha_{\text{IR}}$ ) in the <i>Spitzer</i> case and by bolometric temperature, $T_{\text{bol}}$ , in the SCUBA-2 case (Table 6.3). <i>Spitzer</i> YSOcs are indicated by hollow black circles (Class III), solid red circles (Class II) and green hollow circles (Class 0/I). SCUBA-2 confirmed YSOs are indicated by black crosses (Class II) and green crosses (Class 0/I). Small, solid blue circles mark the location of Damiani et al. (2006) X-ray sources, typically associated with Class II/III objects.	10
		14

2.5	left: composite image of Serpens South from IRAC wavelength; 3.6, 4.5, 8.0 $\mu\text{m}$ in blue, green and red, respectively. Right: Greyscale 8.0 $\mu\text{m}$ image overlaid with YSOs; Class I and II in red circles and green diamonds, respectively. The white circle outlines the extent of the core (?). . . . .	15
2.6	(left) Serpens Main in three-band false-colour IRAC <i>Spitzer</i> bands 3.4 $\mu\text{m}$ (blue), 4.5 $\mu\text{m}$ and 8.0 $\mu\text{m}$ . Redish hue shows diffuse PAH emission, green is typically shocked Hydrogen and more blue sections is scattered light (Winston et al., 2007). (Right) 850-greyscale and 450-contour $\mu\text{m}$ images of Serpens Main. Submillimeter continuum sources identified by Casali et al. (1993) are labeled as SMM1, etc. Cavity features due to outflows that are investigated by Davis et al. (1999) are also labeled though the central white patch here represents a depression in flux and is in fact an artefact of the reduction process. Contours in 450 $\mu\text{m}$ are set at 0.5, 1, 2, 3 and 4 (black) and 5, 10 and 20 Jy $\text{beam}^{-1}$ . The relative beam size of each map is displayed in bottom left of each image ( 14" at 850 and 8" at 450 $\mu\text{m}$ ) . . . . .	16
2.7	The 4.5 (blue), 8.0 (green), 24.0 $\mu\text{m}$ (red) colour composites of the VV Ser nebulosity by Pontoppidan et al. (2007). <i>left</i> : <i>Spitzer</i> MIPS band 1 and IRAC band 2 and 4 colour image of VV Ser. <i>right</i> : The model of the star-disk-nebulosity system produced by the above author with the same colour composite scheme . . . . .	18
3.1	$^{12}\text{CO}$ 3–2 integrated intensity map over the entire range (colour scale over -90 to +100 $\text{km s}^{-1}$ ) of the central region of the W40 complex. Contours show SCUBA-2 850 $\mu\text{m}$ emission at the 5 $\sigma$ , 15 $\sigma$ and 50 $\sigma$ levels. . . . .	23
3.2	The fraction of SCUBA-2 850 $\mu\text{m}$ that can be attributed to $^{12}\text{CO}$ 3–2 345 GHz line emission. The SCUBA-2 data are masked at 3 $\sigma$ and the 5 $\sigma$ level is shown in white. . . . .	24
3.3	The distribution of 450 $\mu\text{m}$ /850 $\mu\text{m}$ flux ratio for the original (blue - S2-4') and CO subtracted (green - S2-CO-4') Aquila reductions with additional 4' spatial filtering. KS-statistics reveal a 1.3% chance that the two data sets are drawn from the same distribution. . . . .	24
3.4	SCUBA-2 850 $\mu\text{m}$ map of the W40 complex with $^{13}\text{CO}$ 2–1 integrated intensity contours of red (10 $\text{km s}^{-1}$ ) and blueshifted (5 $\text{km s}^{-1}$ ) emission that trace out the location of two separate clouds within the region. Blue contours are at 20, 40, 60, 80 $\text{K km s}^{-1}$ and red are the same levels with an additional contour at 5 $\text{K km s}^{-1}$ . The greyscale SCUBA-2 850 $\mu\text{m}$ shown here has not had CO emission subtracted. Yellow stars mark the location of the OB stars in the W40 complex. The insert shows the line emission spectra at the position of peak SCUBA-2 luminosity, marked with a white cross. Two CO clouds are visible at 5 and 10 $\text{km s}^{-1}$ with a significant vacancy at 7 $\text{km s}^{-1}$ where Shimoikura et al. 2015 finds HCO 4–3 emission, indicating that our $^{13}\text{CO}$ 2–1 absence is due to optical depth and self-absorption. . . . .	25

3.5 2CO 32 integrated line emission in the blue wing of the $5\text{ km s}^{-1}$ (upper), and red wing of the $10\text{ km s}^{-1}$ cloud (lower). The blue $5\text{ km s}^{-1}$ wing is integrated over the velocity range $3.2 \leq v_{LSR} \leq 2.8\text{ km s}^{-1}$ . The red $10\text{ km s}^{-1}$ wing is integrated over the velocity range $11.7 \leq v_{LSR} \leq 14.5\text{ km s}^{-1}$ . Line wing sources are identified from local peaks in emission, identified as black crosses in the respective plots. Yellow stars and green circles indicate the location of the OB stars and protostars (from our composite YSO catalogue). The grayscale backdrop map is SCUBA-2 850 $\mu\text{m}$ flux density. The black, smoothed contour represents emission from the alternative line wing (see text for velocity ranges) . . . . .	27
3.6 $^{13}\text{CO}$ 2–1 line profiles of example outflows R10-6 (left) and B5-4 (right) with their locations in the 10 and $5\text{ km s}^{-1}$ clouds respectively marked in Figure E1. Each profile shows prominent outflow line-wings that are either red or blue shifted. Dotted lines demonstrate the length of the line-wing, from local cloud velocity to its maximum extent. . . . .	28
4.1 Archival VLA 21 cm NRAO VLA Sky Survey (Condon & Kaplan, 1998) continuum map of the W40 complex H II region ( $45''$ resolution). Red <i>Herschel</i> 70 $\mu\text{m}$ contours of the nebulosity SH-64 at 300, 1200, 4800, 12000 MJy/Sr. Blue SCUBA-2 850 $\mu\text{m}$ contours of the dust cloud at the $5\sigma$ level. Yellow stars indicate the locations of the OB stars, with the O9.5 star OS1 the primary ionising object of the region. The white cross indicates the peak of the VLA 21 cm emission. . . . .	32
4.2 <b>Left]</b> A schematic of the SED shape for three hypothetical scenarios offig:freefreealpha free-free emission. <b>Case a)</b> an UCH II with $\alpha_{\text{ff}} = 0.6$ has a turnover that occurs short ward of the submillimetre regime, and as a result has a majority contribution to the 850 $\mu\text{m}$ band and a significant contribution to the 450 $\mu\text{m}$ band. <b>Case b)</b> a YSO emits free-free emission, $\alpha_{\text{ff}} = 1.0$ , from a collimated jet. However the spectrum turns over to the optically thin regime long ward of submillimetre wavelengths, and consequently free-free emission contributes roughly equally to both SCUBA-2 bands. <b>Case c)</b> a H II region has free-free emission from diffuse gas of $\alpha_{\text{ff}} = -0.1$ that outshines that from compact objects at long wavelengths. However, the flat spectrum means that at submillimetre wavelengths the emission is all but negligible. <b>Right]</b> Free-free turnover as a function of launching electron density (as described by Olmon 1975 in Equation 4.15). Dashed lines indicate the submillimetre regime (1.3 mm to 350 $\mu\text{m}$ ). . . . .	34
4.3 Archival AUI/NRAO 3.6 cm map of the W40 complex OB association (NRAO/VLA Archive Survey, (c) 2005-2007). SCUBA-2 850 $\mu\text{m}$ contours of dust emission at $5\sigma$ , $15\sigma$ and $50\sigma$ overlaid. Yellow markers indicate the locations of the OB stars while cyan circles indicate the location of compact radio sources identified by Rodriguez et al 2010. Cyan crosses mark the four peaks identified separately in the AUI/NRAO 3.6 cm map. . . . .	35

---

4.4	The Spectral Energy Distribution of MWC 297 from submillimetre to radio wavelengths. SCUBA-2 fluxes (found using aperture photometry as described in Section 5.2.) are presented alongside those collated by Sandell et al. (2011) who fit a power law $\alpha = 1.03 \pm 0.02$ , consistent with free-free emission from an UCHII region and polar jets or outflows. . . . .	36
4.5	IR1 SCUBA-2 850 $\mu\text{m}$ data before <i>left</i> and after <i>right</i> removal of free-free contamination from an UCHII region and polar jets/winds (represented by the point source contours in the <i>left</i> plot). SCUBA-2 contours are at 0.011, 0.022, 0.033 and 0.055 Jy/pixel (corresponding to 5, 10, 15 and 25 $\sigma$ detection limits). 6 cm VLA contours (red) from Sandell (private comm.) at 0.002, 0.005, 0.02, 0.072, 0.083 Jy/beam are overlaid on the left hand panel. The location of MWC 297 is marked with a star. Beam sizes are shown at the bottom of the image (VLA CnD config. <i>left</i> and JCMT <i>right</i> ). . . . .	37
4.6	The free-free contribution from large-scale H II gas, modelled using archival VLA 21 cm observations (Condon & Kaplan, 1998) assuming $\alpha_{\text{ff}} = -0.1$ (right), compared to SCUBA-2 dust emission at 850 $\mu\text{m}$ (left). Maps have common 15'' pixels and 45'' resolution. Markers indicate the locations of the OB stars. . . . .	38
4.7	The free-free contribution of compact radio sources OS1a and OS2a at 450 $\mu\text{m}$ (left) and 850 $\mu\text{m}$ (right), modelled as point sources extrapolated from the Rodriguez et al. 2010 3.6 cm fluxes with assumed spectral indices given in Table 4.3. Yellow markers with thick outlines indicate the locations of the OB stars, cyan circles the location of all the Rodriguez et al. 2010 compact radio sources and cyan crosses the location of four peaks identified separately in the AUI/NRAO 3.6 cm map (450 $\mu\text{m}$ only). Black contours trace SCUBA-2 data at 3 $\sigma$ , 5 $\sigma$ , 15 $\sigma$ and 30 $\sigma$ . Red and green filled contours trace the free-free contribution at 3 $\sigma$ and 5 $\sigma$ from optically thick (see Table 4.1). . . . .	39
4.8	Modelling free-free emission in OS2a from the Rodriguez et al. (2010) 3.6 cm data for a given $\alpha_{\text{ff}} = 0.6$ (red), 1.0 (green), and the observed dust spectral index (black). . . . .	41
5.1	Flux ratio as a function of temperature as described by Equation 5.1. The temperature range is that commonly observed in protostellar cores. . . . .	47
5.2	Temperature maps of MWC 297 from the ratio of 450 $\mu\text{m}$ and 850 $\mu\text{m}$ emission pre ( <i>left</i> ) and post ( <i>right</i> ) free-free contamination subtraction. Contours are at 11, 25 and 38 K. The location of MWC 297 is marked with a star. . . . .	51
5.3	Temperature maps of MWC 297 from the ratio of 450 $\mu\text{m}$ and 850 $\mu\text{m}$ emission pre ( <i>left</i> ) and post ( <i>right</i> ) free-free contamination subtraction. Contours are at 11, 25 and 38 K. The location of MWC 297 is marked with a star. . . . .	52

---

5.4 IR1 SCUBA-2 850 $\mu\text{m}$ data before <i>left</i> and after <i>right</i> removal of free-free contamination from an UCHII region and polar jets/winds (represented by the point source contours in the <i>left</i> plot). SCUBA-2 contours are at 0.011, 0.022, 0.033 and 0.055 Jy/pixel (corresponding to 5, 10, 15 and 25 $\sigma$ detection limits). 6 cm VLA contours (red) from Sandell (private comm.) at 0.002, 0.005, 0.02, 0.072, 0.083 Jy/beam are overlaid on the left hand panel. The location of MWC 297 is marked with a star. Beam sizes are shown at the bottom of the image (VLA CnD config. <i>left</i> and JCMT <i>right</i> ). . . . . .	53
6.1 Top to bottom: a) SCUBA-2 convolved 850 $\mu\text{m}$ flux map of Serpens MWC 297. Contours from the original 850 $\mu\text{m}$ data are at 0.011, 0.033 Jy/pixel (corresponding to 5 and 15 $\sigma$ ). b) SCUBA-2 convolved and aligned 450 $\mu\text{m}$ flux map of Serpens MWC 297 in Jy/pixel. Contours from the original 450 $\mu\text{m}$ data are at 0.082, 0.25 Jy/pixel (corresponding to 5 and 15 $\sigma$ ). The crosses in a) and b) mark the location of the ZAMS B1.5Ve star MWC 297 and its binary partner OSCA (A2v). c) Dust temperature map of Serpens MWC 297 for $\beta = 1.8$ . Contours of <i>Spitzer</i> 24 $\mu\text{m}$ emission at 32, 40 and 70 MJy per Sr are overlaid. . . . .	55
6.2 Jeans stability plotted against Jeans length. All clumps with $M_{850}/M_J > 1$ , as shown by the dashed line, are expected to be undergoing collapse. Blue circles represent calculations made with real temperature data whereas red crosses indicate those made with an assumed temperature of 15 K. Systematic error in the measurement of distance to MWC 297 accounts for 20 per cent uncertainty on Jeans length. . . . .	58
6.3 Comparison of flux emission from FELLWALKER objects at 450 $\mu\text{m}$ (contours), 850 $\mu\text{m}$ (greyscale) and the SGBS YSOcs (markers). Numbers in square brackets correspond to the objects in Table 6.1. Maps show contours of 450 $\mu\text{m}$ submillimetre flux at 5, 10, 20 and 30 $\sigma$ ( $\sigma = 0.016$ Jy/pixel). <i>Spitzer</i> YSOcs are indicated by hollow black circles (Class III), solid red circles (Class II) and green hollow circles (Class 0/I). The star indicates the location of the star MWC 297. . . . .	63
6.4 Submillimetre clumps in Serpens MWC 297 as identified by the FELLWALKER clump-finding algorithm. Numbers in square brackets correspond to the objects in Table 6.1. Maps show contours of 850 $\mu\text{m}$ submillimetre flux at 5, 10, 20 and 30 $\sigma$ ( $\sigma = 0.0022$ Jy/pixel) up to the position of peak flux (black cross). The aperture from which SED flux density was calculated is plotted as the scale size of a protostellar core (0.05 pc). Temperature is shown where it is statistically significant and is used to calculate the masses shown in Table 6.3. <i>Spitzer</i> YSOcs are indicated by hollow black circles (Class III), solid red circles (Class II) and green hollow circles (Class 0/I). The star indicates the location of the star MWC 297. . . . .	63

6.5	Spectral Energy Distributions for YSOcs associated with <b>FELLWALKER</b> clumps (Table 6.3). Blue points represent archive data sourced from <i>Spitzer</i> and 2MASS. Red points show new data provided by SCUBA-2 at 450 $\mu\text{m}$ and 850 $\mu\text{m}$ (note that the star MWC 297 was not identified by <b>FELLWALKER</b> after free-free contamination was accounted for). The straight line in MWC 297 describes free-free emission from an UCHII region and polar jet/wind with a spectral index $\alpha=1.03$ . . . . .	66
6.6	Bolometric temperature plotted against $L_{\text{smm}}/L_{\text{bol}}$ ( <i>left</i> ) and $\alpha_{\text{IR}}$ ( <i>right</i> ) for the 10 YSOcs listed in Table 6.3. Dashed lines indicate the boundaries of classification of objects (greyed boxes indicating regions of class space where methods agree).	69
7.1	Temperature map of the W40 complex with <i>Herschel</i> 70 $\mu\text{m}$ contours at 300, 1200, 4800 and 12000 MJy/Sr. . . . .	77
7.2	Clumps identified in the SCUBA-2 CO subtracted, 4' filtered and free-free subtracted 850 $\mu\text{m}$ data using the Starlink clump-finding algorithm <b>fellwalker</b> . Clumps are indexed in order of highest to lowest flux density which matches the order presented in Tables 7.1 and 7.2. . . . .	78
7.3	Histograms of the properties of clumps within the W40 complex. Top left) describes mass segregation, top right) column density segregation, bottom left) temperature distribution of clumps and bottom right) Jeans stability of clumps. Total height of bars includes the full set of clumps. Blue is a subset of clumps that have real, calculated temperature, yellow is further subset of clumps with real temperature and at least one YSO present within the body of the cloud. Red bars show those clumps where no temperature data is available therefore a value of $15\pm2$ K (Rumble et al., 2015) has been assumed for the purpose of these calculations. . .	79
7.4	SCUBA-2 column density map of the major parts of the W40 complex. Prepared using temperature maps presenting in Figure 7.1 for a constant $\beta = 1.8$ . Contours describe YSO surface density with levels at 20, 60, 110, 160 and 210 YSO pc $^2$ . .	83
7.5	<i>Herschel</i> 70 $\mu\text{m}$ flux density map of the W40 complex. Morphological features of W40-N and the Dust Arc are labelled along side major clumps detected in SCUBA-2 850 $\mu\text{m}$ emission (see Figure 7.2 for accurate clumps positions). Black contours show SCUBA-2 850 $\mu\text{m}$ at the $5\sigma$ and $50\sigma$ level. Red contours show HARP $^{12}\text{CO}$ 3–2 redshifted ( $10.5 \text{ km s}^{-1}$ ) emission at 5, 25 and 75 K km s $^{-1}$ . White contours show archival VLA 21 cm emission at $5\sigma$ and $25\sigma$ (Condon & Kaplan, 1998). . . . .	86
7.6	Plots describing clump temperature as a function of; top) distance, in pc, to OS1a, the most powerful star in the W40 complex, middle) mean VLA 21 cm flux detected in the area of each clump and bottom) YSO surface density. Circle markers indicate that that clump has at least one YSO detected within it. . . . .	88

7.7 SCUBA-2 850 $\mu\text{m}$ flux density map. The 4 OB stars OS1a, 2a, 3a and IRS 5 are marked in yellow. YSOcs from our composite catalogue are displayed. OB stars are marked in yellow, protostars (Class 0/I) are marked as green and PMS-stars (Class II/III) are marked as red. The black contour indicates the $5\sigma$ level of the SCUBA-2 850 $\mu\text{m}$ flux. The FWHM of the YSO surface density (an effective size of the stellar cluster) is also shown. . . . .	91
7.8 Archival Herschel 70 $\mu\text{m}$ data. Magenta contours (560, 570, 580, 590, 600, 610, 620 mag.) show a number of 2MASS point sources embedded within the eastern Dust Arc (shown in the yellow SCUBA-2 850 $\mu\text{m}$ 5, 10, 20, 40, 60, 80 $\sigma$ contours with circle markers at the peaks of the W40-SMM1 and 5 clumps). Cyan crosses show the four peaks in Archival AUI/NRAO 3.6 cm map (contours at 0.01, 0.016 and 0.021 Jy/beam). The Rodriguez et al. 2010 YSO ‘VLA3’ is also shown. . . . .	93
7.9 Jeans stability as a function of column density. Exterior periphery clumps (defined as having a mean <i>Herschel</i> 70 $\mu\text{m}$ flux of less than 1000 MJy/Sr) are marked in blue, interior clumps within the nebulosity SH2-64 are marked in red. The unweighted linear regression fit to each population is marked as a line of the same colour. . . . .	95

## List of Tables

2.1	Results of analysis of ratio of protostars to pre-main sequence stars for the whole maps and the core region, defined by an arbitrary flux level. [UPDATE] . . . . .	10
2.2	A sample of <i>Spitzer</i> YSO candidates (YSOc) from the SGBS. The full version appears as supplementary material online. . . . .	12
2.3	YSO candidates in the MWC 297 region. . . . .	13
4.1	Summary of radio findings on bright objects in W40. . . . .	39
4.2	Summary of free-free contributions to SCUBA-2 wavelengths from MWC 297. The uncertainty on flux density at 450 $\mu$ m is 0.03 Jy and 850 $\mu$ m is 0.0025 Jy. . . . .	42
4.3	Summary of free-free contributions to SCUBA-2 wavelengths from bright objects in W40. The uncertainty on flux density at 450 $\mu$ m is 0.017 Jy and 850 $\mu$ m is 0.0025 Jy. . . . .	43
6.1	Properties of submillimetre clumps in MWC 297. . . . .	59
6.2	Ratios of protostars (Class 0, I, FS) to PMS stars (Class II, TD, III) in the SGBS and SCUBA-2 catalogue . . . . .	61
6.3	Properties of YSO candidates in MWC 297. . . . .	63
6.4	SCUBA-2 40'' aperture fluxes for the <i>Spitzer</i> YSOc listed in Table 2.2. A full version of this catalogue is available online. . . . .	64
7.1	A sample of submillimetre clumps and their respective SCUBA-2 and <i>Herschel</i> fluxes. The full table is available online. . . . .	76
7.2	The properties of a sample of submillimetre clumps in the W40 complex. The full table is available online. . . . .	80
7.3	Dense cores in the W40 complex. . . . .	84

## **Declaration**

This thesis contains work published or pending publication as papers. Honest.

# Acknowledgements

Hey.

Thanks.

ME  
Exeter, U.K.  
??<sup>th</sup> September 200?

# 1

## Introduction

### 1.1 Content (to be sorted)

The temperature of gas and dust in dense, star-forming clouds is vital in determining whether or not clumps undergo collapse and potentially form stars (Jeans, 1902). Dense clouds can be heated by a number of mechanisms: heating from the interstellar radiation field (ISRF) (Mathis et al., 1983; Shirley et al., 2000, 2002), evolved OB stars with HII regions (Koenig et al., 2008; Deharveng et al., 2012) or strong stellar winds (Canto et al., 1984; Ziener & Eislöffel, 1999; Malbet et al., 2007); and internally through gravitational collapse of the Young Stellar Object (YSO) and accretion onto its surface (Calvet & Gullbring, 1998). Radiative feedback is thought to play an important role in the formation of the most massive stars through the suppression of core fragmentation (Bate, 2009; Offner et al., 2009; Hennebelle & Chabrier, 2011). The temperature of star-forming regions has been observed and calculated using a variety of different methods and data. Some methods utilise line emission from the clouds: for example, Ladd et al. (1994) and Curtis et al. (2010) examine the CO excitation temperature and Huttemeister et al. (1993) looked at a multilevel study of ammonia lines. Often temperature assumptions are made in line with models of Jeans instability and Bonnor-Ebert Spheres (Ebert, 1955; Bonnor, 1956; Johnstone et al., 2000). An alternative method is to fit a single temperature greybody model to an observed Spectral Energy Distribution (SED) of dust continuum emission for the YSO (Hildebrand, 1983); however, this method is sensitive to the completeness of the spectrum, the emission models and local fluctuations in dust properties (Könyves et al., 2010; Bontemps et al., 2010). Where multiple submillimetre observations exist, low temperatures (less than 20 K), which favour cloud collapse, can be inferred by the relative intensity of longer wavelengths over shorter wavelengths. For example, *Herschel* provides FIR and submillimetre data through PACS bands 70  $\mu\text{m}$ , 100  $\mu\text{m}$  and

160  $\mu\text{m}$  and SPIRE bands 250  $\mu\text{m}$ , 350  $\mu\text{m}$  and 500  $\mu\text{m}$  (Pilbratt et al., 2010). Men'shchikov et al. (2010); André et al. (2010) use *Herschel* data to construct a low resolution temperature map for the Aquila and Polaris region through fitting a greybody to dust continuum fluxes (an opacity-modified blackbody spectrum). *Herschel* data offers five bands of FIR and submillimetre observations and low noise levels; however, it lacks the resolution of the JCMT which can study structure on a scale of 7.9''(450  $\mu\text{m}$ ) and 13.0''(850  $\mu\text{m}$ ) (Dempsey et al., 2013) as opposed to 25.0'' and larger for 350  $\mu\text{m}$  or greater submillimetre wavelengths. Sadavoy et al. (2013) combine *Herschel* and SCUBA-2 data to constrain both  $\beta$  and temperature. This work develops a method which takes the ratio of fluxes at submillimetre wavelengths when insufficient data points exist to construct a complete SED. The ratio method allows the constraint of temperature or  $\beta$ , but not both simultaneously. Throughout this paper we used a fixed  $\beta$ . The value and justification for this are discussed in Section 3. Similar methods have been applied by Wood et al. (1994), Arce & Goodman (1999) and Font et al. (2001) and used by Kraemer et al. (2003) at 12.5  $\mu\text{m}$  and 20.6  $\mu\text{m}$  and by Schnee et al. (2005) at 60  $\mu\text{m}$  and 100  $\mu\text{m}$ . Mitchell et al. (2001) first used 450  $\mu\text{m}$  and 850  $\mu\text{m}$  fluxes from SCUBA, though full analysis was limited by the quality and quantity of 450  $\mu\text{m}$  data. A more rigorous analysis of SCUBA data was completed by Reid & Wilson (2005) who are able to constrain errors on the temperature maps from sky opacity and the error beam components. Most recently similar methods have been used by Hatchell et al. (2013) to analyse heating in NGC1333. This work looks to utilise these methods to further investigate radiative feedback in star-forming regions.



## 1.2 Radiative Transfer Theory

1.2.1 Dust

1.2.2 Dust models/assumptions - opacity

1.2.3 Jayliegh Jeans limit

## 1.3 Protostars

1.3.1 Jeans mass/stability

1.3.2 SED models

1.3.3 Classification: Alpha

1.3.4 Classification: Bolometric Luminosity

1.3.5 Classification: Bolometric temperature

1.3.6 Classification: Colour diagrams

1.3.7 Evolution/timescale: MvsL diagrams

1.3.8 IMF/CMFs

## 1.4 Radiative feedback

1.4.1 OB stars

1.4.2 Winds

1.4.3 RDI

1.4.4 HII regions

1.4.5 Jets

1.4.6 Radiative heating by OB stars

## 1.5 Accretion

1.5.1 Discs

1.5.2 Envelopes

## 1.6 Emission

1.6.1 IR

1.6.2 Submm

1.6.3 Radio

1.6.4 X-ray

## 1.7 Properties

# 2

## The JCMT Gould Belt Survey of star forming regions

### 2.1 Observational astronomy

#### 2.1.1 Observing in submillimetre

#### 2.1.2 SCUBA-2

Our work builds on analytical techniques developed for SCUBA data (Johnstone et al., 2000; Kirk et al., 2006; Sadavoy et al., 2010) to analyse SCUBA-2 data at the same wavelengths. SCUBA-2 represents a significant improvement over its predecessor as it has an array of 10,000 pixels, as opposed to 128. Practically this gives the instrument a much wider field of view and allows larger regions to be observed quicker and to greater depth. Restricted to SCUBA, larger regions of star formation, for example Orion (Nutter & Ward-Thompson, 2007) and Perseus (Hatchell et al., 2007), were prioritised over the low mass Serpens MWC 297 region.

The JCMT GBS extends the coverage of the local star-forming regions over those mapped by SCUBA. SCUBA-2 also offers much greater quality and quantity of 450  $\mu\text{m}$  data, as a result of improved array technology and reduction techniques pioneered by Holland et al. (2006, 2013), Dempsey et al. (2013) and Chapin et al. (2013). Mitchell et al. (2001) is able to construct partial temperature maps from SCUBA 450  $\mu\text{m}$  and 850  $\mu\text{m}$  data but is limited to general statements about the region as a result of high noise estimates at 450  $\mu\text{m}$ . Reid & Wilson (2005) go further in their use of 450  $\mu\text{m}$  data to analyse clump temperature but only obtain results for 54 per cent of the clumps they detect in 850  $\mu\text{m}$ . Calculated temperatures become increasingly unreliable at higher values to the extent they can only define a lower limit of 30 K for temperatures above this value.

The lower noise levels and wider coverage at 450  $\mu\text{m}$  from SCUBA-2 offer improved quality and quantity to the extent that temperature maps can be constructed for many features in star-forming regions.

### 2.1.3 Data reduction

The data were reduced using an iterative map-making technique (`makemap` in `SMURF`, Chapin et al. 2013, Jenness et al. 2013), and gridded to 6'' pixels at 850  $\mu\text{m}$ , 4'' pixels at 450  $\mu\text{m}$ . The iterations were halted when the map pixels, on average, changed by <0.1 per cent of the estimated map rms. The initial reductions of each individual scan were coadded to form a mosaic from which a signal-to-noise mask was produced for each region. This was combined with *Herschel* 500  $\mu\text{m}$  emission at greater than 2 Jy/beam to include all potential emission regions. The final mosaic was produced from a second reduction using this mask to define areas of emission. Detection of emission structure and calibration accuracy are robust within the masked regions, and are uncertain outside of the masked region. A spatial filter of 600'' is used in the reduction, which means that flux recovery is robust for sources with a Gaussian Full Width Half Maximum (FWHM) less than 2.5'. Sources between 2.5' and 7.5' will be detected, but both the flux and the size are underestimated because Fourier components with scales greater than 5' are removed by the filtering process. Detection of sources larger than 7.5' is dependent on the mask used for reduction. The data presented in Figure 2.3 are initially calibrated in units of pW and are converted to Jy per pixel using Flux Conversion Factors (FCFs) derived by Dempsey et al. (2013) from the average values of JCMT calibrators. By correcting for the pixel area, it is possible to convert maps of units Jy/pixel to Jy/beam using

$$S_{\text{beam}} = S_{\text{pixel}} \frac{\text{FCF}_{\text{peak}}}{\text{FCF}_{\text{arcsec}}} \frac{1}{\text{Pixel area}}. \quad (2.1)$$

$\text{FCF}_{\text{arcsec}} = 2.34 \pm 0.08$  and  $4.71 \pm 0.5$  Jy/pW/arcsec<sup>2</sup>, at 850  $\mu\text{m}$  and 450  $\mu\text{m}$  respectively, and  $\text{FCF}_{\text{peak}} = 537 \pm 26$  and  $491 \pm 67$  Jy/pW at 850  $\mu\text{m}$  and 450  $\mu\text{m}$  respectively. The PONG scan pattern leads to lower noise in the map centre and overlap regions, while data reduction and emission artefacts can lead to small variations in the noise over the whole map.

### 2.1.4 Calibration

#### 2.1.5 Related surveys - 2MASS/Spitzer/Herschel

## 2.2 Data enhancement

### 2.2.1 Selection

Of the six scans observed, three were selected for the final mosaics at each wavelength. This selection reflects a number of factors. In one case observed flaws were attributed to bolometer failures in one 850  $\mu\text{m}$  case and weather conditions where the opacity was significantly off trend in both  $\tau_{225}$  and  $\tau_{186}$  bands for a 450  $\mu\text{m}$  case (Figure 2.1). Both scans were removed. A perceived ‘temperature gradient’ remained in the preliminary results and was unexplained by contemporary understanding of star formation. We devised a test for reliability of the data, comparing a pixel

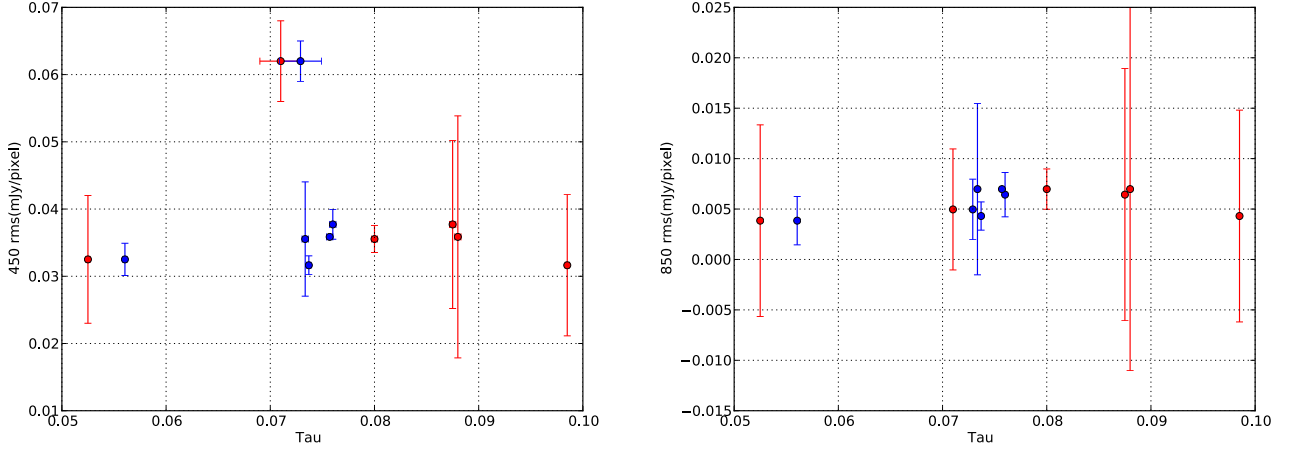


Figure 2.1: Plots of optical depth due to water vapour,  $\tau$ , as a function of noise level of the data in the 6 component scans of MWC 297 at  $450\text{ }\mu\text{m}$  (left) and  $850\text{ }\mu\text{m}$  (right).  $\tau$  is measured at two frequencies, 225GHz (red) and 186GHz (blue). Note how the majority of points are on linear trend (within measured errors), with the exception of one scan 450 which was subsequently rejected from the final mosaic.

in one scan to the mean of the remaining five. Where this pixel was greater than three standard deviations from the mean it was flagged as ‘anomalous’. Typical fraction of anomalies due to statistical noise within the data reduction masks of MWC 297 region were *3percent* and *6percent* for  $450\text{ }\mu\text{m}$  and  $850\text{ }\mu\text{m}$ . Two out of five scans were rejected from  $450\text{ }\mu\text{m}$  with fractions of *7percent* and *10percent* and two out of five scans were rejected from  $850\text{ }\mu\text{m}$  with fractions of *17percent* and *50percent*. The omission of half of the components has a none negligible effect on the background  $1\sigma$  noise level of the maps, causing it to increase from  $16.8/2.18$  to  $20.9/2.62$  mJy per  $4''/6''$  pixel,  $450\text{ }\mu\text{m}/850\text{ }\mu\text{m}$  respectively.

### 2.2.2 Mosaics

### 2.2.3 Filtering

### 2.2.4 Clumpfinding

### 2.2.5 FINDBACK

### 2.2.6 FELLWALKER

Clumps do not have well defined boundaries within the ISM. We use the signal to noise ratio to define a boundary at an *effective radius*. The boundary is determined by the STARLINK CUPID package for the detection and analysis of objects (Berry et al., 2013), specifically the FELLWALKER algorithm which assigns pixels to a given region based on positive gradient towards a common emission peak. This method has greater consistency over parameter space than other algorithms (Watson 2010, Berry (2014)). FELLWALKER was developed by Berry et al. (2007), and the 2D version of the algorithm used here considers a pixel in the data above the noise level parameter and then

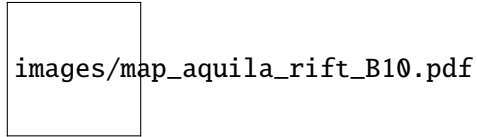


Figure 2.2: A visual extinction map of the whole Serpens/Aquila region derived from 2MASS data. Of particular interest are the Serpens Main and W40/Serpens South region. Note that whilst these two last regions appears as one continuous feature on this map, they are thought to be separate features (labeled respectively with the circle and star). The dashed rectangle indicates an area examined by Herschel and discussed by Bontemps et al. (2010)

compares its value to the adjacent pixels. FELLWALKER then moves on to the adjacent pixel which provides the greatest positive gradient. This process continues until the peak is reached - when this happens all the pixels in the ‘route’ are assigned an index and the algorithm is repeated with a new pixel. All ‘routes’ that reach the same peak are assigned the same index and form the ‘clump’. Clump-finding algorithms, such as this, have been used by Johnstone et al. (2000), Hatchell et al. (2005), Kirk et al. (2006) and Hatchell et al. (2007) to define the extent of clumps for the purposes of measuring clump mass.

## 2.3 Statistical noise

### 2.3.1 Methods

## 2.4 GBS regions

This study uses data from the JCMT Gould Belt Survey (GBS) of nearby star-forming regions (Ward-Thompson et al., 2007). The survey maps all major low and intermediate-mass star-forming regions within 0.5 kpc. The JCMT GBS provides some of the deepest maps of star forming regions where  $A_v > 3$  with a target sensitivity of  $3 \text{ mJy beam}^{-1}$  at  $850 \mu\text{m}$  and  $12 \text{ mJy beam}^{-1}$  at  $450 \mu\text{m}$ . The improved resolution of the JCMT also allows for more detailed study of large scale structures such as filaments, protostellar envelopes, extended cloud structure and morphology down to the Jeans length.

In this section, the basic properties of each region are presented and studies at a variety of wavelengths are discussed to highlight the diversity of astrophysics in the Aquila-rift. This is an elongated region of extinction at  $l = 28^\circ$ . Studies by Straizys et al. (2003) have calculated a distance of  $225 \pm 55 \text{ pc}$  for the ‘extinction wall’ of the region. The rift itself is a vast dust feature spanning approximately  $5^\circ$  in length and is clearly visible in figure 2.2 (Bontemps et al., 2010).

Serpens Main, Ammonia and South are vast, complex systems with filaments and well defined core regions within the clouds. Star formation here is thought to have started from the spontaneous collapse of the molecular clouds under gravity - hereby referred to as ‘classical’ star formation. It is fairly ubiquitous that these regions contain a core region of the most dense, cold gas with filaments off shoots. These regions are grouped such that they do not feature isolated collapse or obvious previous generations of stars that may be influencing the environment from which they are formed, for example with a Photo-Dissociative region (PDR).

W40, MWC297 and VV Ser regions of Serpens-Aquila are smaller and fundamentally different to the classical star forming regions. That is to say each region is synonymous with some existing MS stars which have recently formed from the natal cloud and are thought to be in some-way influencing star formation in the region. MWC297 and VV Ser contain isolated, young MS or Zero Age Main Sequence (ZAMS) stars. W40 contains a developed OB association of 3 ionising stars which are responsible for a large DPR. Together they are designated as potentially '*triggered*' star forming regions.

The rift is the common cloud that Serpens Main, Ammonia and VV Ser are all part of, therefore the distance of  $225 \pm 55$  pc is carried through for the distance to Serpens South as the regions are physically connected, Figure ?? shows the regions in relation to each other. In addition to this, South also has similar Local Standard of Rest velocity ( $6 \text{ km}^{-1}$ ) as Main and  $NH_3$  (?). Observations of Serpens South are complicated by the presence of W40 which is projected on the same part of the sky as South. There has been considerable debate over its distance of W40 relative to South. From this point on it is assumed that W40 is at a distance of 600 pc and is therefore not physically connected to South.

Finally, other notable regions of Serpens-Aquila are discussed, namely this is a poorly studied Eastern region. [EXPAND AND INCLUDE N]

I summarise the regions here.

- **Serpens Main** is located approximately  $\alpha: 18 29 55 \delta: +01 13 00$  (Galactic coordinates  $l = 32^\circ$  and  $b = 5^\circ$ ) at a distance of  $230 \pm 20$  ps (Eiroa et al., 2008) with an approximate depth of 80 pc.
- **Serpens Ammonia** (from now on  $NH_3$ ) is located  $45'$  to the south of Serpens Main (Djupvik et al., 2006) and is undergoing many similar star formation processes to its 'sister' region to the north.
- **Serpens South** is one half of the Aquila-Rift Molecular cloud complex located at approximately  $\alpha: 18 30 03, \delta: -02 01 58.2$  ( $l = 28^\circ$  and  $b = 5^\circ$ ). It is located approximately  $3^\circ$  south of the previous discuss Serpens Main region.
- **W40** is coincident with Serpens South and is composed of three components; a large cold molecular cloud, a powerful HII region (S2-64) driven by a three star OB association and a embedded stellar cluster.
- **Serpens MWC 297** is an important, isolated intermediate mass ZAMS star to the south east of W40 at  $\alpha: 18 27 40.6 \delta: -03 50 11$ .
- **Serpens East** is the most prominent of several smaller eastern regions located approximately  $\alpha: 18 37 30 \delta: -01 40 00$ .
- **Serpens North** is the most prominent of several smaller eastern regions located approximately  $\alpha: 18 37 30 \delta: -01 40 00$ .

Spatial distribution has been analysed by various authors for various regions through the means of a quantifiable ratio between the number of PMS to protostars in a given part of the cloud, for example, the core. Here I conduct a similar analysis, the results of which are shown in Table 2.1. Ratios are calculated for the entire map as a control and then for two different sized cores. These areas are shown on the YSO maps for each region above as the blue dotted and solid lines. Each area is defined by an arbitrary flux level such that a sensible core region is defined. There is a mixed bag of results to compare this directly to as some areas have been studied in this fashion whereas others have not and there are few limits places on the boundary conditions. The results obtained here will be discussed relative to the literature results in the discussion section with the main focus being on trends as opposed to actual data.

Region	Whole map	0.03Jy per beam	0.1Jy per beam	0.25Jy per beam	0.3Jy per beam
Main	0.26	-	0.92	1.62	-
$NH_3$	0.13	-	1.13	7.00	-
South		5.70	-	-	19.00
MWC297	0.10	-	n/a	0.40	-

Table 2.1: Results of analysis of ratio of protostars to pre-main sequence stars for the whole maps and the core region, defined by an arbitrary flux level. [UPDATE]

#### 2.4.1 Serpens MWC 297

Serpens MWC 297 region is a region of low mass star formation associated with the B star MWC 297 and considered to be part of the larger Serpens-Aquila star forming complex (Figure 2.3).

Serpens MWC 297 was observed with SCUBA-2 (Holland et al., 2013) on the 5th and 8th of July 2012 as part of the JCMT Gould Belt Survey (GBS, Ward-Thompson et al. 2007) MJLSG33 SCUBA-2 Serpens Campaign (Holland et al., 2013). One scan was taken on the 5th at 12:55 UT in good Band 2 with 225 GHz opacity  $\tau_{225} = 0.04 - 0.06$ . Five further scans taken on the 8th between 07:23 and 11:31 UT in poor Band 2,  $\tau_{225} = 0.07 - 0.11$ . Continuum observations at 850  $\mu$ m and 450  $\mu$ m were made using fully sampled 30' diameter circular regions (PONG1800 mapping mode, Chapin et al. 2013) centered on RA(J2000) =  $18^h 28^m 13^s.8$ , Dec. (J2000) =  $-03^\circ 44' 1.7''$ . Typical noise levels were 0.0165 and 0.0022 Jy per pixel at 450  $\mu$ m and 850  $\mu$ m respectively.

The exact distance to the star MWC 297 is a matter of debate. Preliminary estimates of the distance to the star were put at 450 pc by Canto et al. (1984) and  $530 \pm 70$  pc by Bergner et al. (1988). Drew et al. (1997) used a revised spectral class of B1.5Ve to calculate a closer distance of  $250 \pm 50$  pc which is in line with the value of  $225 \pm 55$  pc derived by Straizys et al. (2003) for the minimum distance to the extinction wall of the whole Serpens-Aquila rift of which the star MWC 297 is thought to be a part. The distance to the Serpens-Aquila rift was originally put at a distance of  $250 \pm 50$  pc due to association with Serpens Main, a well constrained star forming region the north of MWC 297; however, recent work by Dzib et al. (2010, 2011) has placed Serpens Main at  $429 \pm 2$  pc using parallax. Maury et al. (2011) argues that previous methods

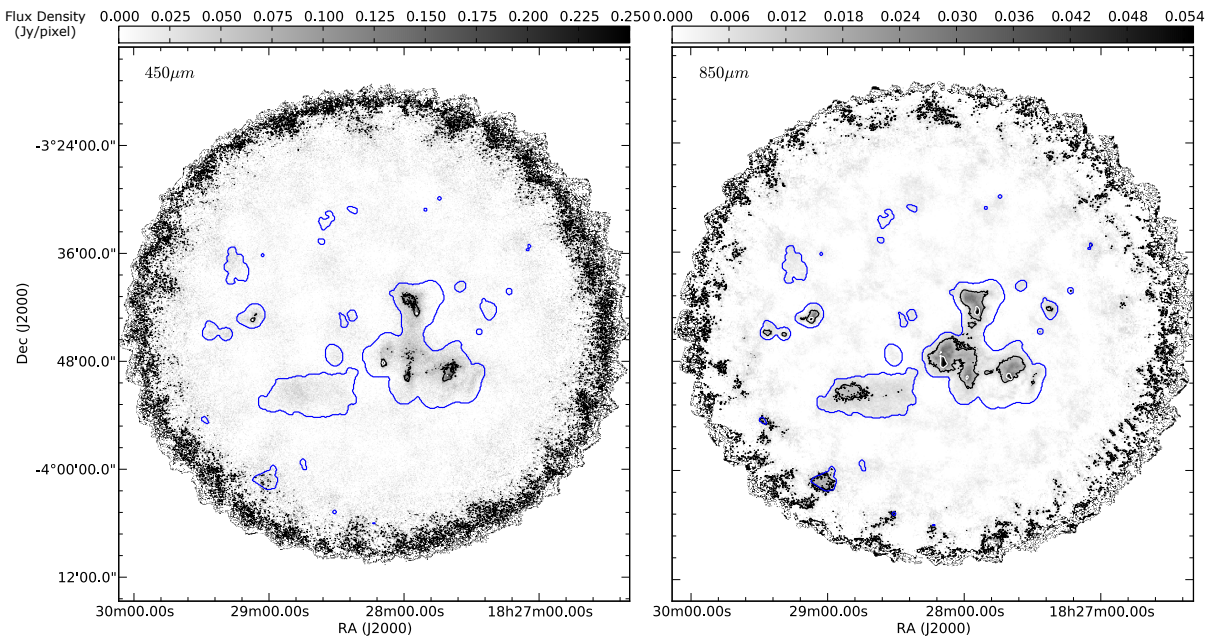


Figure 2.3: SCUBA-2  $450\mu\text{m}$  (left) and  $850\mu\text{m}$  (right) data. Contours show  $5\sigma$  and  $15\sigma$  levels in both cases: levels are at  $0.082, 0.25\text{ Jy/}4''\text{ pixel}$  and  $0.011, 0.033\text{ Jy/}6''\text{ pixel}$  at  $450\mu\text{m}$  and  $850\mu\text{m}$  respectively. The blue outer contour shows the data reduction mask for the region, based on *Herschel*  $500\mu\text{m}$  observations. Noise levels increase towards the edges of the map on account of the mapping method outlined in Section 2.1.

measured the foreground part of the rift and that Serpens Main is part of a separate star forming region positioned further back. On this basis, we adopt a distance of  $d = 250 \pm 50$  pc to the Aquila rift and the Serpens MWC 297 region (Sandell et al., 2011).

The star MWC 297 is an isolated, intermediate mass Zero Age Main Sequence (ZAMS) star located to the south east of Serpens South at RA(J2000) =  $18^h 27^m 40^s.6$ , Dec. (J2000) =  $-03^\circ 50' 11''$ . Drew et al. (1997) noted that MWC 297 has strong reddening due to foreground extinction ( $A_V = 8$ ) and particularly strong Balmer line emission. The star has been much studied as an example of a classic Herbig AeBe star, defined by Herbig (1960), Hillenbrand et al. (1992) and Mannings (1994) as an intermediate mass ( $1.5$  to  $10 M_\odot$ ) equivalent of classical T-Tauri star, typically a Class III pre-main sequence star of spectral type A or B.

Herbig AeBe stars are strongly associated with circumstellar gas and dust with a wide range of temperatures. Berrilli et al. (1992) and Di Francesco et al. (1994, 1998) find evidence of an extended disk/circumstellar envelope around the star MWC 297. Radio observations constrain disk size to  $< 100$  AU and also find evidence for free-free emission at the poles that suggest the presence of polar winds or jets (Skinner et al., 1993; Malbet et al., 2007; Manoj et al., 2007). MWC 297 is in a loose binary system with an A2 star, hereafter referred to as OSCA, which has been identified as a source of X-ray emission (Vink et al., 2005; Damiani et al., 2006). In addition to MWC 297, there is also a large nebulosity, Sh2-62 which occupies the same space on the sky (Sharpless, 1959). Drew et al. (1997) compare the radial velocities of the star and the HII region Fich et al. (1990) and find they are significantly different, suggesting that a physical association is unlikely and the objects are simply superimposed on each other.

We pull together existing YSOc catalogues, discuss the various methods used to compile them, compare the distribution of objects to the SCUBA-2 submillimetre data. From here on Class 0, I and Flat Spectrum (FS) YSOs are referred to as protostars and Class II, Transition Disk (TD) and III YSOs are referred to as Pre-Main Sequence (PMS) stars. Three YSOc catalogues are found for the Serpens MWC 297 region, each deploying a different method to identify and classify YSOcs. The earliest catalogue found is of *Chandra* ACIS-I X-Ray observations carried out by Damiani et al. (2006) over an area of  $16.9' \times 8.7'$  centred on the star MWC 297. YSOc identification is a byproduct of the investigation into the X-ray flaring of the star MWC 297 and as a consequence their sample is incomplete for the whole of the Serpens MWC 297 region ( $30'$  diameter). They find that the star MWC 297 only accounts for 5.5 per cent of X-ray emission in the region. The rest is attributed to flaring low mass PMS. As Damiani et al. (2006) do not make the distinction between YSOs and more evolved objects in their work it is not possible to use these data for the purposes of classification.

## IR catalogues

The MWC 297 region was observed twice by *Spitzer* in the mid-infrared, first as part of the *Spitzer* Young Clusters Survey (SYC; Gutermuth et al. 2009) and secondly as part of the *Spitzer* legacy program “Gould’s Belt: star formation in the solar neighbourhood” (SGBS, PID: 30574). In both surveys, mapping observations were taken at  $3.6$ ,  $4.5$ ,  $5.8$  and  $8.0 \mu\text{m}$  with the Infrared Array Camera (IRAC; Fazio et al. 2004) and at  $24 \mu\text{m}$  with the Multiband Imaging Photometer for *Spitzer*



Table 2.3: YSO candidates in the MWC 297 region.

	YSO Classification		
	0/I	II	III
Damiani et al. (2006)	-	-	27
SGBS <sup>a</sup> - Gutermuth et al. (2008)	8	32	36
SYC - Gutermuth et al. (2009)	4	16	2
Total <sup>b</sup>	10	72	

a) Within a 20' radius area centred at RA(J2000) =  $18^h 28^m 13^s.8$ , Dec. (J2000) =  $-03^\circ 44' 1.7''$ .

b) The totals account for sources which feature in multiple catalogues.

across catalogues. These are YSOc2, 47 and 11 presented in Table 2.2. Similarly SGBS identifies 22 PMS-stars whereas SYC identified 18. Across the sample 11 are consistent in both catalogues. Objects that appear in both catalogues are most likely to be real YSOs. Of the two *Spitzer* YSO surveys, we use SGBS as the primary *Spitzer* catalogue because it covers all of the SCUBA-2 mapped area. All IR surveys are subject to contamination by Galactic sources (for example, field red giants) and extra-Galactic sources (broad line AGN). Gutermuth et al. (2009) calculate that this should account for less than 2 per cent of sources in Serpens/Aquila. In addition to this, Connelley & Greene (2010) discuss how target inclination can play a role in classification. In Table 2.3 we give the total numbers of YSOcs in each catalogue by evolutionary class whilst in Figures 2.4 and 6.3 we plot the positions and evolutionary classification of the SGBS YSOcs on the  $850\ \mu\text{m}$  flux map. In Figure 2.4 we show whether or not the *Spitzer* YSOcs are consistent with the Damiani et al. (2006) X-ray sources. One further catalogue was found for the region. Connelley & Greene (2010) uses *IRTF* 2MASS NIR data to classify Class I sources, by spectral index. The study lacks depth, returning a single object for this region and this being MWC 297, an object which is omitted from SGBS due to saturation. This result should be questioned as MWC 297 has been observed to be a Class III or ZAMS B1.5Ve star (Drew et al., 1997) which are optically visible, where as Class I objects are typically obscured by their natal envelopes.

#### 2.4.2 Serpens South

Serpens South is considered part of the Aquila-Rift along with Serpens MWC 297 MWC 297. The Rift is heavily obscured by its molecular cloud (Vallee, 1987) with an extinction wall of  $A_v \geq 5$  at  $250 \pm 50\text{pc}$ . Serpens South is complicated by the presence of the nearby W40 complex (separation of approximately 1.5') and extended sections of each region may overlap.

Maury et al. (2011) estimates mass of the primary star forming core as  $610M_\odot$  and column density of  $3.1 \times 10^{22}\text{cm}^{-2}$  over the projected area of  $1\text{pc}^{-2}$ . From this star-formation efficiency (SFE) is estimated as approximately 7% and star-formation rate (SFR) is approximately  $23M_\odot\text{Myr}^{-1}\text{pc}^{-2}$  which is significantly higher than the typical values for inert molecular clouds (?).

The morphology of the region has been examined by Men'shchikov et al. (2010). Figure ?? demonstrates the extent of filamentary structure and how the observed protostars of the region are found within them. André et al. (2010) studies SFR and SFE associated with filaments. Figure

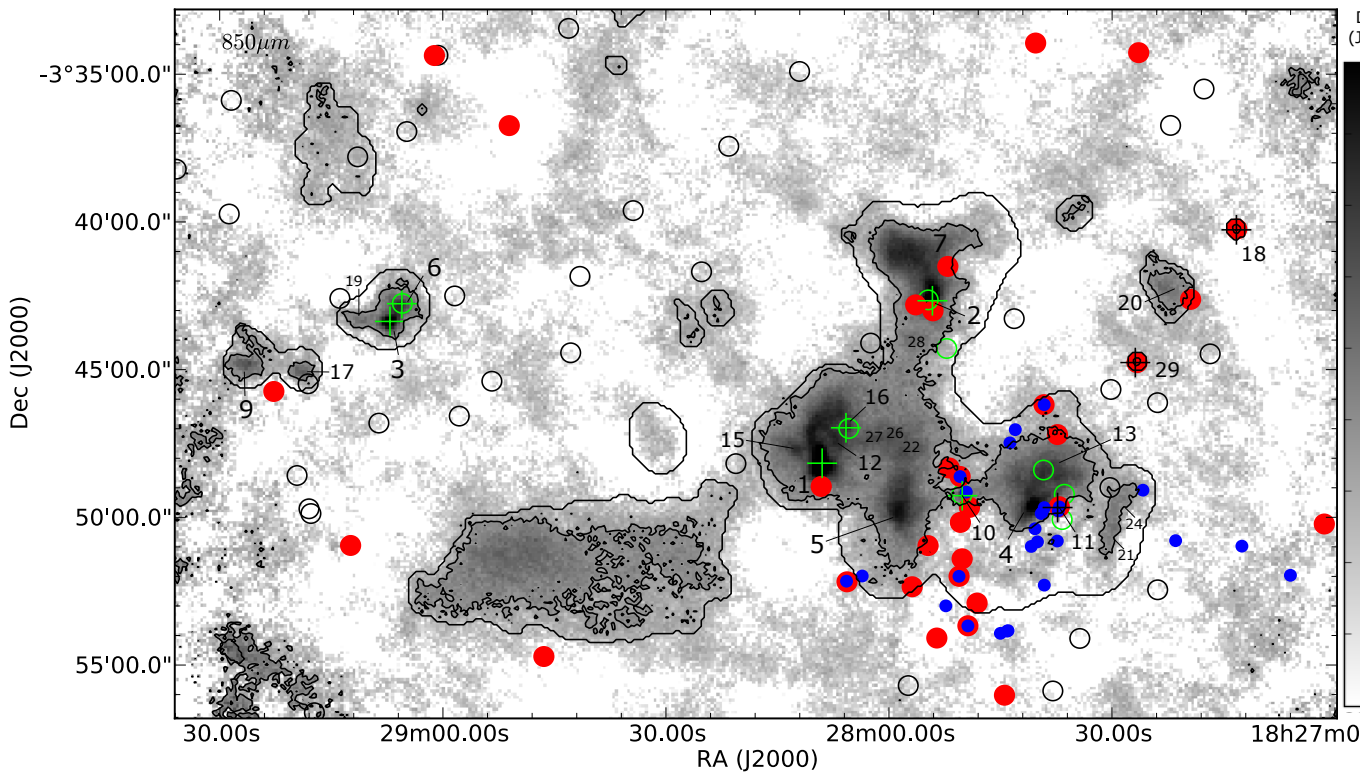


Figure 2.4: 850  $\mu\text{m}$  greyscale map of Serpens MWC 297. Outer contours mark the data reduction mask (Figure 1) and inner contours the  $3\sigma$  detection level (0.0079 Jy/pixel). Circular markers indicate the location of YSOcs as catalogued by SGBS and crosses indicate the location of SCUBA-2 confirmed YSOs (Table 6.3). YSOcs are coded by evolutionary classification based on their spectral indices ( $\alpha_{\text{IR}}$ ) in the *Spitzer* case and by bolometric temperature,  $T_{\text{bol}}$ , in the SCUBA-2 case (Table 6.3). *Spitzer* YSOcs are indicated by hollow black circles (Class III), solid red circles (Class II) and green hollow circles (Class 0/I). SCUBA-2 confirmed YSOs are indicated by black crosses (Class II) and green crosses (Class 0/I). Small, solid blue circles mark the location of Damiani et al. (2006) X-ray sources, typically associated with Class II/III objects.

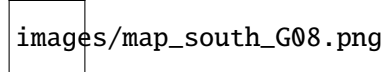


Figure 2.5: left: composite image of Serpens South from IRAC wavelength; 3.6, 4.5, 8.0  $\mu\text{m}$  in blue, green and red, respectively. Right: Greyscale 8.0  $\mu\text{m}$  image overlaid with YSOs; Class I and II in red circles and green diamonds, respectively. The white circle outlines the extent of the core (?).

?? also demonstrates the extent and complexity of the structure with many extraneous sub-cores with detect protostars in their vicinity.

The region was included in the *Spitzer* c2d survey (Evans et al., 2003) which formed the basis for the first meaningful studies of Serpens South. Since then the *Spitzer* GBS catalogs have developed and provide a wide insight into Protostars in Serpens South.

The foremost study of South was by ? which identified 101 YSOs: 54 Class I and 37 Class II from 3.6, 4.5, 5.8 and 8.0  $\mu\text{m}$  IRAC data centred on  $\alpha:18^{\circ}30'03'', \delta:-02^{\circ}01'58.2''$  as shown in Figure 2.5. The cluster was found to have a well defined ‘core’ region where the surface density of protostars was  $590 \text{ pc}^{-2}$  and accounted for 77% of the YSOs detected. Extended filamentary structure was also observed with surface density ranging between  $50\text{-}120 \text{ pc}^{-2}$  and for a total length of approximately 1pc and column density  $N=3\times 10^{23} \text{ cm}^{-2}$ . Connelley et al. (2007)’s survey of 0.8 to 2.43  $\mu\text{m}$  includes South and the results contribute to constraining of the parameters of YSOs in the cluster.

Könyves et al. (2010) and Bontemps et al. (2010) to catalogue the protostars in the whole of Aquila Rift using recent data from *Hershel* and they conclude there are 541 starless cores, of which 452 are gravitationally bound and therefore likely to evolve into protostars. Through measurements of velocities and analysis of the age, density and distribution of protostars in what is perceived to be Serpens South, they to conclude that South is sufficiently similar Serpens Main and Serpens Ammonia in distance and velocity structure, that, given there close proximity, they are in fact part of the same cloud structure. By contrast W40 is not only different but the OB association within does no appear to influence the structure of South as would expected if they were sufficiently close. The *Hershel* YSO catalog will shortly be released and will provide the first comparable survey to *Spitzer* GBS which will allow better constraints on the reliability of the competing methods of detecting Protostars.

Bontemps et al. (2010); André et al. (2010); Men’shchikov et al. (2010) utilise *Hershel* Far Infrared and submillimetre data from SPIRE (250 to 500  $\mu\text{m}$ ) and PACS (100 to 160  $\mu\text{m}$ ) to study the advanced morphology of the regions. Controversially, Bontemps et al. (2010) argues that large uncertainties in previous measurements of distance do not allow for a reliable estimate and therefore they favour the status quo, that South is physically connected to W40 and therefore at the same distance. They detect 201 YSOs in Serpens-Aquila - though it is notable that 90% of these are attributed to W40 and a further 8% MWC 297 (see section 1.2). It is important to note, that whilst Bontemps et al. (2010) does not provide complete classification of list of YSOs, they do claim to have identified 45-60 Class 0 objects with the *Hershel* data, 7 of which are within South. Until this point, Class 0 had been elusive and this paper represents the first statistically



Figure 2.6: (*left*) Serpens Main in three-band false-colour IRAC *Spitzer* bands  $3.4\,\mu\text{m}$  (blue),  $4.5\,\mu\text{m}$  and  $8.0\,\mu\text{m}$ . Redish hue shows diffuse PAH emission, green is typically shocked Hydrogen and more blue sections is scattered light (Winston et al., 2007). (*Right*)  $850\,\mu\text{m}$  greyscale and  $450\,\mu\text{m}$  contour images of Serpens Main. Submillimeter continuum sources identified by Casali et al. (1993) are labeled as SMM1, etc. Cavity features due to outflows that are investigated by Davis et al. (1999) are also labeled though the central white patch here represents a depression in flux and is in fact an artefact of the reduction process. Contours in  $450\,\mu\text{m}$  are set at 0.5, 1, 2, 3 and 4 (black) and 5, 10 and  $20\,\text{Jy}\,\text{beam}^{-1}$ . The relative beam size of each map is displayed in bottom left of each image (  $14''$  at  $850\,\mu\text{m}$  and  $8''$  at  $450\,\mu\text{m}$  )

significant survey of Class 0 protostars.

#### 2.4.3 Serpens Main

The Serpens Main Molecular Cloud (identified in Figures 2.2, *left* 2.6 and ?) is located [RA DEC] and was first identified as a region of active star formation by Strom et al. (1974). It has been extensively mapped for molecular line emission Dame & Thaddeus, 1985; Dame et al., 1987, 2001, dust extinction Cambrésy, 1999; Dobashi et al., 2005 and at a variety of wavelengths.

$850\,\mu\text{m}$  maps (figure ??) of Serpens Main show peaks in flux and column density in two separate clumps, a northwestern (NW) and southeastern (SE) clump. Both structures are of similar size, distance and are at close proximity, being separated by 200arcsec or a few parsecs (Casali et al., 1993). Figure 2.6 *right* shows  $850\,\mu\text{m}$  and  $450\,\mu\text{m}$  SCUBA maps of Serpens detailing suspected submillimeter sources SMM1 through to SMM11. Davis et al. (1999) investigates the flux and properties of these sources in an attempt to categorise these YSO by calculating their Spectral Energy Distributions (SED). McMullin et al. (2000) attempted to calculate mass of Main using the  $C^{18}O$  ( $J = 1-0$ ) line transition and found it to be  $250\text{--}300M_{\odot}$ . By contrast, White et al. (1995) found it to be  $1450M_{\odot}$  using the same method. However there is consensus with Williams (2000)'s work which show both clumps are undergoing in-falling motion due to gravity supporting the conclusion that star formation through mass accretion is ongoing.

Many studies have been conducted into the exact distance of Serpens Main. Initial studies by Zhang et al. (1988) put the distance at between 700 pc and 200 pc but more recent studies by Racine (1968) [errr check this citation] and Straižys et al. (2003) have returned smaller and more precise values using a variety of different techniques. These methods are outlined in more detail in those papers and their respective results appear to converge on  $225\pm55$  pc. [UPDATE distance now 415pc]

Eiroa & Casali (1992) conducted an early, near-infrared observations of the Serpens Main in the J,H,K and nbL bands detecting 163 stellar objects but were unable to reliable identify many of the objects. X-ray studies have been carried out by Preibisch (2003) and Winston et al. (2007). Preibisch's initial study using *XMM-Newton* data revealed 1 Class I and 2 Class Flat Spectrum (FS) protostars. Winston then expanded on this considerably with use of joint *Spitzer* and *Chandra* observation through 6 wave bands from 3 to  $70\,\mu\text{m}$ . They identified 183 YSOs in Serpens Main:

22 Class 0/I, 16 Class FS, 62 Class II, 17 Class Transition Disc (TD) and 21 Class III. 60 were found to exhibit X-ray emission with no correlation for evolution class.

Work by Evans et al. (2003) resulted in the *Spitzer c2d Legacy Programme*, a wide ranging survey of star forming clusters with its IRAC, IRS and MIPS instruments to observe mid to far-infrared sources between 3.6 and 70  $\mu\text{m}$ . Serpens Main was included in this study and data has been analysed by many subsequent authors. ?? subsequently identified 235 YSO in Serpens (this includes Serpens  $NH_3$ ).

Kaas et al. (2004) presented an ISOCAM survey at the *Infrared Space Observatory (ISO)* which detected 392 sources in the 6.7  $\mu\text{m}$  band and 139 in the 14.3  $\mu\text{m}$  band. 124 of these were common in both bands and 61 were constrained as YSO candidates.

Eiroa et al. (2005) looked at 3.5cm radio emission from Serpens Main using the Very Large Array (VLA). 16 of the 22 sources detected were classified as YSOs, with the radio emission most likely resulting from thermal jets.

Such is the prominence of Serpens Main that it features heavily in several other large surveys of YSOs across many star forming regions, namely Enoch et al. (2009); ?; Sadavoy et al. (2010). Each survey uses a slightly different criteria for detection and selection of sources, allowing for analysis of methodology behind observing as well as their distribution with respect to 850  $\mu\text{m}$  SCUBA-2 data.

A total of 140 YSO candidates cited in Winston et al. (2007); ?; ? are compared in Serpens Main. [mention detection methods]. 92 sources are consistent between catalogs and have been identified by different methods making it likely they are indeed YSO as opposed to contaminants such as background galaxies or foreground stars. Only 48 data points are not consistent within any other catalog and should be receive a larger degree of scepticism. Classification between Protostars and PMS stars is inconsistent in 14 cases, 4 of which occur substantially outside of the cluster.

#### 2.4.4 Serpens $NH_3$ and VV Ser

Serpens  $NH_3$  was first observed by Cohen & Kuhi (1979) who identified 4 optical T-Tauri stars (Serpens G3, 4, 5, 6). The surrounding region was then mapped by Clark (1991) who also identified two additional sources with strong ammonia 1,1 emission lines (for which the cluster is named). Additional Herbig-Haro objects (small, nebulous regions formed from outflow material from Class 0 and I protostars Ziener & Eislöffel (1999)) and  $H_2O$  masers (Persi et al., 1994) were found providing further evidence of on going star formation.

The morphology of  $NH_3$  is similar to Serpens Main as it has two separate clumps of dense star formation with connected filaments as indicated in SCUBA-2 submillimeter data (Figure ?? and also IRAM mm data Figure??). Figure ?? shows the whole structure in relation to Main, the large scale density structure has a NE-SW orientation. Djupvik et al. (2006) uses 1.3mm observations from IRAM to quantitatively show that emission is, in general, less intense in  $NH_3$  than in Main.

Authors have adopted a distance to Serpens  $NH_3$  as  $225 \pm 55$  pc in line with the distance to the Serpens Cauda Clouds calculated by Straižys et al. (2003). ? represents the first known YSO

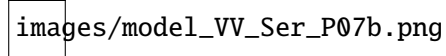


Figure 2.7: The 4.5 (blue), 8.0 (green), 24.0  $\mu\text{m}$  (red) colour composites of the VV Ser nebulosity by Pontoppidan et al. (2007). *left*: *Spitzer* MIPS band 1 and IRAC band 2 and 4 colour image of VV Ser. *right*: The model of the star-disk-nebulosity system produced by the above author with the same colour composite scheme

survey of the region. This study included Main as well due to the proximity of the two clusters. Harvey describes this ‘cluster B’ as less dense than ‘cluster A’ (Main) but still the second most region in the local area which high concentrations of Class I sources and evidence of outflows (Figure ??).

Djupvik et al. (2006) presents a comprehensive review of the region and its YSOs, presenting evidence for 31 Class II sources, 5 Class FS sources, 5 Class I sources and 2 Class 0 sources. Note that Class III were omitted from the sample purposely due to selection bias. ? revisited Serpens  $NH_3$  and was able to produce significant improvements in the photometry of the sources of the regions, producing extended SEDs for many of them as well to better constrain the classification of the YSO and the revised YSO list is as follows: 8 Class II sources, 1 Class FS sources, 4 Class I sources and 2 Class 0 sources.

Work by Evans et al. (2003) on the *Spitzer c2d Legacy Programme* remains the largest available catalog of YSOs for  $NH_3$  but instances of sources from the wider Connelley et al. (2007) near-infrared survey of YSOs and the *Spitzer* GBS survey (?) are also available.

Djupvik calculates Luminosity (LF) and Initial Mass Functions (IMF) by combining the Class II source for  $NH_3$  with the same set for Main (Kaas et al., 2004) to produce a statistically significant sample from which it is possible to confirm the coeval age of the sources as 2Myrs by trialling several scenarios and selecting the best fit.

VV Serpens is a young UX Variable Orion Star located at  $\alpha: 18^{\circ} 28' 47.865'' \delta: +00^{\circ} 08' 39.76''$  roughly 20' to the south of Serpens  $NH_3$ , see Figure ???. Chavarria-K. et al. (1988) found a large nebulosity associated with the object. There is some debate over the exact spectral type of the star with publications claiming the later, B6 type (Hernández et al., 2004) to the less powerful A2 (Chavarria-K. et al., 1988). More recent authors agree with the classification of A0 printed by (?). VV Ser has very low extinction ( $A_v \sim 3$ ) allowing for accurate and precise measurements of its properties (Pontoppidan et al., 2007). Pontoppidan et al. (2007) measures an effective temperature of 10200K, a mass of  $2.6 \pm 0.2 M_{\odot}$  and an age of  $3.5 \pm 0.5$  Myr. There is a wealth of  $\mu\text{m}$  wavelength data on this object curtosy of the *Spitzer Legacy Program* and *From Molecular Cores to Protoplanetary Disks* Evans et al. (2003). VV Ser has been used for the study of dust and proto-planetary disks by Pontoppidan et al. (2007,?) and Alonso-Albi et al. (2008).

VV Ser is an example of UX Variable Orion star, whereby the star is inclined such that its disk is appears edge on to the observer. As a result it casts a narrow band shadow across the star as observed in figure fig.VV Ser. Additionally, the light may frequently change in extinction due to ‘clumps’ of material in the disk eclipsing the star due to keplerian motion Natta et al. (2001). Another feature of VV Ser is a vast, extended, low density nebulosity spanning 94,000 Au which has no detectable optical or IR counter parts. This combined with low extinction suggests that the

star has lost the vast bulk of its primordial envelope.

Together with Main and VV Serpens, these three objects are collectively known as ‘Serpens’ and are shown together in the SCUBA-2 data (Figure ??).

#### 2.4.5 W40 Complex

#### 2.4.6 Serpens East

E is notable region of the Aquila rift with strong submillimeter features. it is covered very sparsely in the literature with no known catalogs or studies of the YSOs in the region. Szymczak et al. (2000) surveys IRAS 6.7GHz Methanol maser emission and similarly Wu et al. (2006) studied a selection of sources with strong ammonia lines, including *IRAS 18352-0148* which is found in E. This source is also a strong  $H_2O$  maser which are often found at sites of high mass star formation (Wang et al., 2007). This could potentially be a first indicator of star formation in E, however the literature puts the distance to this maser at 3.2kps. This is over an order of magnitude further away than all the other components of Serpens-Aquila.

#### 2.4.7 Other

# 3

## CO observations of star-forming regions

### 3.1 Introduction to CO contamination and outflows

### 3.2 HARP

### 3.3 CO reduction

### 3.4 CO observations

#### 3.4.1 PPV Clouds

#### 3.4.2 Outflows

### 3.5 CO contamination of SCUBA-2 850 $\mu\text{m}$

#### 3.5.1 Literature

CO is known to be found in conjunction with dust and molecular hydrogen gas in GMCs, either in the form of ambient ground or excited states. Observing bright CO is used to trace either high column densities of molecular gas (assuming the emission is optically thin) or heating through exposure to radiative feedback. Careful analysis of line emission profile can be used to identify outflows which are the signatures of embedded protostars (Graves et al., 2010). Outflows primarily provide dynamical feedback into a molecular cloud, though the most powerful outflows may also contribute a small, localised radiative component.

We use our HARP 345.796 GHz observations of the  $^{12}\text{CO}$  3–2 line emission to assess the impact of CO emission on the 850  $\mu\text{m}$  band, which is a known contaminant of the 850  $\mu\text{m}$  band

(Gordon, 1995) observed by SCUBA-2.

Davis et al. (2000) and Tothill et al. (2002) have all observed CO contamination of SCUBA data of up to 10% whilst Hatchell & Dunham (2009) have found contamination up to 20%. Johnstone et al. (2003) and Drabek et al. (2012) record a minority of cases where CO emission dominates the dust emission (up to 79%) in SCUBA-2 observations, with these regions hosting substantial molecular outflows in addition to ambient molecular gas within the clouds.

Given that CO contamination affects the 850  $\mu\text{m}$  band but not the 450  $\mu\text{m}$  band, an assessment of  $^{12}\text{CO}$  3–2 line emission is vital for an accurate assessment of dust temperature with unaccounted CO emission producing artificially lower ratios and cooler temperatures (Equation 5.1, see Section 5). We use Drabek et al. (2012)'s method by which CO line integrated intensities can be converted into 850  $\mu\text{m}$  flux densities and directly subtracted from SCUBA-2 data.

### 3.5.2 Methodology

Reliable temperatures depend on accurate input fluxes. Systematic contamination of 450  $\mu\text{m}$  and 850  $\mu\text{m}$  flux by molecular lines, in particular CO, is a known problem within SCUBA-2 data (Drabek et al., 2012). We investigate the contribution of CO and free-free emission to these bands and attempt to mitigate their effects where necessary.

## 3.6 Contamination in the Serpens MWC 297

Hatchell et al. (2013) and Drabek et al. (2012) highlighted 345 GHz contamination of 850  $\mu\text{m}$  due to the CO 3–2 line in other Gould Belt star-forming regions. Limited  $^{12}\text{CO}$  and  $^{13}\text{CO}$  1–0 data exist for the Serpens MWC 297 region (Canto et al., 1984). A very rough estimate of the CO contamination towards the star MWC 297 can be made based on the published spectra. The  $^{12}\text{CO}$  lines are broad ( $\sim 12 \text{ km s}^{-1}$ ) but do not show line wings characteristic of outflows. Making the simplest assumption that the  $^{12}\text{CO}$  is optically thick and fills the beam in both the  $J = 1\text{--}0$  and  $J = 3\text{--}2$  lines, the integrated intensity of the latter will be similar to the former,  $\sim 36 \text{ K km s}^{-1}$ , corresponding to a CO contamination of  $1.14 \text{ mJy/pixel/K km}^{-1}$  (13 per cent of peak flux) at the position of the star MWC 297 using the conversion in Drabek et al. (2012) updated for the beam parameters in Dempsey et al. (2013). Drabek et al. (2012) noted than regions where CO emission accounts for less than 20 per cent of total peak emission are not consistent with outflows or major contamination. Manoj et al. (2007) find no evidence of CO 2–1 and  $^{13}\text{CO}$  2–1 emission within 80 AU of MWC 297 and conclude this depletion is caused by photoionisation due to an ultra-compact H II (UCHII) region as has been detected by Drew et al. (1997) and Malbet et al. (2007).

Fuente et al. (2002) - high res  $^{13}\text{CO} + 18\text{CO}$ . Evidence of a cavity. Ridge et al. (2003) - Low res  $18\text{CO}$ .

## 3.7 Contamination in the the W40 complex

### Observations

Archival HARP  $^{12}\text{CO}$  3–2 data (van der Wiel et al., 2014) confirms the presence of red- and blue-shifted gas in the Dust Arc (Figure 2.3) but coverage is limited to a  $2' \times 2'$  region centred on the peak of the submillimetre emission, and therefore we commissioned an extended survey of the W40 complex in  $^{12}\text{CO}$  3–2 that included the whole of the Dust Arc and W40-N, as presented in Figures 2.3 and 3.1. Subsequent to our observations, Shimoikura et al. (2015) mapped the W40 complex the Atacama Submillimeter Telescope Experiment (ASTE) observations in  $^{12}\text{CO}$  3–2 and  $\text{HCO}^+$  4–3 with a similar coverage, but at the lower effective resolution of  $22''$  compared to the JCMT (14.6'').

Aquila was observed with HARP (Heterodyne Array Receiver Programme, Buckle et al. 2009) on the 4th of July 2015 as part of the M15AI31 "active star-formation in the W40 complex" proposal. The main beam efficiency,  $\eta_{\text{MB}}$ , taken from the JCMT efficiency archive is 0.61 at 345 GHz. Two sets of four basket-weaving scan maps were observed over an approximately  $7' \times 18'$  area (position angle = 65) at 345.796 GHz to observe the  $^{12}\text{CO}$  3–2 line. A sensitivity of 0.3 K was achieved on  $1 \text{ km s}^{-1}$  velocity channels in weather Grade 4 ( $\tau_{225} = 0.16$ ). Maps were referenced against an off-source position at RA(J2000) = 18:33:29.0, Dec.(J2000) = -02:03:45.4, which had been selected as being free of any significant CO emission in the Dame et al. (2001) CO Galactic Plane Survey.

The data were first reduced using the SMURF `makecube` technique (Jenness et al., 2015). An integrated intensity map, corrected for main beam efficiency, was produced by collapsing along the entire velocity range and subsequently run through the SCUBA-2 data reduction pipeline with the effect of filtering out scales larger than  $5'$  as well as regridding to  $3''$  pixels. Figure 3.1 presents the reduced  $^{12}\text{CO}$  3–2 integrated intensity map for the W40 complex.

### Contamination results

Integrated intensity maps of  $^{12}\text{CO}$  3–2 emission are subtracted from the original SCUBA-2  $850 \mu\text{m}$  maps using a joint data reduction process before a  $4'$  filter is applied following the method outlined in Appendix B. The fraction of SCUBA-2 emission that can be accounted for by  $^{12}\text{CO}$  3–2 line emission is presented in Figure 3.2. Contamination in W40-N is minimal with levels up to 5%. The Dust Arc has significantly more contamination at the level of 10%, reaching up to 20% at its highest.

Figure 3.3 shows the distribution of flux ratios (Equation 5.1 and the method given in Appendix A) with and without CO contamination contributing to  $850 \mu\text{m}$ , showing how even a small degree of CO contamination can have a significant effect on measuring the temperature of the cloud, increasing the modal flux ratio from 6.8 to 7.8 when CO is subtracted. Furthermore, the FWHM of the distribution increases from 1.9 to 2.8. Subtracting CO from our maps increases the mean and standard deviation of temperature in regions where  $^{12}\text{CO}$  3–2 is detected, in comparison with temperatures derived from uncorrected maps. The distribution of flux ratios across the map, with and without the CO contamination, are compared and found to have a KS-statistic of 0.253,

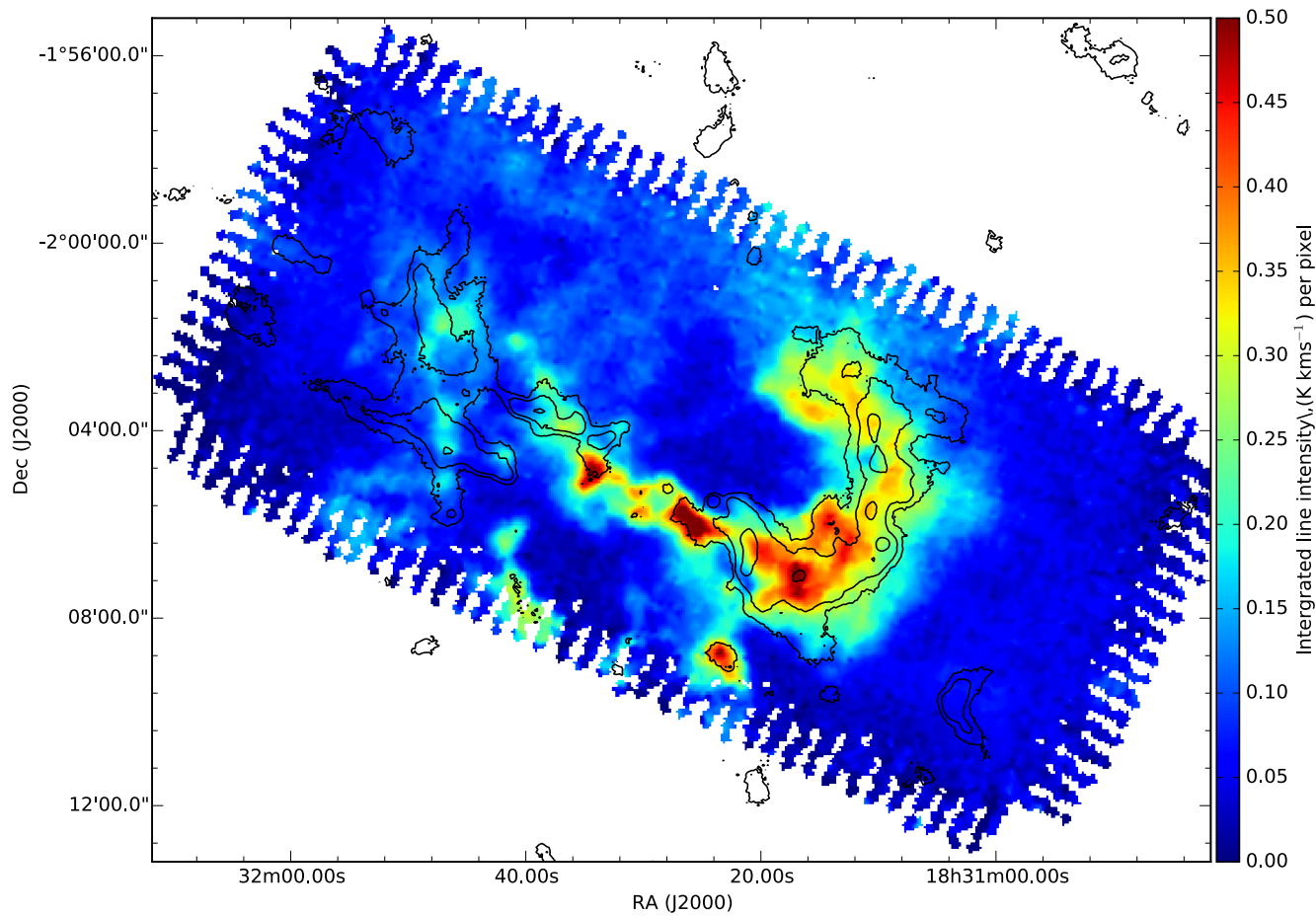


Figure 3.1:  $^{12}\text{CO}$  3–2 integrated intensity map over the entire range (colour scale over  $-90$  to  $+100 \text{ km s}^{-1}$ ) of the central region of the W40 complex. Contours show SCUBA-2  $850 \mu\text{m}$  emission at the  $5\sigma$ ,  $15\sigma$  and  $50\sigma$  levels.

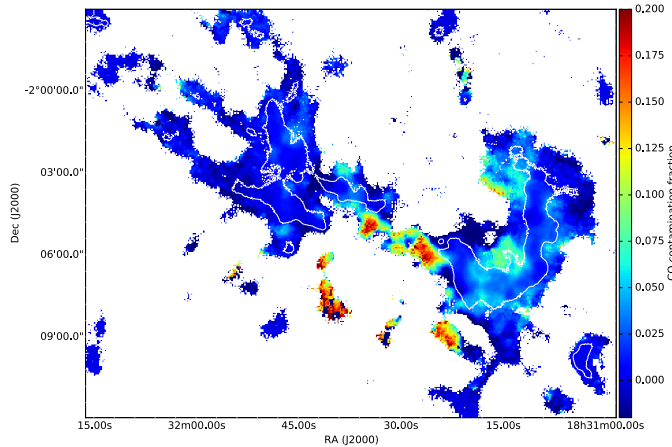


Figure 3.2: The fraction of SCUBA-2 850  $\mu\text{m}$  that can be attributed to  $^{12}\text{CO}$  3–2 345 GHz line emission. The SCUBA-2 data are masked at  $3\sigma$  and the  $5\sigma$  level is shown in white.

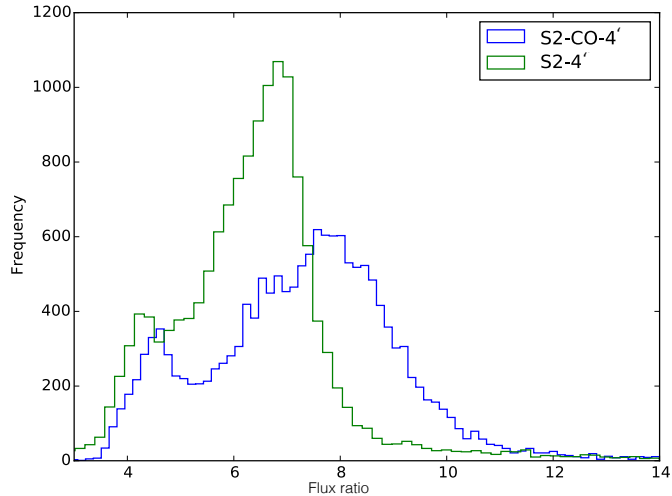


Figure 3.3: The distribution of 450  $\mu\text{m}$ /850  $\mu\text{m}$  flux ratio for the original (blue - S2-4') and CO subtracted (green - S2-CO-4') Aquila reductions with additional 4' spatial filtering. KS-statistics reveal a 1.3% chance that the two data sets are drawn from the same distribution.

corresponding to 1.3% probability that the two samples are drawn from the same parent sample. CO contamination in the W40 complex is having a significant impact on distribution of flux ratios.

### 3.7.1 Cloud velocities

Two distinct components are visible in the velocity space of the  $^{13}\text{CO}$  2–1 cube and are presented in Figure D1. A blueshifted component is observed at approximately  $5\text{km s}^{-1}$  (consistent with Zeilik Lada 1978 and Shimoikura et al. 2015) with peak integrated flux of  $88\text{K km s}^{-1}$  that is coincident with the SCUBA-2 emission in the Dust Arc and, to a lesser extent, W40-N. A redshifted component is observed at approximately  $10\text{ km s}^{-1}$  with an integrated flux of  $86\text{ K km s}^{-1}$  and tightly traces a low luminosity filament of SCUBA-2 emission between W40-N and the Dust Arc, passing through the location of the OB association in the W40 complex.

Atacama Submillimeter Telescope Experiment (ASTE) observations by Shimoikura et al.

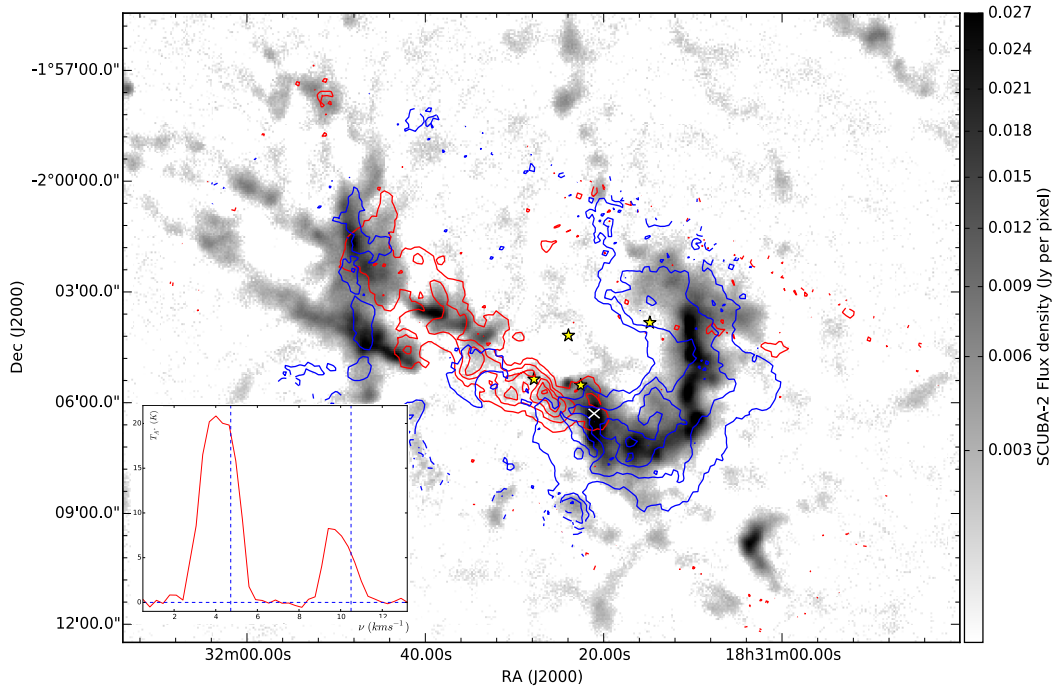


Figure 3.4: SCUBA-2 850  $\mu\text{m}$  map of the W40 complex with  $^{13}\text{CO}$  2–1 integrated intensity contours of red ( $10\text{ km s}^{-1}$ ) and blueshifted ( $5\text{ km s}^{-1}$ ) emission that trace out the location of two separate clouds within the region. Blue contours are at  $20, 40, 60, 80 \text{ K km s}^{-1}$  and red are the same levels with an additional contour at  $5\text{ km s}^{-1}$ . The greyscale SCUBA-2 850  $\mu\text{m}$  shown here has not had CO emission subtracted. Yellow stars mark the location of the OB stars in the W40 complex. The insert shows the line emission spectra at the position of peak SCUBA-2 luminosity, marked with a white cross. Two CO clouds are visible at  $5$  and  $10\text{ km s}^{-1}$  with a significant vacancy at  $7\text{ km s}^{-1}$  where Shimoikura et al. 2015 finds HCO 4–3 emission, indicating that our  $^{13}\text{CO}$  2–1 absence is due to optical depth and self-absorption.

(2015) provides evidence of a third velocity of approximately  $7 \text{ km s}^{-1}$  observed in HCO 4–3 at the submillimetre peak of the cloud (their Figure 2). HCO 4–3 remains optically thin at high column densities where  $^{13}\text{CO}$  2–1 may become optically thick. Shimoikura et al. (2015) argue that the sharp partition between 5 and  $10 \text{ km s}^{-1}$ , as seen in the insert of Figure D1, may be due a dense cloud at  $7 \text{ km s}^{-1}$  in which  $^{13}\text{CO}$  2–1 is extincted but HCO 4–3 is observed.

Our observations of 5 and  $10 \text{ km s}^{-1}$   $^{13}\text{CO}$  2–1 components are consistent with Shimoikura et al. (2015)’s interpretation of a molecular shell, swept up and heated by the expanding H II region, with divergent velocities either side of the shell. We find less evidence to support their claim that the ambient gas in the W40 complex has a velocity of  $7 \text{ km s}^{-1}$  as we detect no  $^{13}\text{CO}$  2–1 at that velocity in the relatively low density filaments that are significantly outside of the H II shell. It is unlikely that this component extends to our off position (RA (J2000) = 18:33:29.0, Dec. (J2000) = -02:03:45.4) as it was thoroughly examined in Zeilik & Lada (1978)’s  $^{12}\text{CO}$  1–0 observations and found to be clear.

HARP data are found to contain two clouds at  $5 \text{ km s}^{-1}$  and  $10 \text{ km s}^{-1}$  that trace different morphological structures (Figure D1). The redshifted filament starts in W40-N and traces a line from this cloud to the tip of the Dust Arc. The emission from  $^{13}\text{CO}$  2–1 is observed in SCUBA-2 850  $\mu\text{m}$  data and closely fits the HARP data, albeit at high SNRs, as shown in Figures D1 and 19. The red filament passes directly through the stellar cluster, enveloping the location of OS1a and the H II region, as shown in Figure 19.

Since CO is photo-dissociated in H II regions, the red filament is either shielding CO gas from the UV photons, or it is located in the foreground or background of the H II region. SCUBA-2 does not detect a significant dust filament coincident with redshifted the CO and therefore we discount the former premise. Furthermore, figure 19 shows how clumps W40-SMM 12, 13, 20, 21, 23 and 39 are coincident both with the bright rimmed clouds (BRCs) observed in Herschel 70  $\mu\text{m}$  data and peaks of redshifted CO emission, confirming that the CO gas is within the nebulosity. This picture is consistent with the findings of Shimoikura et al. (2015) who suggested the redshifted filament is a shell of heated CO gas swept up in the expanding shockwave around the H II region.

### 3.7.2 Outflow analysis

A first wave of  $^{12}\text{CO}$  1–0 observations of the W40 complex was made by Zeilik & Lada (1978) who found an ambient cloud with extended emission symptomatic of outflows with a local standard of rest velocity across the region of approximately  $4.5 \text{ km s}^{-1}$ . Evidence of a weak molecular outflow was found by Zhu et al. (2006).

The complex nature of red and blue-shifted emission in the W40 complex makes direct analysis of individual outflows very difficult. We instead refer to the method of identifying local peaks in  $^{13}\text{CO}$  2–1 integrated over the velocity ranges red and blue-ward of the  $5 \text{ km s}^{-1}$  and  $10 \text{ km s}^{-1}$  components, respectively, as used by Shimoikura et al. (2015). Peaks can be used to identify molecular outflows from protostars where the line profile shows a line-wing similar to those observed by Graves et al. (2010) in Serpens Main. This method is also sensitive to the bulk motion of shocked gas around the shell of the H II region, local variations in ambient gas velocity and foreground clouds at different velocity. Multiple outflow features in the outer’ velocity ranges

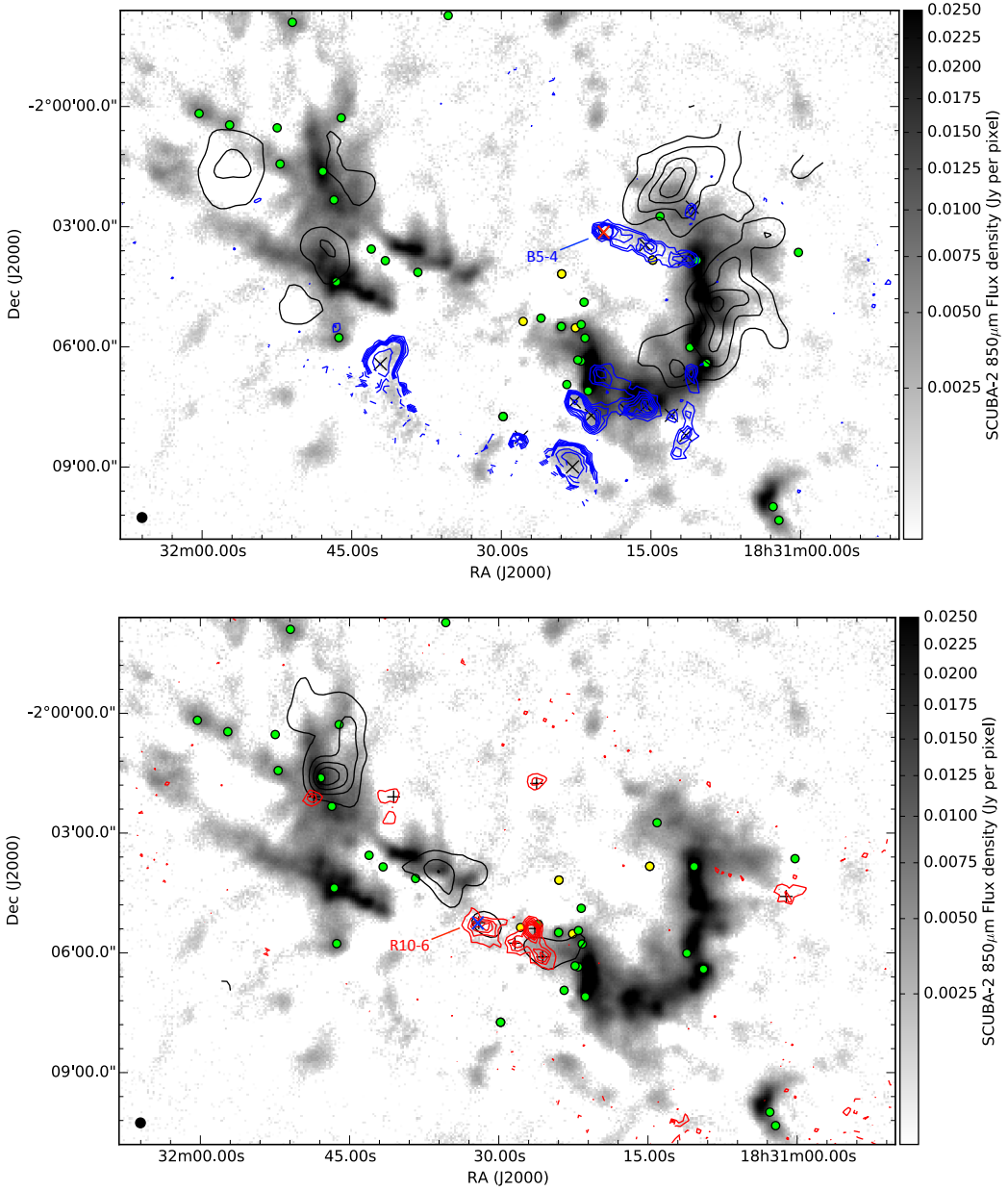


Figure 3.5: 2CO 32 integrated line emission in the blue wing of the  $5 \text{ km s}^{-1}$  (upper), and red wing of the  $10 \text{ km s}^{-1}$  cloud (lower). The blue  $5 \text{ km s}^{-1}$  wing is integrated over the velocity range  $3.2 \leq v_{LSR} \leq 2.8 \text{ km s}^{-1}$ . The red  $10 \text{ km s}^{-1}$  wing is integrated over the velocity range  $11.7 \leq v_{LSR} \leq 14.5 \text{ km s}^{-1}$ . Line wing sources are identified from local peaks in emission, identified as black crosses in the respective plots. Yellow stars and green circles indicate the location of the OB stars and protostars (from our composite YSoc catalogue). The grayscale backdrop map is SCUBA-2 850  $\mu\text{m}$  flux density. The black, smoothed contour represents emission from the alternative line wing (see text for velocity ranges).

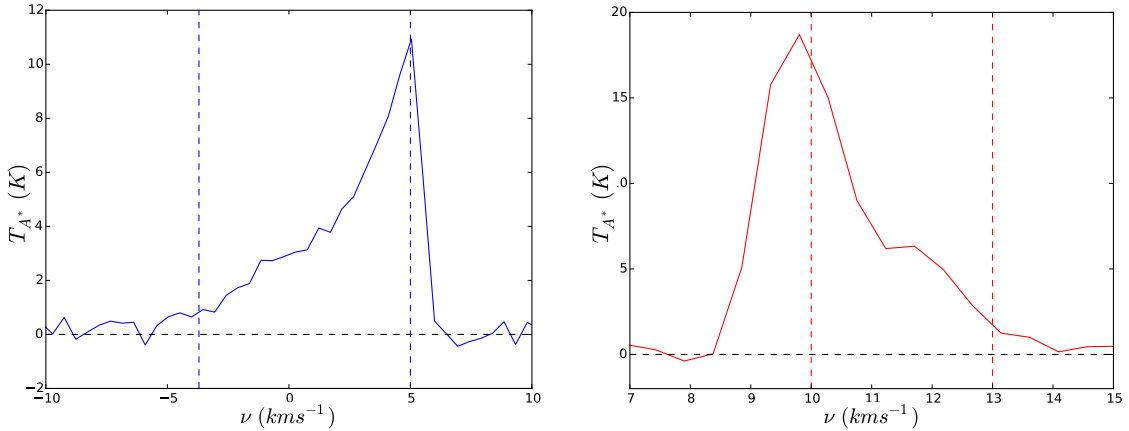


Figure 3.6:  $^{13}\text{CO}$  2–1 line profiles of example outflows R10-6 (left) and B5-4 (right) with their locations in the 10 and 5  $\text{km s}^{-1}$  clouds respectively marked in Figure E1. Each profile shows prominent outflow line-wings that are either red or blue shifted. Dotted lines demonstrate the length of the line-wing, from local cloud velocity to its maximum extent.

( $-3.2 \leq v_{\text{LSR}} \leq 2.8 \text{ km s}^{-1}$  and  $11.7 \leq v_{\text{LSR}} \leq 14.5 \text{ km s}^{-1}$ ) are detected (Figure E1). The ‘inner’ regions ( $5.7 \leq v_{\text{LSR}} \leq 8.4 \text{ km s}^{-1}$  and  $8.5 \leq v_{\text{LSR}} \leq 9.2 \text{ km s}^{-1}$ ) are where paired outflows would be expected, however Shimoikura et al. (2015) outlines how  $^{13}\text{CO}$  2–1 emission becomes optically thick due to a dense cloud at  $7 \text{ km s}^{-1}$ , and subsequently heavily extincts any outflows in this region of the spectrum.

We detect 15 blue objects in the  $5 \text{ km s}^{-1}$  component and nine red objects in the  $10 \text{ km s}^{-1}$  component. These detections are almost twice the number detected by Shimoikura et al. (2015), primarily as a result of the higher resolution of the JCMT. Of this total, five are confirmed as outflows using the criterion of Hatchell et al. (2007), whereby the line wing is required to have an intensity greater than  $3\sigma$  at  $\pm 3 \text{ km s}^{-1}$  from the bulk cloud. The two most significant outflows of each cloud are presented in Figure E2. R10-6 and B5-4 have linewidth widths of  $3.5 \text{ km s}^{-1}$  and  $8.7 \text{ km s}^{-1}$ , respectively. A further seven candidate outflows have a notable asymmetry in their line profiles but have too much noise to be confirmed. Eight objects are displaced components with no line asymmetries or wing-like features. Three are noise artefacts or have very low SNRs.

Of the 12 outflow-like detections, 11 have nearby protostars identified in our composite YSO catalogue (Figure E1). Due to the complexity of the region and lack of observations from the inner wings of the cloud it would be premature to infer that the completeness of our Class 0/I protostellar population is near 100%. We conclude that the  $10 \text{ km s}^{-1}$  CO filament is likely shocked shell material around the H II region and we cannot rule this shell out as a source of many of the weaker candidate outflows near OS1a and IRS 5. There is evidence that significantly powerful protostellar outflows can contribute additional localised heating of dust through shocks (Buckle et al., 2015). Outflows have been detected in the W40 complex by Zeilik & Lada (1978) and more recently van der Wiel et al. (2014) found red and blue shifted line wings in the eastern Dust Arc. Our HARP data extend this coverage to the whole of the Dust Arc and W40-N (Figure 3).

We detect 12 potential molecular outflows which are presented in Figure E1. The highest

velocity line-wing offset is  $8.7 \text{ km s}^{-1}$  and is recorded in outflow B5-4 which is associated with a protostar in W40-SMM2. Line-wings found in Serpens Main by Graves et al. (2010) are detected out to  $-30 \text{ km s}^{-1}$  and  $+37 \text{ km s}^{-1}$  from an ambient cloud of similar velocities to the W40 complex. We conclude that the outflows in the W40 complex are relatively weak and that the radiative heating from outflows is negligible, relative to the levels of the radiative feedback from the protostar itself.

We conclude that many of the line-wing detections in Figure E1 are likely caused by shocks related to this wave as opposed to protostellar outflows.

Some of the most prominent outflows we detect are found in the western Dust Arc. For example, Figure E1 shows the outflow B5-4 subtending  $3''$  (0.43 pc) in length from the the protostar W40-MM5 (Maury et al., 2011) in W40-SMM3. As discussed in Section 6.1[UPDATE], the size of these linewings are not particularly exceptional. Given a clump mass of  $12.5 \pm 2.6 M_{\odot}$ , we would anticipate low-to-intermediate mass star-formation is occurring. W40-SMM2 is the only significant clump in the western Dust Arc that does not have a protostar recorded in our composite YSO catalogue. In addition, no significant CO line-wing emission is detected, suggesting that this clump is indeed starless.

The  $^{13}\text{CO}$  2–1 emission (Figure E1) shows many line-wing sources to the north and south of W40-SMM1 from both the  $5$  and  $10 \text{ km s}^{-1}$  clouds. It is not possible to assign individual outflows to protostars, or to rule out that the line-wings could be caused by shocked gas swept up in a shell where the H II region interacts with the filament. The absence of CO line-wing sources in the vicinity of the YSOs near OS2b does suggest that either; these are particularly low-mass protostars with weak outflows, the majority of the  $^{13}\text{CO}$  2–1 has been photo-ionised by the H II region, or that the protostars detected here are false detections.

## 3.8 Conclusions

1. We find evidence for significant levels of  $^{12}\text{CO}$  3–2 line emission in HARP data that contaminates the  $850 \mu\text{m}$  band range between  $3$  and  $10\%$  in the majority of the filaments. In a minority of areas contamination reaches up to  $20\%$ . Removing the  $^{12}\text{CO}$  3–2 contamination significantly increases the calculated dust temperatures, beyond the calculated uncertainties.

# 4

## Free-Free contamination

In this chapter we examine the arguments for a thermal Bremsstrahlung, or free-free, contribution to the SCUBA-2 detections, addressing questions regarding the source, strength, spectral index, and location of the turnover (from partially opaque to optically thin) of free-free emission. We examine the various sources of free-free emission in the JCMT GBS and asses the magnitude of the contribution of free-free to SCUBA-2 bands.

### 4.1 Introduction to thermal breemstralung emission

Thermal Bremsstrahlung, or free-free, emission is a thermal process by which photons are produced from electron scatter in a plasma in LTE. We derive the spectral index of the free-free emission by first considering the number of electrons,  $N_e$ , passing an ion, per unit time. The electrons have a speed range  $v$  to  $v + dv$  and the the ion has an impact parameter of  $b$  to  $b + db$  such that

$$N_e(2\pi b db)v f(v) dv. \quad (4.1)$$

In this system the number of ‘encounters’,  $N(v, b)$ , between the ion and an electron, per unit volume, per unit time, is

$$N(v, b) dv db = (2\pi db)[v f(v)] N_e N_i, \quad (4.2)$$

and the average energy per unit frequency,  $W_\nu$ , is

$$W_\nu \approx \frac{\pi^2}{2} \frac{Z^2 e^6}{c^3 m_e^2} \left( \frac{1}{b^2 v^2} \right) \quad (4.3)$$

where the above constants have their usual meanings. From radiative transfer, the emission coefficient,  $\epsilon_\nu$ , can be calculated by integrating energy and encounters over  $b$  and  $\nu$  as such,

$$4\pi\epsilon_\nu = \int_{b=0}^{\infty} \int_{\nu=0}^{\infty} W_\nu(\nu, b) N(\nu, b) d\nu db. \quad (4.4)$$

Considering non-relativistic Maxwellian distribution of electron velocities,

$$f(v) = \frac{4v^2}{\sqrt{\pi}} \left( \frac{m_e}{2k_B T_e} \right)^{3/2} \exp\left(-\frac{m_e v^2}{2k_B T_e}\right), \quad (4.5)$$

the free-free emission coefficient can be derived as

$$\epsilon_\nu = \frac{\pi^2 Z^2 e^6 N_e N_i}{4c^3 m_e^2} \left( \frac{2m_e}{\pi k_B T_e} \right)^{1/2} \ln\left(\frac{b_{max}}{b_{min}}\right). \quad (4.6)$$

The minimum and maximum impact parameters,  $b_{min}(\nu)$  and  $b_{max}(\nu, \nu)$ , make up the Gaunt factor,

$$g_{ff}(\nu, T) = \frac{\sqrt{3}}{\pi} \ln\left(\frac{b_{max}}{b_{min}}\right), \quad (4.7)$$

that value of which ranges as  $g_{ff}(\nu) \propto 1/\nu$  between 1 and 10 across the radio spectrum. Using Kirchoff's law ( $\kappa_\nu = \epsilon_\nu / B_\nu(T)$ ) the absorption coefficient,  $\kappa_\nu$ , can be calculated in the Rayleigh-Jeans limit as

$$\kappa_\nu = \frac{1}{\nu^2 T^{3/2}} \frac{\pi^3}{\sqrt{48}} g_{ff} \left[ \frac{Z^2 e^6}{c} N_e N_i \frac{1}{\sqrt{2\pi(m_e k_B)^3}} \right]. \quad (4.8)$$

Because the Gaunt factor is weakly inversely proportional to frequency the opacity of free-free emission can be approximated to  $\kappa_\nu \propto \nu^{-2.1}$  (Oster, 1961; Altenhoff et al., 1970) and as a result the optical depth of the free-free can be written as

$$\tau_\nu \approx \int \frac{N_e^2}{\nu^{2.1} T^{3/2}} ds. \quad (4.9)$$

From this expression it can be determined that at low frequencies  $\tau_\nu \gg 1$  and emission will become optically thick. Likewise at very high frequencies emission will become optically,  $\tau_\nu \ll 1$ . Considering the equation of flux density from radiative transfer,

$$S_\nu = \int_{\Omega} B_\nu(T, \nu) \tau d\Omega, \quad (4.10)$$

it is possible to show that free-free emission at very low frequencies will resemble a black body where  $S_\nu \propto \nu^2$ . Likewise at very high frequencies free-free emission is approximately flat,  $S_\nu \propto \nu^{-0.1}$  (Mezger & Henderson, 1967).

At  $\tau_\nu = 1$  free-free emission will undergo a ‘turnover’ from the optically thick to thin regime, typically at low frequencies around KHz regime. At very high frequencies another break occurs in the spectrum when  $h\nu \gg k_B T_e$  and the free-free spectrum goes from flat to an exponential

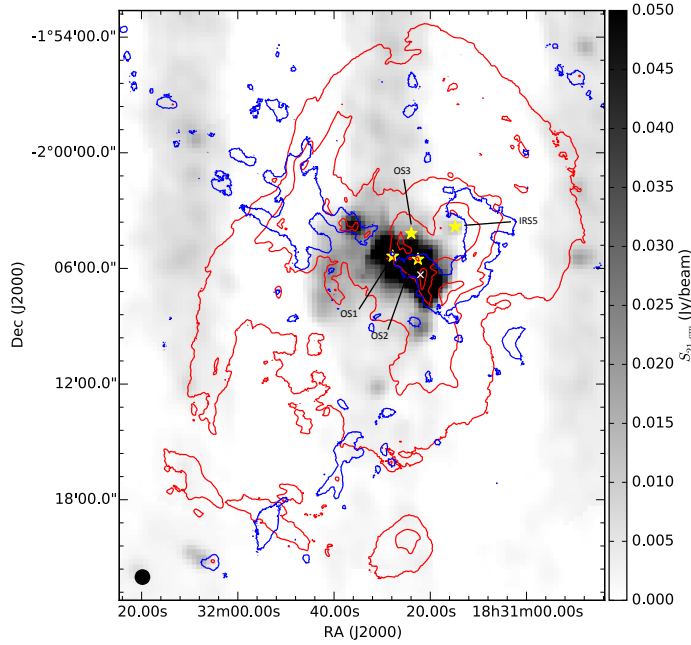


Figure 4.1: Archival VLA 21 cm NRAO VLA Sky Survey (Condon & Kaplan, 1998) continuum map of the W40 complex HII region (45'' resolution). Red *Herschel* 70 μm contours of the nebulousity SH-64 at 300, 1200, 4800, 12000 MJy/Sr. Blue SCUBA-2 850 μm contours of the dust cloud at the 5σ level. Yellow stars indicate the locations of the OB stars, with the O9.5 star OS1 the primary ionising object of the region. The white cross indicates the peak of the VLA 21 cm emission.

decay that is described by,

$$J_{\nu,T} \propto T^{-1/2} \exp\left(\frac{-h\nu}{k_B T_e}\right) N_e^2 g_{ff}(\nu, T), \quad (4.11)$$

where  $J_{\nu,T}$  is the emissivity [CITE]. For an electron temperature of 10<sup>4</sup> K, the exponential decay break can be estimated at occurring shortward of 1 μm.

## 4.2 HII observations

In star formation, free-free emission is typically observed from HII regions formed by photoionisation of molecular hydrogen by UV photons from B4V stars or earlier. The UV, or Lyman, photon density,  $N_{Ly}$ , required to maintain the ionisation of an HII region is given by Kurtz et al. (1994) as

$$N_{Ly} \geq 8.04 \times 10^{46} T_e^{-0.85} U^3, \quad (4.12)$$

where U is the excitation parameter  $R_s N_e^{2/3}$  for a Stromgren sphere of radius  $R_s$ . These two variables are also related through

$$N_{Ly} = \alpha_H N_e^2 \frac{4}{3} \pi R_s^3 \quad (4.13)$$

where  $\alpha_H$  is the hydrogen recombination rate, approximately equal to  $3 \times 10^{-13} \text{ cm}^3 \text{ s}^{-1}$ . H II regions are large scale, low density structures with radii greater than  $10^{18} \text{ cm}$  and  $N_e$  less than  $10^4 \text{ cm}^{-3}$ . The stellar  $N_{Ly}^*$  for the OB stars capable of producing H II regions is typically greater than  $10^{46} \text{ cm}^{-3}$ . By considering  $N_{Ly}^*$  at specific frequencies Kurtz et al. (1994) calculates the flux density that would be observed if viewing an H II region at a distance,  $d$ , using

$$S_\nu(\text{Jy}) = 1.32 \times 10^{-49} \xi N_{Ly}^* a(\nu, T) \left( \frac{\nu}{\text{GHz}} \right)^{-0.1} \left( \frac{T_e}{\text{K}} \right)^{0.5} \left( \frac{d}{\text{kpc}} \right)^{-2}, \quad (4.14)$$

where  $a(\nu, T)$  is a constant equal to 0.98 (Mezger & Henderson, 1967) and  $\xi$  is the fraction of UV photons not absorbed by the dust set at 10%. Free-free emission from large scale, diffuse H II regions is predicated to be optically thin at radio frequencies emission where the power law becomes approximately flat with an  $\alpha_{\text{ff}} = -0.1$  (Oster, 1961; Mezger & Henderson, 1967).

In an H II region UV heat up the gasses and plasma of the ISM by radiative transfer to temperatures in excess of 10000 K. This causes the exposed material to expand adiabatically into the space surround the OB star/s. In the transition zone between the H II region and the neutral ISM two fronts are observed; the ionisation front [CITE] and the shock [CITE]. In the shock front, expansion of the H II region is thought to sweep up the ISM producing localised over densities associated with a ‘shell’ of material around the H II region [CITE]. Whether the shock front has sufficient pressure to destabilise existing cores within any exposed filaments and ‘trigger’ star-formation is an open question (Lefloch & Lazareff, 1994; Urquhart et al., 2009). The ionisation front represents a region where neutral material is being ionised through exposure to UV photons. Rate of ionisation is heavily dependant on the local density. High density regions take considerably longer to break down than lower density regions and as a result ‘champagne’ flows (Dale et al., 2012) are observed where the molecular cloud has been ruptured by an internal H II and photons are exiting through a narrow opening. The H II region can be further imbedded by accretion flow of neutral material onto the star Dale et al. (2005); Dale & Bonnell (2011) and by gravity when at the centre of massive cloud Yorke et al. (1989). The region in-between the ionisation front and shock front is collectively known as a photo-dissociative region (PDR, Thompson et al. 2004). An example of a PDR is observed in Perseus, a star forming region observed as part of the JCMT GBS.

### 4.3 UCH II observations

In addition to these large scale structures, free-free emission is also detected in the form of a power law at scale sizes comparable to individual stars (Panagia & Felli, 1975).

Early type OB stars undergoing mass loss through winds produce free-free emission from ionised material leaving the star, in addition to UV photons ionising the ISM, and are considered compact ( $\leq 0.5 \text{ pc}$ ), ultra compact ( $\leq 0.1 \text{ pc}$ ) and hyper compact ( $\leq 0.03 \text{ pc}$ ) H II regions (Wright & Barlow, 1975; Harvey et al., 1979). These are the processors of evolved H II regions (10 pc, Kurtz 2005). From here on in we refer to these classes collectively as UCH II regions. Whereas H II regions are diffuse, homogenous fields of emission, UCH II regions have an electron density is

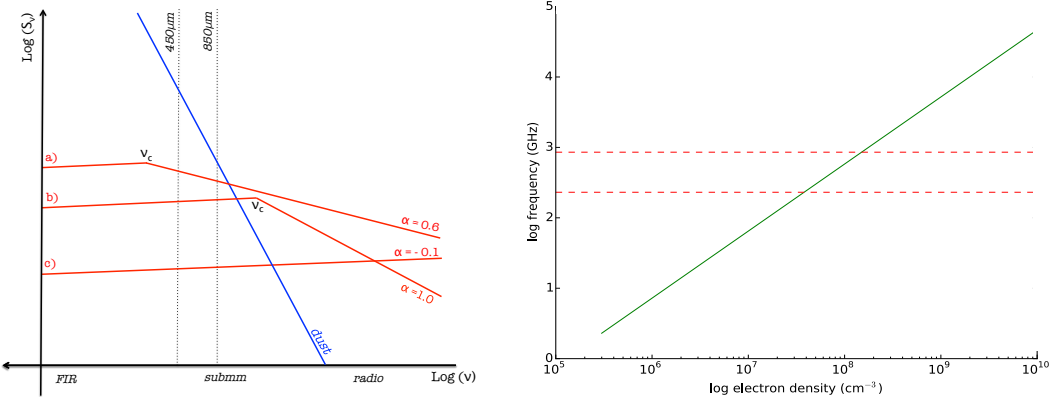


**Figure 4.2: Left]** A schematic of the SED shape for three hypothetical scenarios offig:freefreealpha free-free emission. **Case a)** an UCH II with  $\alpha_{\text{ff}} = 0.6$  has a turnover that occurs short ward of the submillimetre regime, and as a result has a majority contribution to the  $850 \mu\text{m}$  band and a significant contribution to the  $450 \mu\text{m}$  band. **Case b)** a YSO emits free-free emission,  $\alpha_{\text{ff}} = 1.0$ , from a collimated jet. However the spectrum turns over to the optically thin regime long ward of submillimetre wavelengths, and consequently free-free emission contributes roughly equally to both SCUBA-2 bands. **Case c)** a H II region has free-free emission from diffuse gas of  $\alpha_{\text{ff}} = -0.1$  that outshines that from compact objects at long wavelengths. However, the flat spectrum means that at submillimetre wavelengths the emission is all but negligible. **Right]** Free-free turnover as a function of launching electron density (as described by Olnon 1975 in Equation 4.15). Dashed lines indicate the submillimetre regime (1.3 mm to  $350 \mu\text{m}$ ).

inversely proportional to radius. Assuming spherical winds of constant velocity Panagia & Felli (1975) and Wright & Barlow (1975) derive the spectral index of the free-free emission as  $\alpha_{\text{ff}} = 0.6$ . Large surveys of UCH II candidate regions are consistent with this result (Harvey et al., 1979; Wood & Churchwell, 1989; Kurtz et al., 1994; Molinari et al., 1998; Walsh et al., 1998; Kurtz, 2005).

Where the free-free emission mechanism is a spherical ionised stellar wind, Emission can be thought of as *partially thick* with lower frequencies probing greater depths of emission within the wind before becoming fully optically thin at shorter wavelengths where only the diffuse H II region is being observed. The exact location of this free-free turnover,  $\nu_c$ , has been much debated in the literature. If the turnover occurs short-ward of submillimetre wavelengths then it is possible that the free-free may contribute in part to SCUBA-2 observations of dust emission. Olnon (1975) defines  $\nu_c$  as a function of electron density,  $N_e(R) = N_{e,0}$  where  $r \leq R$ , as

$$\log_{10} \nu_c = -0.516 + \frac{1}{2.1} \log_{10} \left( \frac{8}{3} R N_{e,0}^2 T_e^{-1.35} \right), \quad (4.15)$$

where  $R$  is the launching radius of the wind (typically 10 AU) and  $T_e$  is the electron temperature (typically  $10^4$  K). Figure ?? highlights how a turnover point short wards of the submillimetre regime requires an electron density in excess of  $10^8 \text{ cm}^{-3}$ .

The electron density  $n_0$  is not easily determined from observations. We therefore turn to indirect measurements to make a general statement about what systems will produce free-free emission that is opaque at submillimetre wavelengths and hence may subsequently be contributing

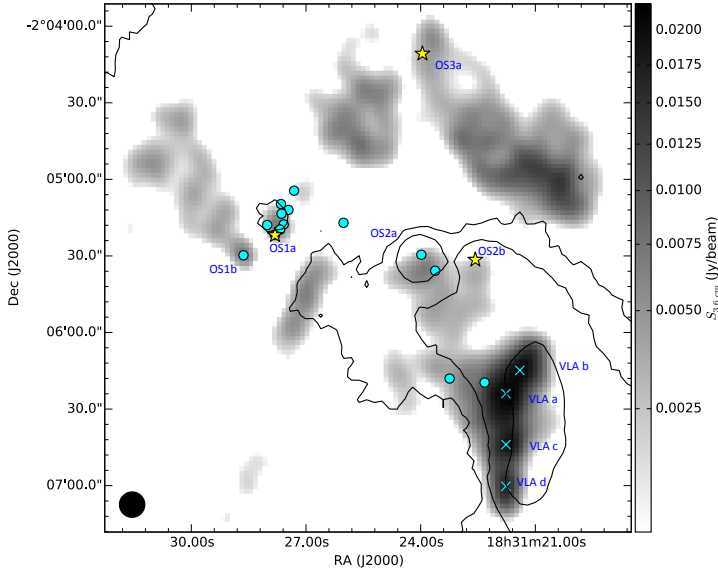


Figure 4.3: Archival AUI/NRAO 3.6 cm map of the W40 complex OB association (NRAO/VLA Archive Survey, (c) 2005-2007). SCUBA-2 850  $\mu\text{m}$  contours of dust emission at  $5\sigma$ ,  $15\sigma$  and  $50\sigma$  overlaid. Yellow markers indicate the locations of the OB stars while cyan circles indicate the location of compact radio sources identified by Rodriguez et al 2010. Cyan crosses mark the four peaks identified separately in the AUI/NRAO 3.6 cm map.

to SCUBA-2 emission. We assume that  $n_0$  is proportional to stellar mass and by association varies with spectral class as the more massive stars are known to produce more vigorous winds and greater mass loss. Sandell et al. (2011)'s results indicate that the free-free contribution is significant for early B stars in their sample, but not for late B and A class stars. MWC 297 is the lowest mass star in their sample for which free-free contributes at SCUBA-2 wavelengths and we therefore mark it as a lower limit of stellar class. MWC 297 has a luminosity of  $3 \times 10^3 L_\odot$  (Drew et al., 1997) which corresponds to a class B1.5Ve or B4V star. Given the nature of these assumptions, we are limited to assigning an upper estimate of spectral class B4V, above which the free-free turnover can occur in the submillimetre regime.

UCH II are associated with stars that are sufficiently massive (greater than  $8M_\odot$ ) that their Kelvin-Helmholtz contraction timescale is shorter than their free fall and accretion timescale (Manoj et al., 2007). These stars reach the main sequence and start producing ionising radiation whilst still embedded within their protostellar envelope (McKee & Tan, 2003). This would then lead to a compact region of highly ionised winds, as detected by Malbet et al. (2007) and Drew et al. (1997). We follow Wood & Churchwell (1989)'s description of an UCH II region as region with electron density greater than  $10^4 \text{ cm}^{-3}$  within a diameter of less than 0.1 pc. The minute size of the UCH II region means they cannot be detected optically and are interest observed through free-free processes or the indirect heating of dust. The lifetime of the ultra-compact stage of an H II region is estimated at  $4 \times 10^5$  years, approximately 10% the lifetime of a typical O star.

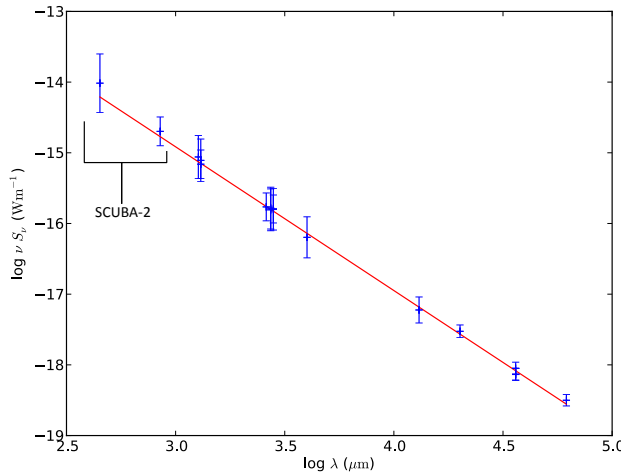


Figure 4.4: The Spectral Energy Distribution of MWC 297 from submillimetre to radio wavelengths. SCUBA-2 fluxes (found using aperture photometry as described in Section 5.2.) are presented alongside those collated by Sandell et al. (2011) who fit a power law  $\alpha = 1.03 \pm 0.02$ , consistent with free-free emission from an UCHII region and polar jets or outflows.

### 4.3.1 Jets

A minority of radio bright young OB stars are observed with  $\alpha_{\text{ff}} \geq 0.6$ , for example MWC 349 (Olon, 1975), MWC 297 Skinner et al. (1993); Sandell et al. (2011) and AB Aur (Rodríguez et al., 2014). Reynolds (1986) provides a comprehensive examination of models for stellar winds and finds that, where the outflow is highly collimated and accelerating (as this the case of bi-polar jets) the spectral index becomes increasingly opaque with  $\alpha_{\text{ff}} \simeq 1.0$ . [CAN DERIVE IF NECESSARY BUT ITS PRETTY OVERKILL].

MWC 349 (Tafoya et al., 2004; Sandell et al., 2011) and MWC 297 (Sandell et al., 2011; Rumble et al., 2015) are early B-class Herbig stars where empirical observations have suggested that the free-free emission is sufficiently bright and opaque that it dominates over the dust emission at submillimetre wavelengths and produces a distinct point source in the observations consistent with a compact object. If similar point sources are present the SCUBA-2 observations of W40 complex, and are also consistent the location of whole compact radio sources, that could well signify the potential for free-free contribution.

## 4.4 Free-free contribution to SCUBA-2

Where free-free emission is significantly bright and remains optically opaque up to submillimetre wavelengths it may be detected by SCUBA-2 in the 450 and 850  $\mu\text{m}$  bands.

Harvey et al. (1979), Kurtz et al. (1994) and Sandell et al. (2011) present multi-wavelength radio surveys of numerous HAeBe systems. A number of A class and late B class stars have faint free-free UCH II detections that appear to become optically thin long-ward of the submillimetre regime or are otherwise negligible when compared to emission at from the dust in the protostellar disc or envelope. Rodríguez et al. (2014) finds evidence that free-free emission in AB Aur has



in MWC297/mwc297<sub>a</sub>rXiv/MNRAS/20140618<sub>mwc297</sub>contamination.jpeg

Figure 4.5: IR1 SCUBA-2 850  $\mu\text{m}$  data before *left* and after *right* removal of free-free contamination from an UCHII region and polar jets/winds (represented by the point source contours in the *left* plot). SCUBA-2 contours are at 0.011, 0.022, 0.033 and 0.055 Jy/pixel (corresponding to 5, 10, 15 and 25  $\sigma$  detection limits). 6 cm VLA contours (red) from Sandell (private comm.) at 0.002, 0.005, 0.02, 0.072, 0.083 Jy/beam are overlaid on the left hand panel. The location of MWC 297 is marked with a star. Beam sizes are shown at the bottom of the image (VLA CnD config. *left* and JCMT *right*.)

index  $\alpha_{\text{ff}} = 1.1$  at cm wavelengths, however flux becomes optically thin by 1.3 mm, leading to the conclusion that  $\nu_c \sim 70$  GHz. The early B systems of MWC 349, MWC 279 and LkH $\alpha$  101 are observed to have strong free-free wind or jet emission which fits a power law right up to the submillimetre where the free-free provides a substantial, if not the majority of emission at these wavelengths. Olnon (1975) calculates that  $\nu_c \sim 575$  GHz for MWC 349 using Equation 4.15, given that  $R \sim 11$  AU and  $N_{e,0} \sim 9 \times 10^8 \text{ cm}^{-3}$  (Greenstein, 1973). Harvey et al. (1979) goes further and argues that free-free emission may be opaque up to 100  $\mu\text{m}$ .

We present our methods for calculating and subtracting the free-free contribution from SCUBA-2 data published in Rumble et al. (2015) and Rumble et al. (2016, in prep.).

#### 4.4.1 Direct methods

Skinner et al. (1993) studied free-free 3.6 cm and 6.0 cm radio emission from stellar winds around the B1.5ve star MWC 297 and found a power law of the form  $S_\nu \propto \nu^\alpha$  where  $\alpha$  is equal to 0.6238 in the optically thin regime. Sandell et al. (2011) extended the study down to 3 mm and revised the spectral index to  $\alpha = 1.03 \pm 0.02$  which is consistent with a collimated jet component to free-free emission. The free-free power law extends into the submillimetre spectrum; however, at wavelengths shorter than 2.7 mm there is potential for a thermal dust component in the observed flux, so submillimetre flux is not included in the calculation of  $\alpha$ .

Figure 5.4 displays 6 cm radio emission from the VLA CnD configuration in conjunction with SCUBA-2 850  $\mu\text{m}$  data (Skinner 1993, Sandell priv. comm.). Both sets of data show peaks in emission which are coincident with a point source at the location of the star MWC 297 in 1 mm and 3 mm data presented by Alonso-Albi et al. (2009). The peak of the SCUBA-2 850  $\mu\text{m}$

emission in Figure 5.4 is 86 mJy/pixel, consistent with the SCUBA 850  $\mu\text{m}$  value of 82 mJy/pixel (Alonso-Albi et al., 2009).

The VLA data also show extended emission to the north and south of MWC 297 which is consistent with polar winds or jets. The intensity of emission is significantly weaker than that of the UCHII region. Considering the elongated beam shape of the VLA CnD observations ( $21.1'' \times 5.2''$ , PA=  $-61^\circ.3$ ) accounts for much the E/W elongation of the emission. In addition to this, Manoj et al. (2007) describe this emission as coming from within 80 AU of MWC 297. This is much smaller than the JCMT beam and therefore we model the dominant free-free emission from MWC 297 as a point source.

By taking the revised power law least square fit to Skinner et al. (1993) and Sandell et al. (2011)'s results at radio and millimetre wavelengths and extrapolating to the submillimetre wavelengths of SCUBA-2, we are able to calculate the effect of free-free emission due to a point-like UCHII region as an integrated flux of  $934 \pm 128$  mJy at 450  $\mu\text{m}$  and  $471 \pm 62$  mJy at 850  $\mu\text{m}$ . Single pixels with these values were then implanted into blank SCUBA-2 450 and 850  $\mu\text{m}$  PONGs and the map convolved with the JCMT beam to produce an SCUBA-2 free-free emission map. These are subtracted off of the original SCUBA-2 maps to leave a SCUBA-2 dust map.

In addition to small scale free-free structures that are modelled as point sources, we can also run a free-free subtraction for large-scale emission from the diffuse emission from the H II region.

Archival VLA 21 cm data ( $45''$  resolution) is presented in Figure 4.1 and shows the location of the  $1.7'$  large scale H II region associated with SH-64 (Condon & Kaplan, 1998). Rodney & Reipurth (2008) presents a summary of observations at multiple radio wavelengths and conclude a flat spectral index ( $\alpha = -0.1$ ) as expected from homogenous, optically thin free-free emission as predicted by Oster (1961) and Mezger & Henderson (1967).

Using a simple gaussian we convolve the SCUBA-2 850  $\mu\text{m}$  up to the  $45''$  resolution of the VLA data so the fluxes are comparable. Likewise we re-grid the data on to a common pixel size. SCUBA-2 data has large scale structure greater than  $5'$  removed during the data reduction process so we use the FINDBACK tool (see Section 2) to mimic the process on the VLA data. The VLA fluxes are subsequently scaled up to 850  $\mu\text{m}$  following an  $\alpha = -0.1$  before they are subtracted from the SCUBA-2 observations.

#### 4.4.2 Indirect methods

In the previous section we were able to combine observations across a range of wavelengths to directly and accurately calculate the free-free spectral index. Other regions have been less well studied in high resolution and radio catalogues exist only for single wavelengths from which it is not possible to directly calculate  $\alpha_{\text{ff}}$ . In order to get around this problem we can assess the radio properties of any free-free sources to determine whether or not it can be classified as H II, spherical wind UCHII or collimated jet UCHII region. By considering the spectral class (if known) of the source and SCUBA-2 observations we can also make a judgement on whether or not any free-free emission is optically thick or thin at submillimetre wavelengths. In this way we can indirectly estimate the extent the free-free contribution to SCUBA-2 observations in more regions.

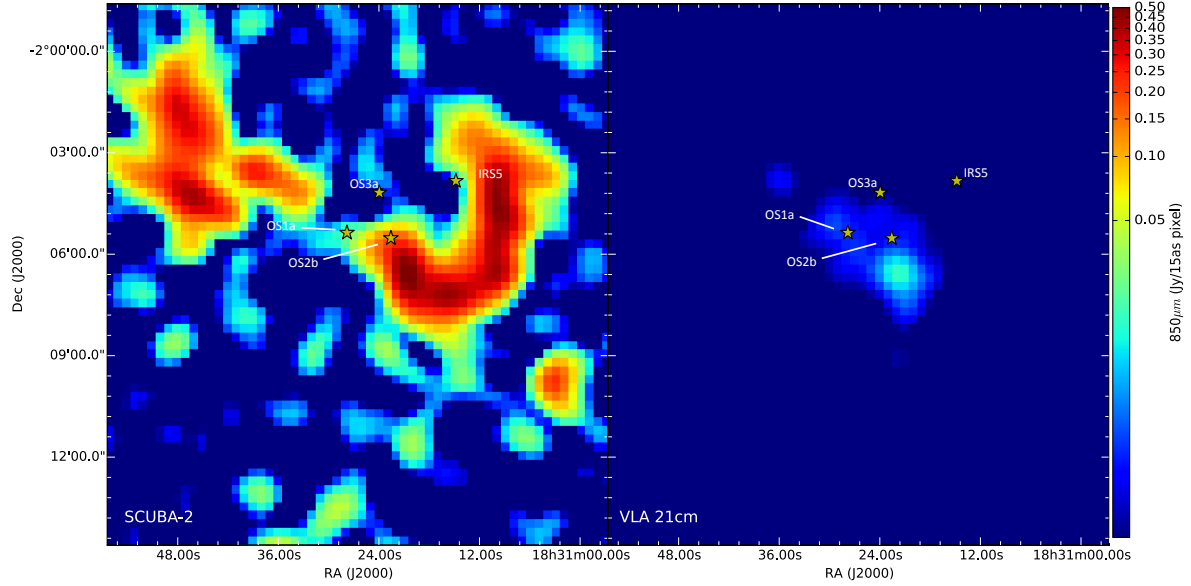


Figure 4.6: The free-free contribution from large-scale H II gas, modelled using archival VLA 21 cm observations (Condon & Kaplan, 1998) assuming  $\alpha_{\text{ff}} = -0.1$  (right), compared to SCUBA-2 dust emission at 850  $\mu\text{m}$  (left). Maps have common 15'' pixels and 45'' resolution. Markers indicate the locations of the OB stars.

Table 4.1: Summary of radio findings on bright objects in W40.

Source	2MASS ID	Type	Time variable 3.6 cm?	Associated jet?	SCUBA-2 point source?	Free-free optically th
OS 1a (North)	18312782-0205228	Herbig AeBe	N	N	Y	?
OS 1a (South)	18312782-0205228	O9.5	-	N	Y	-
OS 1b	18312866-0205297	Class II	N	Y	N	N
OS 1c	18312601-0205169	Class II	Y	N	N	N
OS 2a	18312397-0205295	Herbig AeBe	Y	?	Y	?
OS 2b	18312257-0205315	B4	Y	N	Y	?
OS 3a	18312395-0204107	B3*(binary)	-	-	N	-
IRS 5	18311482-0203497	B1	-	-	N	N

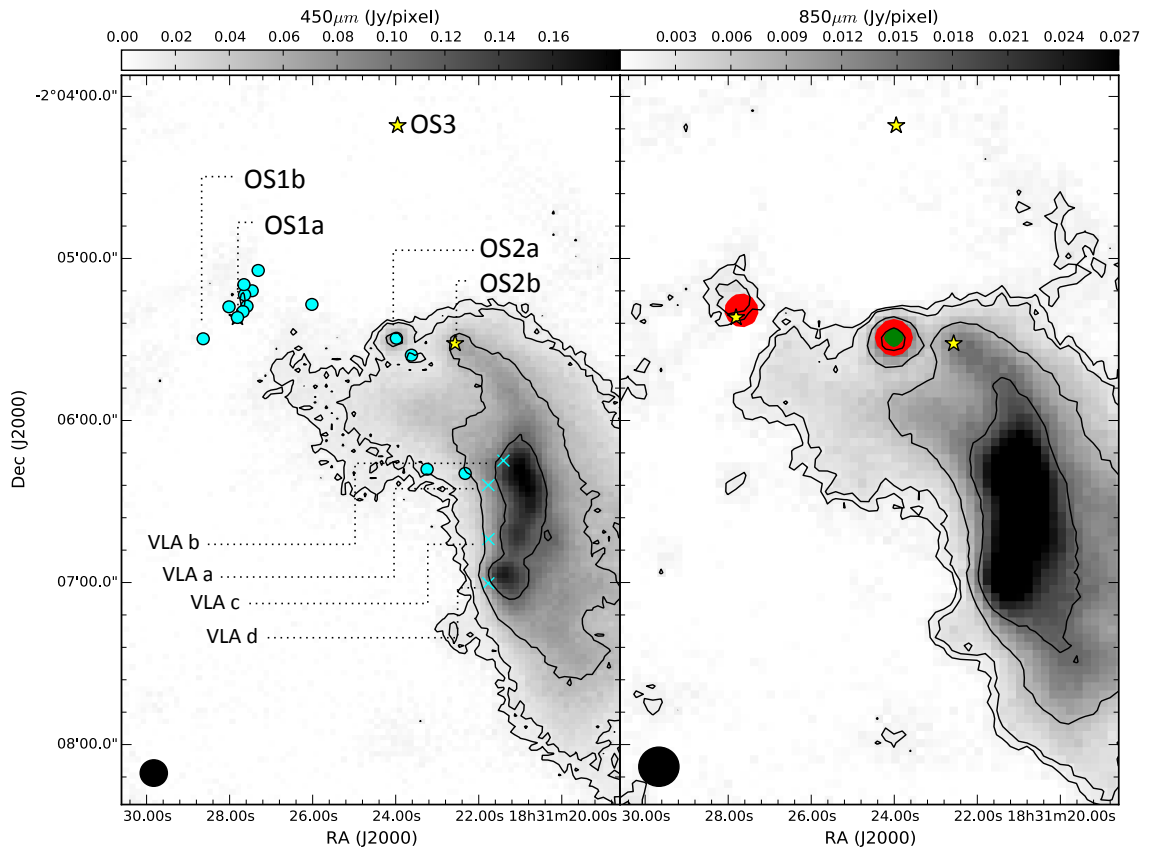


Figure 4.7: The free-free contribution of compact radio sources OS1a and OS2a at  $450\text{ }\mu\text{m}$  (left) and  $850\text{ }\mu\text{m}$  (right), modelled as point sources extrapolated from the Rodriguez et al. 2010  $3.6\text{ cm}$  fluxes with assumed spectral indices given in Table 4.3. Yellow markers with thick outlines indicate the locations of the OB stars, cyan circles the location of all the Rodriguez et al. 2010 compact radio sources and cyan crosses the location of four peaks identified separately in the AUI/NRAO  $3.6\text{ cm}$  map ( $450\text{ }\mu\text{m}$  only). Black contours trace SCUBA-2 data at  $3\sigma$ ,  $5\sigma$ ,  $15\sigma$  and  $30\sigma$ . Red and green filled contours trace the free-free contribution at  $3\sigma$  and  $5\sigma$  from optically thick (see Table 4.1).

In the W40 complex archival AUI/NRAO 3.6 cm data is used and presented in Figure 4.3. The coverage of this region is limited approximately  $5'$  and resolution of  $9.97''$  is comparable to SCUBA-2. As a result AUI/NRAO 3.6 cm is not able to resolve individual sources but can pick up extended radio emission associated with outflows. Rodríguez et al. (2010) supplement these data with high-resolution photometry at the same wavelength but with a reduced coverage of  $4'$ .

No additional observations of alternative wavelengths at comparable resolution are available to this author, therefore it is not possible to empirically measure the free-free spectral index and we turn to indirect methods to infer  $\alpha_{\text{ff}}$ . This requires examining the evidence for sufficient electron density,  $N_e$ , for any free-free emission to remain optically thick up to the submillimetre regime, and for features that hint that the host star may power a jet.

The W40 complex contains a number of massive star and Shuping et al. (2012) conduct a NIR study of the brightest objects in W40, identifying a list of one late O star, 3 B stars, 2 Herbig AeBe stars and 2 low mass Class III YSOs. These objects are listed in Table 4.1 and build on early IR studies by Smith et al. (1985). Rodríguez et al. (2010) resolves 20 compact radio sources, 15 of which are consistent with 2MASS sources and, by using time-variability, is able to classify 8, variable, YSOcs and 7, non-variable, UCH II candidate regions. Rodríguez et al. (2010) also identify non-compact radio sources without IR counterparts and these are interpreted as shock fronts from thermal jets that were likely formed by the local HAeBe stars OS1b and OS2a/b.

The example early B systems of MWC 349, MWC 279 and LkH $\alpha$  101 (Sandell et al., 2011) all have free-free emission that is opaque at submillimetre wavelengths which can be identified as a bright peak in SCUBA observations. The lack of a bright submillimetre point source consistent with the candidate UCH II would likely signify that free-free emission turns over too early, or that emission is not bright enough to have a significant impact on the total flux density observed by SCUBA-2. This test immediately rules out OS1b, c, OS3a and IRS 5 from having significant UCH II regions as they are not detected in SCUBA-2 at either wavelength.

OS1 and OS2a, presented in Figures 4.1 and 4.3 have coincident SCUBA-2 emission so in these cases we make the initial assumption that 100% of emission at SCUBA-2  $850 \mu\text{m}$  is produced by free-free and measure the subsequent spectral index. This initial assumption is subsequently adjusted until a spectral index that fitted a model of  $\alpha_{\text{ff}} \sim -0.1, 0.6$  or  $1.0$ . Photometry from SCUBA-2 450 and  $850 \mu\text{m}$  and AUI/NRAO 3.6 cm maps was conducted with a  $14.5''$  aperture (the SCUBA-2  $850 \mu\text{m}$  beam FWHM). Rodríguez et al. (2010) also detects time variability of radio emission from a number of radio sources in the W40 complex, concluding that a variable detection is symptomatic of episodic accretion processes and non-variable emission are a result of an UCH II region. They also detect a number of irregular radio without an IR detection which they interpret at shocks from jet outflows. We use these as further tools to indirectly infer whether or not a YSO has an UCH II region and/or jet.

OS1 is a close cluster of objects that are not resolved by SCUBA-2 or the AUI/NRAO beam but are listed as a number of objects in Rodríguez et al. (2010), four of which have non-variable emission indicating an UCH II region. There is also no significant emission at  $450 \mu\text{m}$  which suggests that if there is any free-free contribution at  $850 \mu\text{m}$ , the emission has become optically thin by  $450 \mu\text{m}$ . An  $\alpha_{\text{ff}} = 0.6$  represents emission of  $6.36 \text{ mJy}$  of free-free at  $850 \mu\text{m}$ , a

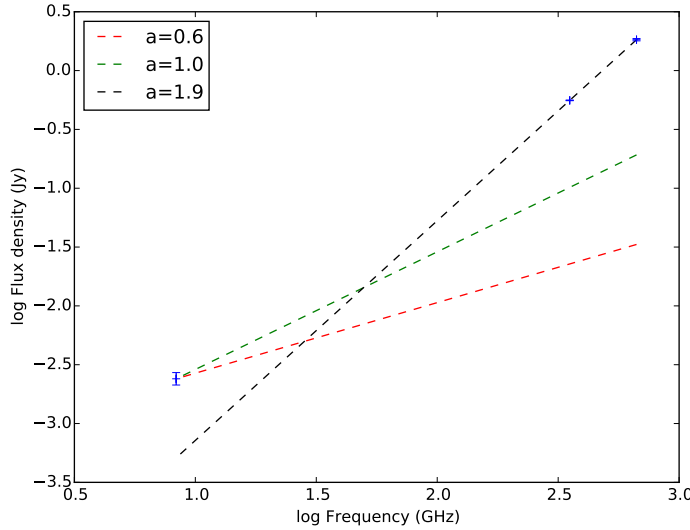


Figure 4.8: Modelling free-free emission in OS2a from the Rodriguez et al. (2010) 3.6 cm data for a given  $\alpha_{\text{ff}} = 0.6$  (red), 1.0 (green), and the observed dust spectral index (black).

50% contribution. This result is consistent with the presence of HAeBe stars in the cluster. No jet shocks are found in the vicinity of the cluster and so we rule out the collimated jet configuration of free-free emission.

OS2a is a single HAeBe star that is resolved as a strong point source by SCUBA-2 at both 450  $\mu\text{m}$  and 850  $\mu\text{m}$ . Rodríguez et al. (2010) does resolve both OS2a at 3.6 cm and therefore these fluxes are used to complete the contribution test. Two results are returned; an  $\alpha_{\text{ff}} = 0.6$  represents a 5% contribution (1.86 mJy) and an  $\alpha_{\text{ff}} = 1.0$  represents a 22% contribution (8.18 mJy). OS2a is variable in nature but it also has nearby shock fronts which are consistent with active accretion, so the jet scenario of  $\alpha_{\text{ff}} = 1.0$  appears the more likely outcome. No spectral class is available for this object. Both tests infer that even if the free-free emission is opaque at SCUBA-2 wavelengths, the SCUBA-2 source is remains dominated by dust emission. These results, and others, are summarised in Table 4.1. OS2b has a SCUBA-2 peak at both wavelengths but given its spectral class of B4 we consider it unlikely that any free-free emission will remain optically thick in the submillimetre regime.

In addition to this radio catalogue, we identify four radio peaks in Archival AUI/NRAO 3.6 cm map which were outside of the coverage of Rodríguez et al. (2010) which are marked in Figure 4.3 as VLAa, b, c and d. As there is no clear point source in the SCUBA-2 maps we assume that these additional VLA radio sources are optically thin at these wavelengths and take no further action.

Table 4.2: Summary of free-free contributions to SCUBA-2 wavelengths from MWC 297. The uncertainty on flux density at 450  $\mu\text{m}$  is 0.03 Jy and 850  $\mu\text{m}$  is 0.0025 Jy.

Object	3.6 cm (Jy)		450 $\mu\text{m}$ (Jy)			850 $\mu\text{m}$ (Jy)			$\alpha_{\text{ff}}$	
	VLA <sup>a</sup>	SCUBA-2	Free-free	Dust	%	SCUBA-2	Free-free	Dust	%	
MWC 297	0.0099	0.1886	0.1377	0.0510	73±5	0.0860	0.0709	0.0150	82±4	1.03±0.02

## 4.5 The free-free contribution in Serpens MWC 297 results and discussion.

We determine that free-free emission from an UCHII region and polar jets/winds associated with MWC 297 contaminates the 450  $\mu\text{m}$  and 850  $\mu\text{m}$  data (Skinner et al., 1993). The nature of the free-free emission from the outflow has been debated by various authors. Malbet et al. (2007) and Manoj et al. (2007) argue for ionised stellar winds that dominate at higher latitudes, whereas Skinner et al. (1993) and Sandell et al. (2011) provide evidence for an additional source of free-free emission in the form of highly collimated polar jets. Jets are typically associated with less evolved objects where luminosity is dominated by accretion processes whereas MWC 297 is considered to be a Class III / ZAMS star where the majority of the disk has fallen onto the star or been dissipated by winds.

X-ray flares are thought to be a signature of episodic accretion and Damiani et al. (2006) detect a number of X-rays flares from the Serpens MWC 297 region but find that only 5.5 per cent of total flaring is directly associated with MWC 297, suggesting that accretion onto it is minimal. The majority of X-ray emission is associated with additional YSOs and the companion of MWC 297, OSCA, an A2V star identified by Habart et al. (2003) and Vink et al. (2005) at a separation of 850 AU.

Figure 4.4 and Figure 5.4 show that free-free emission due to an UCHII region and polar winds/jets is responsible for the majority of flux from the star MWC 297. Original peak fluxes of  $188\pm16$  mJy and  $86\pm22$  mJy. Residual dust peak fluxes are  $51\pm10$  mJy and  $15\pm3$  mJy flux per pixel at 450  $\mu\text{m}$  and 850  $\mu\text{m}$  respectively and are highlighted in Figure 4.4 as the flux above the free-free power law fit of  $\alpha = 1.03 \pm 0.02$ . Free-free subtraction increases the residual dust spectral index by 35%. This corresponds to approximately 73±5 per cent and 82±4 per cent of the 450  $\mu\text{m}$  and 850  $\mu\text{m}$  peak flux respectively. Given our estimate of 13 per cent CO contamination, dust emission could potentially account for as little as 5 per cent of peak emission at 850  $\mu\text{m}$ .

The  $5\sigma$  level of 82 mJy and 11 mJy means that flux is too uncertain to be detected at 450  $\mu\text{m}$  and therefore it is not possible to calculate reliable temperatures of the residual circumstellar envelope/disk around the star. The assumption of point-like free-free emission may add further uncertainty to the residual flux. We cannot say whether any dust emission contributes at the position of MWC 297.

Table 4.3: Summary of free-free contributions to SCUBA-2 wavelengths from bright objects in W40. The uncertainty on flux density at  $450\text{ }\mu\text{m}$  is 0.017 Jy and  $850\text{ }\mu\text{m}$  is 0.0025 Jy.

Object	3.6 cm (Jy)			450 $\mu\text{m}$ (Jy)			850 $\mu\text{m}$ (Jy)			$\alpha_{\text{ff}}$
	VLA <sup>a</sup>	SCUBA-2	Free-free	Dust	%	SCUBA-2	Free-free	Dust	%	
OS1 <sup>b</sup>	0.00578	-	-	-	-	0.101	0.064	0.038	62	0.6
OS2a	0.00240	1.83	0.16	1.67	9	0.558	0.069	0.489	12	1.0

<sup>a</sup> VLA 3.6 cm compact object fluxes (Rodríguez et al., 2010).

<sup>b</sup> OS1 covers a cluster for stellar objects where OS1a(North), VLA-12, VLA-14, VLA-16 are all radio emitters. The flux of the most prominent source, VLA-14, is included in this table but in reality the SCUBA-2 free-free flux of OS1 is a combination of all 4 of these objects.

## 4.6 The free-free contribution in the W40 complex results and discussion.

The W40 complex contains a number of massive stars that are detected in high resolution VLA 3.6 cm observations. A large-scale H II region is also observed at lower resolution 21 cm observations.

Figure 4.6 shows how the SCUBA-2 data is subsequently aligned and convolved to the larger resolution of the VLA 21 cm data so the two data sets are directly comparable. Given that free-free emission from the large scale H II region is essentially flat in spectrum, it is not surprising that the contribution is very limited. Peak 21 cm flux density is 0.0298 Jy/pix which corresponds to 0.0163 and 0.0174 Jy/pix at 450 and 850  $\mu\text{m}$  given a spectral index of  $\alpha_{\text{ff}} = -0.1$ . The contribution of this peak flux to the SCUBA-2 observations is 5% at 850  $\mu\text{m}$  and 0.5% at 450  $\mu\text{m}$ . As a result the dust spectral index for the peak increases by 2% from 3.46 to 3.53.

3.6 cm fluxes for OS1 and OS2a are extrapolated up to SCUBA-2 wavelengths (Table 4.3) assuming an indirectly estimated free-free spectral index of 0.6 and 1.0 respectively. Modelled as a point source, the free-free emission from each star is convolved with the JCMT beam using primary and secondary components for comparison with the SCUBA-2 data (Figure 4.7). The contribution of the free-free in OS1a at 850  $\mu\text{m}$  is 62% (no detection at 450  $\mu\text{m}$ ). The free-free contribution for OS2a is 9% at 450  $\mu\text{m}$  and 12% at 850  $\mu\text{m}$ . As a result the dust spectral index for the peak increases by 3%.

Having accounted for possible CO and free-free contamination, the residual flux detected from OS2a is 1.67 and 0.489 Jy at 450  $\mu\text{m}$  and 850  $\mu\text{m}$  respectively. We find that this gives OS2a an usually low spectral index of  $1.6 \pm 0.1$ . Whilst lower  $\alpha$ s have previous been explained by very low  $\beta$  associated with grain growth (Manoj et al., 2007), given a  $\beta=1.0$ , typical for circumstellar disks, an  $\alpha = 1.6$  would require a temperature of less than 2 K. Alternatively, an exceptionally low  $\beta$  approaching 0.0 would still require a temperature of less than 7 K. In both scenarios, dust temperatures this low have never been observed. Therefore the results calculated for OS2a should be considered with a high degree of scepticism.

In summary, the free-free contribution at SCUBA-2 wavelengths is limited (less than 5%) at large scales. At smaller scales it may have a small, but significant (9% to 12%) impact on prominent SCUBA-2 sources such as OS2a and a significant impact (62%) on faint SCUBA-2

sources such as OS1a. Subtraction of the free-free emission from SCUBA-2 observations acts to increase the dust spectral index, by 2% at the peak of large-scale emission and 3% from OS2b.

## 4.7 Conclusions

In this chapter we have examined the impact of free-free contamination on SCUBA-2 observations of star-forming regions of Serpens MWC 297 and the W40 complex. We find a small number of cases in the literature where radio-bright YSOs have free-free emission that is optically thick at submillimetre wavelengths and contributes to SCUBA and SCUBA-2 observations in addition to dust. We develop techniques that are used to subtract this small scale emission from the submillimetre observations and measure the residual dust flux and estimate the contamination fraction. Where insufficient radio observations exist to directly calculate  $\alpha_{\text{ff}}$  we assess the physical characteristics of individual sources to make a judgement on whether they are UCH II regions ( $\alpha_{\text{ff}} = 0.6$ ) or collimated jets ( $\alpha_{\text{ff}} = 1.0$ ). We also apply the same method to large scale, diffuse H II regions with an  $\alpha_{\text{ff}} = -0.1$  to investigate.

Our results are summarised as:

1. The B1.5ve Herbig HAeBe star MWC 297 in the Serpens MWC 297 region has a free-free spectral index of  $\alpha_{\text{ff}} = 1.03 \pm 0.02$ , consistent with collimate jet geometry. SCUBA-2 peak fluxes of  $188 \pm 16$  mJy and  $86 \pm 22$  mJy are consistent with an outstanding point source at the location of MWC 297 inferring that free-free emission from the ZAMS-star maybe optically thick at submillimetre wavelengths.
2. Free-free emission from MWC 297 was found to contribute to approximately  $73 \pm 5$  per cent and  $82 \pm 4$  per cent of the  $450 \mu\text{m}$  and  $850 \mu\text{m}$  peak flux respectively. Residual dust peak fluxes are  $51 \pm 10$  mJy and  $15 \pm 3$  mJy flux per pixel at  $450 \mu\text{m}$  and  $850 \mu\text{m}$  respectively. Subtracting the free-free emission increases the spectral dust index by 35%. Dust at  $850 \mu\text{m}$  represents a  $1.4\sigma$  detection and at  $450 \mu\text{m}$  a  $0.6\sigma$  detection confirming that any residual disc around MWC 297 is too faint to be reliably detected.
3. A number of radio bright stars are observed in the W40 complex in the IR. OS1b, c, OS3a and IRS 5 are not detected in SCUBA-2, confirming that any free-free emission from these objects is optically thin at submillimetre wavelengths and no contamination subtraction is required.
4. The O9.5 MS-star OS1a and a cluster members VLA 12, 14 and 15 are non-variable compact radio sources with no evidence jet features observed. We classify these as UCH II regions with  $\alpha_{\text{ff}} = 0.6$  and calculate a free-free contribution of 62% at  $850 \mu\text{m}$  (no detection at  $450 \mu\text{m}$ ).
5. The Herbig AeBe star OS2a has a variable compact radio source consistent with episodic accretion. Radio shock fronts are also observed in the vicinity that would be consistent with jet emission. A significant SCUBA-2 peak of 1.83 and 0.558 Jy at  $450 \mu\text{m}$  and  $850 \mu\text{m}$  respectively is associated with this object. We classify this object as a collimated jet with

an  $\alpha_{\text{ff}} = 1.0$  and calculate a free-free contribution of 9% at 450  $\mu\text{m}$  and 12% at 850  $\mu\text{m}$ . Subtracting the free-free emission increases the spectral dust index by 2%. The residual dust has an unusually low spectral index  $1.6 \pm 0.1$  which is difficult to explain without invoking exceptional cold dust temperatures.

6. The B4 star OS2b has a variable compact radio source consistent with episodic accretion but lacks any signatures of jet emission. If a weak UCH II region is being detected it would be consistent with the B4 spectral class of the star which lies right on the threshold of sufficient Lyman photon production to power an H II region. We therefore judge that any free-free emission from this star would optically thin at SCUBA-2 wavelengths.
7. The large, diffuse H II region is observed in the W40 complex. This feature has an  $\alpha_{\text{ff}} = -0.1$  and has a peak flux of 0.03 Jy/pix in 21 cm VLA data which has a free-free contribution of 0.5% at 450  $\mu\text{m}$  and 5% at 850  $\mu\text{m}$ . Subtracting the free-free emission increases the spectral dust index by 3%.

Our results lead us to believe that where free-free emission is sufficiently bright and optically thick its contribution can lead to the observation of prominent point sources and significantly lower dust spectral indices, and therefore temperatures. Where the free-free emission is less prominent, in faint UCH II regions and from large-scale H II it can still have a limited, if non-negligible impact on the dust spectral index. In the following chapter we will look at what quantifiable affects the free-free emission has when examining the dust temperature.

# 5

## Temperature mapping

### 5.1 Introduction to the temperature equation

#### 5.1.1 Submillimetre Flux ratio

Using the ratio of 450  $\mu\text{m}$  and 850  $\mu\text{m}$  fluxes from SCUBA-2, we develop a method that utilises the two frequency observations of the same region where the ratio depends partly on the dust temperature ( $T_{\text{d}}$ ) via the Planck function and also on the dust opacity spectral index,  $\beta$  (a dimensionless term dependent on the grain model as proposed by Hildebrand 1983), as described by

$$\frac{S_{450}}{S_{850}} = \left(\frac{850}{450}\right)^{3+\beta} \left( \frac{\exp(hc/\lambda_{850}k_{\text{B}}T_{\text{d}}) - 1}{\exp(hc/\lambda_{450}k_{\text{B}}T_{\text{d}}) - 1} \right), \quad (5.1)$$

otherwise referred to as ‘the temperature equation’ (Reid & Wilson, 2005). There is no analytical solution for temperature and so pixel values are inferred from a lookup table. The method by which temperature maps are made can be split into two distinct parts: creating maps of flux ratio from input 450  $\mu\text{m}$  and 850  $\mu\text{m}$  data and building temperature maps based on the ratio maps. Both methods were discussed by Hatchell et al. (2013), for here on referred to as the H13 method. We focus on the development of this method and the additional features that have been incorporated.

#### 5.1.2 Beta

Temperature is known to influence the process by which dust grains coagulate and form icy mantles and therefore the value of  $\beta$ . Observations by Ubach et al. (2012) have shown

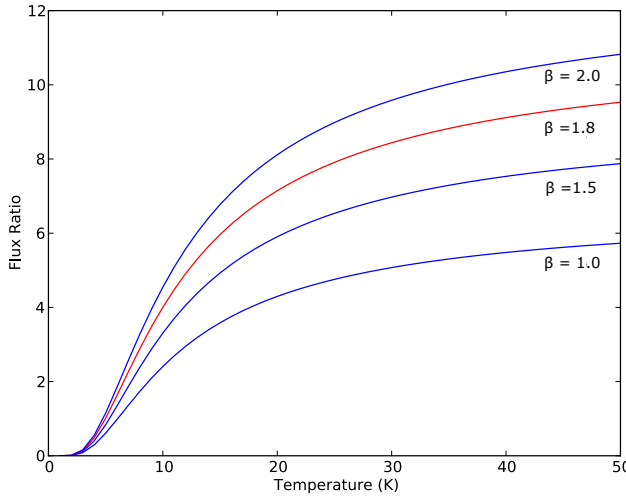


Figure 5.1: Flux ratio as a function of temperature as described by Equation 5.1. The temperature range is that commonly observed in protostellar cores.

decreases in  $\beta$  in protoplanetary disks but for the most part there is little evidence that  $\beta$  changes significantly in pre/protostellar cores (Schnee et al., 2014). Sadavoy et al. (2013) fitted *Herschel* 160  $\mu\text{m}$  to 500  $\mu\text{m}$  data with SCUBA-2 data in the Perseus B1 region and concluded that  $\beta$  is approximately 2.0 in extended, filamentary regions whereas it takes a lower value of approximately 1.6 towards dense protostellar cores. Figure 5.1 describes how small changes in  $\beta$  lead to a large range of flux ratios, especially at higher temperatures. For ratios of 3, 7 and 9, a  $\beta$  of 1.6 would return temperatures of 8.9, 25.4 and 85 K whereas a  $\beta$  of 2.0 would return temperatures of 7.6, 15.7 and 25 K. Higher ratios indicate heating above that available from the Interstellar Radiation Field (ISRF) for any reasonable value of  $\beta$ . Removing the requirement for the uncertainty in  $\beta$  requires data at additional wavelengths, for example 250  $\mu\text{m}$  and 350  $\mu\text{m}$  as observed by *Herschel*. Reconciling the angular scales of *Herschel* observations with those of SCUBA-2 is a non-trivial process and goes beyond the scope of this paper. Smaller values of  $\beta$  are found to be consistent with grain growth which only occurs sufficiently close to compact structures (Ossenkopf & Henning, 1994). Stutz et al. (2010) used the dominance of extended structure to that of compact structure to argue for a uniform, higher value of  $\beta$ . Likewise Hatchell et al. (2013) assumed a constant  $\beta$ , arguing that variation in temperature dominates to that of  $\beta$  in NGC1333. On this basis we adopt a uniform  $\beta$  of 1.8, a value consistent with the popular OH5 dust model proposed by Ossenkopf & Henning (1994) and studies of dense cores with *Planck*, *Herschel* and SCUBA-2 (Stutz et al., 2010; Juvela et al., 2011; Sadavoy et al., 2013). We note that in this regime an apparent fall in temperature towards the centre of a core might be symptomatic of low  $\beta$  values and therefore we cannot be as certain about the temperatures at these points.

### 5.1.3 Alpha

### 5.1.4 Temperature

## 5.2 Dual beam method

### 5.2.1 The JCMT beam (primary and secondary)

The JCMT beam can be modelled as two Gaussian components (Drabek et al., 2012; Dempsey et al., 2013). The primary (or main) beam contains the bulk of the signal and is well described by a Gaussian,  $G_{\text{MB}}$ , but in addition to this there is also a secondary beam which is much wider and lower in amplitude,  $G_{\text{SB}}$ . Together they make up the 2-component beam of the telescope,

$$G_{\text{total}} = aG_{\text{MB}} + bG_{\text{SB}}, \quad (5.2)$$

where  $a$  and  $b$  are relative amplitude, listed in Table ?? alongside the FWHM,  $\theta$ , of the primary (MB) and secondary (SB) beams.

### 5.2.2 Gaussian beam convolution

We introduce a secondary beam component into the H13 method, which previously assumed that the secondary component was negligible. This adds complexity to the convolution process as it requires convolution of the data with a normalised Gaussian of the form of the JCMT beam's primary and secondary components for the alternative wavelength. The primary component at  $850 \mu\text{m}$  is then scaled with

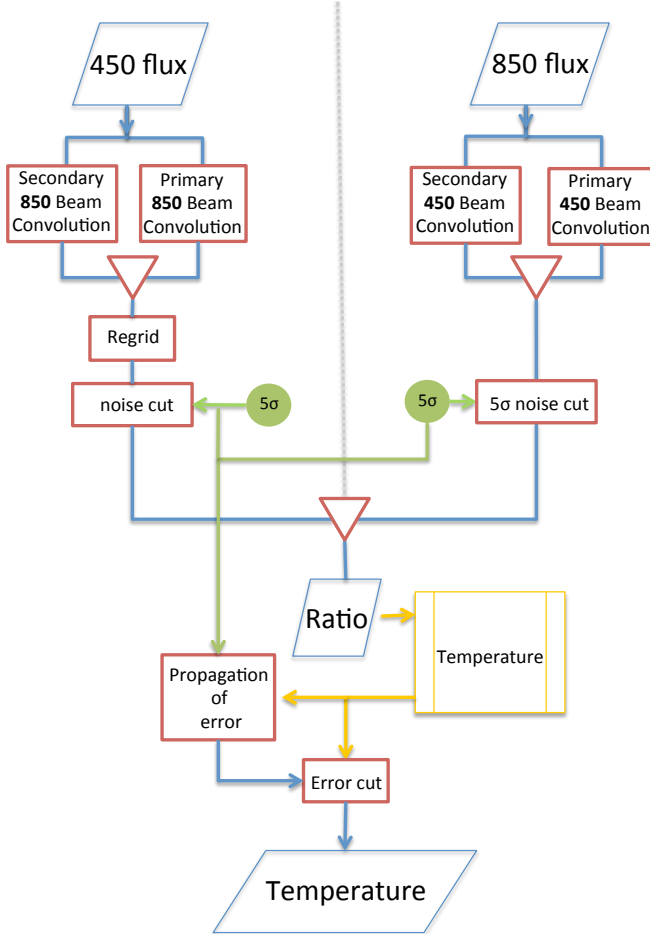
$$\frac{a_{450}\theta_{\text{MB}_{450}}^2}{a_{450}\theta_{\text{MB}_{450}}^2 + b_{450}\theta_{\text{SB}_{450}}^2}, \quad (5.3)$$

and likewise

$$\frac{b_{450}\theta_{\text{SB}_{450}}^2}{a_{450}\theta_{\text{MB}_{450}}^2 + b_{450}\theta_{\text{SB}_{450}}^2}, \quad (5.4)$$

for the secondary component. The  $450 \mu\text{m}$  map is convolved with the  $850 \mu\text{m}$  beam in a similar way. Corresponding parts are then summed together for  $450 \mu\text{m}$  and  $850 \mu\text{m}$  data separately to construct the convolved maps with an effective beam size of  $19.9''$  as shown in Figure 6.1.

### 5.2.3 4 component dual beam convolution method



Free parameters of our method are limited to  $\beta$  (which we set at 1.8). Input  $450 \mu\text{m}$  and  $850 \mu\text{m}$  flux density data (scaled in Jy/pixel) have fixed noise levels. Other fixed parameters which are used in the beam convolution include: the pixel area per map, FWHM of the primary ( $\theta_{\text{MB}}$ ) and secondary ( $\theta_{\text{SB}}$ ) beams and beam amplitudes all of which are measured by Dempsey et al. (2013) and given in Table ???. Input maps are first convolved with the JCMT beam (Equation 1) at the alternate wavelength to match resolution. Pixel size is taken into account in this process. The  $450 \mu\text{m}$  fluxes are then regridded onto the  $850 \mu\text{m}$  pixel grid. Data are then masked leaving only  $5\sigma$  detections or higher.  $450 \mu\text{m}$  fluxes are then divided by  $850 \mu\text{m}$  fluxes to create a map of flux ratio. Whereas the H13 method made a noise cut based on the variance array calculated during data reduction, our model introduces a cut based on a single noise estimate, following the method introduced by Salji (2014). The data are masked to remove pixels which carry astronomical signal. The remaining pixels are placed in a histogram of intensity and a Gaussian is fitted to the distribution, from which a standard deviation,  $\sigma$ , can be extracted as the noise level. This calculation is a robust form of measuring statistical noise that includes residual sky fluctuations. The inclusion of the secondary beam was found to decrease temperatures by between 5 per cent and 9 per cent with the coldest regions experiencing the largest drop in temperature and warmest the least. Applying a  $5\sigma$  cut based on the original  $450 \mu\text{m}$  data to mask uncertain regions of large

scale structure after the beam convolution can lead to spuriously high values around the edges of our maps where fluxes from pixels below the threshold are contributing to those above, producing false positives. These ‘edge effects’ are mitigated by clipping but we advise that where the highest temperature pixels meet the map edges these data be regarded with a degree of scepticism. Ratio maps are converted to temperature maps using Equation 5.1 implemented as a look-up table as there is no analytical solution. The H13 method subsequently cuts pixels with an arbitrary uncertainty in temperature of greater than 5.5 K. We replace this with a cut of pixels of an uncertainty in temperature (calculated from the noise level propagated through the method described in Section 3.1) of greater than 5 per cent.

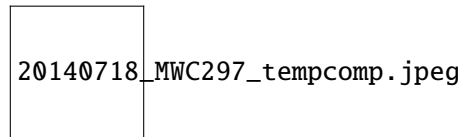


Figure 5.2: Temperature maps of MWC 297 from the ratio of  $450 \mu\text{m}$  and  $850 \mu\text{m}$  emission pre (*left*) and post (*right*) free-free contamination subtraction. Contours are at 11, 25 and 38 K. The location of MWC 297 is marked with a star.

## 5.3 Propagation of error

### 5.3.1 Analytical calculation

### 5.3.2 Monte-Carlo method

## 5.4 Testing Dual beam method

## 5.5 Kernel method

### 5.5.1 Convolution kernel

### 5.5.2 Beam model/beam map

### 5.5.3 Preparing the Kernel

## 5.6 Propagation of error

### 5.6.1 Monte-Carlo method

## 5.7 Testing Kernel method

### 5.7.1 Pixel size problem

## 5.8 Comparing ratio methods

## 5.9 Calculating temperature

### 5.9.1 Edge effects

### 5.9.2 Comparison with alternative methods

## 5.10 The impact of CO contamination

## 5.11 The impact of the free-free contribution

Figure 5.4 presents the  $850 \mu\text{m}$  before and after subtraction. Figure 5.3 presents the impact of free-free emission on temperature maps of the region. Even with the free-free emission subtracted, a

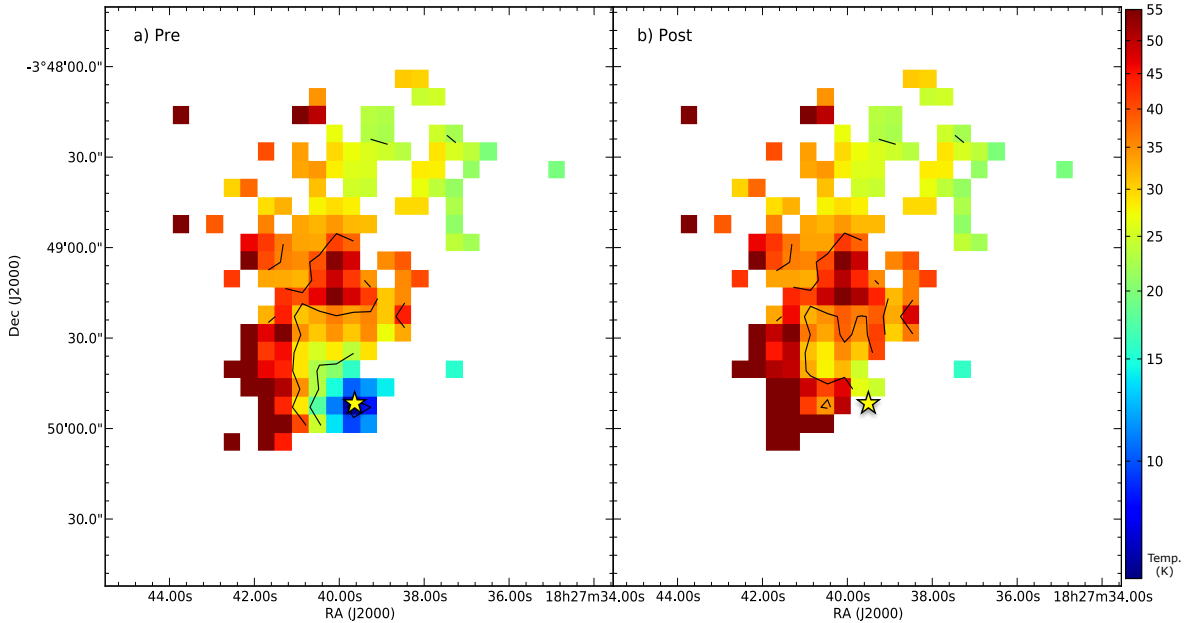


Figure 5.3: Temperature maps of MWC 297 from the ratio of  $450\text{ }\mu\text{m}$  and  $850\text{ }\mu\text{m}$  emission pre (left) and post (right) free-free contamination subtraction. Contours are at 11, 25 and 38 K. The location of MWC 297 is marked with a star.

large, extended submillimetre clump remains, though its peak is offset from the location of MWC 297 by  $24.2''$  (approximately 6,000 AU). The impact of this contamination on the temperature maps is remarkable. The power law of  $\alpha = 1.03 \pm 0.02$  that describes free-free emission from both an UCHII region and jet outflows produces greater flux at  $850\text{ }\mu\text{m}$  than  $450\text{ }\mu\text{m}$ . Free-free dominates the flux and this results in artificially lower ratios and therefore lower temperatures. This is consistent with the cold spot seen in Figure 5.3a at the location of the UCHII region, with a temperature of approximately 11 K. We can conclude that free-free emission may contaminate submillimetre temperature maps where cold spots are coincident with hot OB stars. The  $5\sigma$  level of 82 mJy and 11 mJy means that flux is too uncertain to be detected at  $450\text{ }\mu\text{m}$  and therefore it is not possible to calculate reliable temperatures of the residual circumstellar envelope/disk around the star.

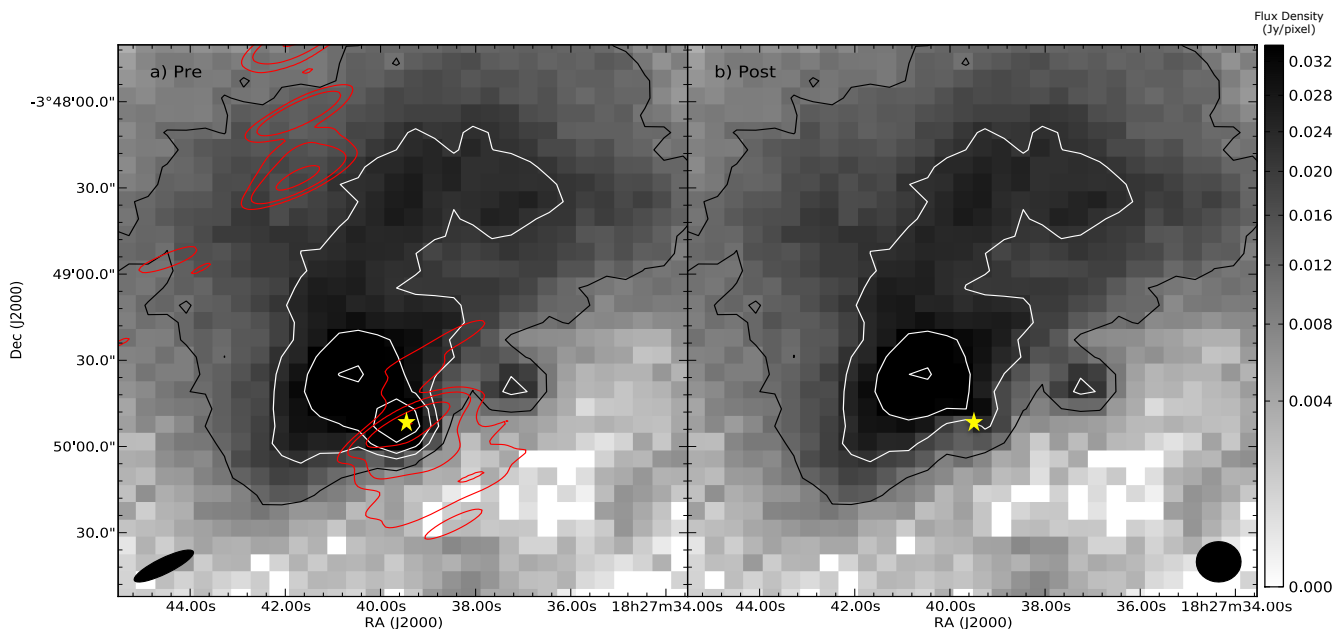


Figure 5.4: IR1 SCUBA-2 850  $\mu\text{m}$  data before *left* and after *right* removal of free-free contamination from an UCHII region and polar jets/winds (represented by the point source contours in the *left* plot). SCUBA-2 contours are at 0.011, 0.022, 0.033 and 0.055 Jy/pixel (corresponding to 5, 10, 15 and 25  $\sigma$  detection limits). 6 cm VLA contours (red) from Sandell (private comm.) at 0.002, 0.005, 0.02, 0.072, 0.083 Jy/beam are overlaid on the left hand panel. The location of MWC 297 is marked with a star. Beam sizes are shown at the bottom of the image (VLA CnD config. *left* and JCMT *right*.)

# 6

## Radiative heating in Serpens MWC 297 region

### 6.1 Temperature maps of Serpens MWC 297

The  $450\text{ }\mu\text{m}$  and  $850\text{ }\mu\text{m}$  SCUBA-2 data for the MWC 297 region are presented in Figure 6.1 alongside a map of temperature of submillimetre dust in that region. These maps show a large diversity in temperature across five isolated regions of significant flux (shown in Figure 6.1c). Mean cloud temperatures range from  $10.1\pm0.9\text{ K}$  and  $15\pm2\text{ K}$  for regions which are relatively cold and isotropic, to  $25\pm17\text{ K}$  for warmer regions with a large diversity of temperatures. Figure 5.3 shows one cloud that has a temperature of  $41\pm19\text{ K}$  which is hot to the extent that this would suggest an active heat source. The range in temperatures suggests that the regions within the Serpens MWC 297 vary in physical conditions.

Men'shchikov et al. (2010) infer temperature variation from contrasting strengths of  $350\text{ }\mu\text{m}$  flux bands to the shorter  $70\text{ }\mu\text{m}$  and  $160\text{ }\mu\text{m}$  bands of *Herschel*. They quote a temperature range for dense, starless filaments of 7.5 to 15 K across the whole Aquila rift. However, we do not observe a typical filamentary structure in Serpens MWC 297 region (Figure 2.3).

Könyves et al. (2010) and Bontemps et al. (2010) used single-temperature modified black-body fitting of SEDs of *Herschel*  $500\text{ }\mu\text{m}$  data points in Aquila and Polaris. Their study includes Serpens MWC 297 and they find temperatures for the region ranging between 24 and 26 K. Though *Herschel*  $500\text{ }\mu\text{m}$  data is at a lower resolution than our effective beam, the general temperatures of the region seem consistent with our findings.

Hatchell et al. (2013) use only the primary beam to study NGC1333, finding typical dust temperatures of ranging from 12 to 16 K. They also argue for a heated region pushing temperatures up as high as 35 to 40 K near the location of the B star SVS3. When the moderating effects of the secondary beam are taken into account, these results are largely consistent with our findings

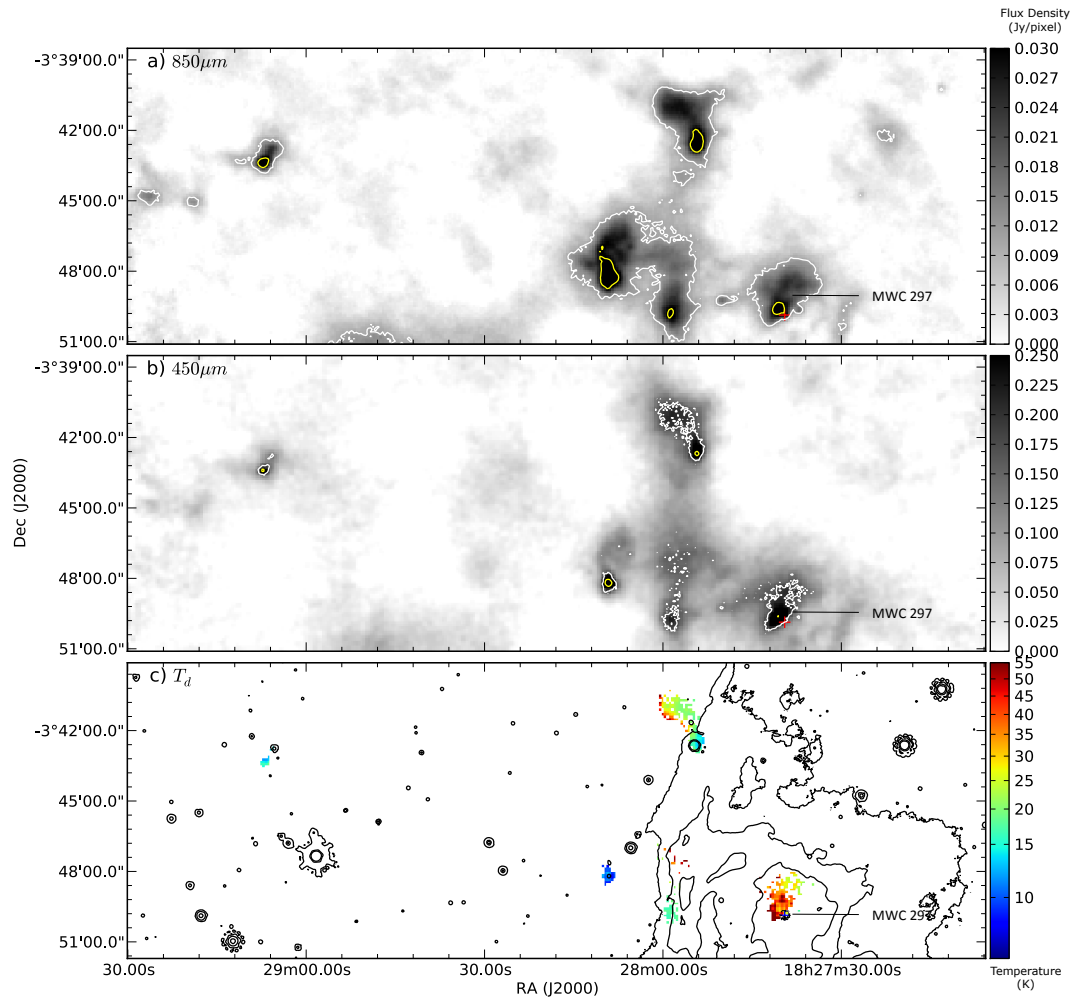


Figure 6.1: Top to bottom: a) SCUBA-2 convolved  $850 \mu\text{m}$  flux map of Serpens MWC 297. Contours from the original  $850 \mu\text{m}$  data are at  $0.011, 0.033 \text{ Jy/pixel}$  (corresponding to  $5$  and  $15 \sigma$ ). b) SCUBA-2 convolved and aligned  $450 \mu\text{m}$  flux map of Serpens MWC 297 in  $\text{Jy/pixel}$ . Contours from the original  $450 \mu\text{m}$  data are at  $0.082, 0.25 \text{ Jy/pixel}$  (corresponding to  $5$  and  $15 \sigma$ ). The crosses in a) and b) mark the location of the ZAMS B1.5Ve star MWC 297 and its binary partner OSCA (A2v). c) Dust temperature map of Serpens MWC 297 for  $\beta = 1.8$ . Contours of *Spitzer*  $24 \mu\text{m}$  emission at  $32, 40$  and  $70 \text{ MJy per Sr}$  are overlaid.

(Serpens MWC 297 also contains a B star).

Figure 6.1c shows *Spitzer* MIPS 24  $\mu\text{m}$  flux for the Serpens MWC 297 region. These data show hot compact sources associated with individual stellar cores. It also shows the morphology of an extended IR nebulosity, associated with SH2-62, that is centred on MWC 297. As well as the dust within the immediate vicinity of the star MWC 297 showing clear signs of heating, we observe 24  $\mu\text{m}$  emission that is coincident with heating in the SCUBA-2 temperature maps. As 24  $\mu\text{m}$  emission provides independent evidence of heating, where we observe high temperature pixels that are not coincident with 24  $\mu\text{m}$  emission (for example in the northernmost cloud) we conclude we are likely witnessing data reduction artefacts as opposed to warm gas and dust.

In addition to providing evidence for direct heating by MWC 297, the 24  $\mu\text{m}$  data also provide strong evidence that the B star is physically connected to the observed clouds. The Aquila rift is thought to be a distance of  $250 \pm 50$  pc (Maury et al., 2011) and through association we conclude that the distance to MWC 297 matches this figure.

## 6.2 The SCUBA-2 clump catalogue

In this section we introduce the clump-finding algorithm **FELLWALKER** used to identify clumps in the SCUBA-2 data presented in Figure 2.3. We calculate clump masses and compare these to their Jeans masses to determine whether or not the objects are unstable to gravitational collapse.

### 6.2.1 Fellwalker parameters

We tuned the **FELLWALKER** algorithm to produce a set of objects consistent with a by-eye decomposition, setting the following parameters;  $\text{MinDip} = 1\sigma$  (minimum flux between two peaks),  $\text{MinPix} = 4$  pixels (minimum number of pixels per valid clump),  $\text{MaxJump} = 1$  pixel (distance between clump peaks),  $\text{FWHMBeam} = 0$  (FWHM of instrument),  $\text{MinHeight} = 3\sigma$  (minimum height of clump peak to register as a valid clump) and  $\text{Noise} = 3\sigma$  (detection level). Throughout this process we used a constant noise level,  $\sigma$ , calculated via the method described by Salji (2014) and described in Section 3.1. Watson (2010) discusses the **FELLWALKER** parameters in depth and concludes  $\text{MinDip}$  and  $\text{MaxPix}$  are the most influential in returning the maximum breakup of clouds into clumps, a subset of which will later be used to compile a list of protostellar cores. The  $3\sigma$  level allows for the detection of the smallest clumps that may be missed at the  $5\sigma$  level on account of insufficient pixels for detection as outlined above. This method also included a number of spurious clumps associated with high variance pixels at the maps edges. In order to avoid these we first masked the SCUBA-2 data with the data reduction mask shown in Figure 2.3.

Using these parameters 28 submillimetre clumps were detected in 850  $\mu\text{m}$  data and are presented in Figure 7.2. Two sources (SMM 23 and 25) were immediately discarded as they were not consistent with a  $5\sigma$  detection. A further two clumps were split into two separate objects by the algorithm when there was no discernible peak in the submillimetre data. In these cases (SMM 7 & 8 and SMM 13 & 14) the objects were recombined into single object. We note that this is a side effect of having a low  $\text{MinDip}$  parameter to maximise the detection of smaller clumps. In total a sample of 23 clumps are presented in Table 3. We note that there is a known bias that

underestimates the size of a clump as its peak flux approaches the cutoff level and therefore biases against the detection of cold, faint objects (examples might be SMM 26 and 27). Modelling clump profiles could be used to better estimate the full extent of these objects. However, as these present a minority of cases we take no further action on this issue (Rosolowsky & Leroy, 2006).

The FELLWALKER algorithm is insensitive to low mass, isolated objects where detections were limited to less than five pixels above the noise level. We find that one potential source was missed on account of it only exhibiting a single significant pixel above the  $5\sigma$  noise level. Here object flux was measured with aperture photometry (see Section 5.2).

Due to the higher noise level of the  $450\text{ }\mu\text{m}$  data many objects detected at  $850\text{ }\mu\text{m}$  were not present at  $450\text{ }\mu\text{m}$ . Therefore we apply the  $850\text{ }\mu\text{m}$  clump boundaries to the  $450\text{ }\mu\text{m}$  data when calculating integrated intensity at that wavelength to ensure consistent flux extraction at both wavelengths for each object.

### 6.2.2 Mass

SCUBA-2 observations of the Serpens MWC 297 region were used to calculate the masses of the FELLWALKER clumps. Hildebrand (1983) describes how the mass of a cloud can be calculated from the submillimetre emission of dust grains fitted to a black-body spectrum for a nominal temperature. We follow this standard method for calculating clump mass (for example Johnstone et al. 2000, Kirk et al. 2006, Sadavoy et al. 2010 and Enoch et al. 2011). We use flux at  $850\text{ }\mu\text{m}$  ( $S_{850}$ ) per pixel, dust opacity ( $\kappa_{850}$ ), distance ( $d$ ) and a variable temperature ( $T_d$ ) per pixel, summing over all pixels,  $i$ , in the clump to calculate the total clump mass:

$$\begin{aligned} M = & 0.39 \sum_i S_{850,i} \left[ \exp\left(\frac{17\text{K}}{T_{d,i}}\right) - 1 \right] \\ & \times \left( \frac{d}{250\text{pc}} \right)^2 \left( \frac{\kappa_{850}}{0.012\text{cm}^2\text{g}^{-1}} \right)^{-1}. \end{aligned} \quad (6.1)$$

There is a high degree of uncertainty in the value of  $\kappa_{850}$ . The popular OH5 model of opacities in dense ISM, with a specific gas to dust ratio of 161, gives  $0.012\text{ cm}^2\text{g}^{-1}$  at  $850\text{ }\mu\text{m}$  (Ossenkopf & Henning, 1994). Comparable studies suggest values of 0.01 (Johnstone et al., 2000), 0.019 (Eiroa et al., 2008) and  $0.02\text{ cm}^2\text{g}^{-1}$  (Kirk et al., 2006). Henning & Sablotny (1995) find  $\kappa_{850}$  can vary by up to a factor of two. We assume an opacity of  $\kappa_{850} = 0.012$  following Hatchell et al. (2005). This value is consistent with  $\beta = 1.8$  over a wavelength range of  $30\text{ }\mu\text{m}$  to  $1.3\text{ mm}$ . We assume a distance  $d = 250 \pm 50\text{ pc}$  following Sandell et al. (2011) as outlined in Section 1.

We calculate dust masses using dust temperatures calculated for each pixel where possible. Not all the clumps shown in Figure 7.2 have temperature data due to the noise constraints of the temperature mapping process and the requirement that the region is also detected at  $450\text{ }\mu\text{m}$ . For those that do not, a constant clump temperature of  $15\text{ K}$  is assumed following Johnstone et al. (2000) and Kirk et al. (2006). Some clumps have only partial temperature data. In these cases the remaining pixels are filled with a value equal to the mean of the existing data. In some cases (SMM

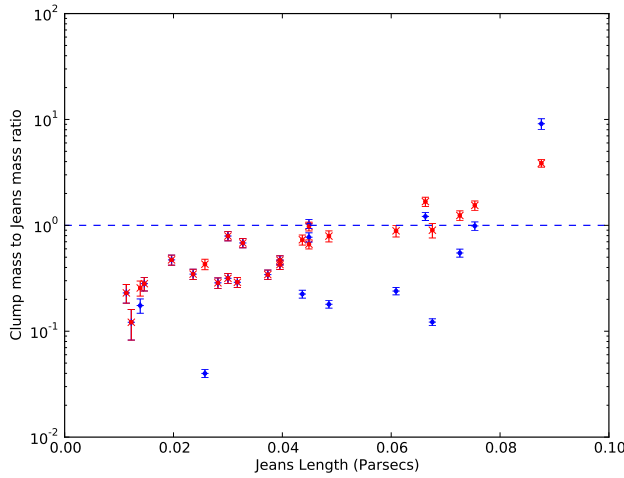


Figure 6.2: Jeans stability plotted against Jeans length. All clumps with  $M_{850}/M_J > 1$ , as shown by the dashed line, are expected to be undergoing collapse. Blue circles represent calculations made with real temperature data whereas red crosses indicate those made with an assumed temperature of 15 K. Systematic error in the measurement of distance to MWC 297 accounts for 20 per cent uncertainty on Jeans length.

6 and 11 for example), temperature data is limited to a few pixels whereas the total clump area is an order of magnitude larger. As it is unlikely that such a small sample of data will accurately represent the whole clump, results for objects such as these should be treated with a larger degree of uncertainty. Edge effects have a negligible influence on clump mass as high temperatures reduce the contribution in Equation 5. Clump masses are listed in Table 6.1.

The total mass of clumps in Serpens MWC 297 is  $40 \pm 3 M_\odot$ . Individual clump masses range over 2 orders of magnitude from  $0.05$  to  $19 M_\odot$  with 29 per cent of objects having a mass of  $1 M_\odot$  or higher. Figure 7.2 shows how FELLWALKER divides the areas of star formation into five large-scale star-forming clouds and a small number of isolated objects. Of these clouds, SMM 1, 12, 15 & 16 is the most massive at  $21 \pm 2 M_\odot$ , containing 53 per cent of all the mass detected by FELLWALKER, followed by SMM 2, 7 & 8 at  $6.6 \pm 0.3 M_\odot$  (17 per cent), SMM 4, 10, 11, 13, 14, 21 & 24 at  $3.3 \pm 0.1 M_\odot$  (9 per cent), SMM 3, 6 & 19 at  $3.1 \pm 0.1 M_\odot$  (8 per cent) and SMM 5, 22, 26 & 27 at  $3.1 \pm 0.3 M_\odot$  (8 per cent).

### 6.2.3 Jeans mass

The Jeans instability (Jeans, 1902) describes the balance between thermal support and gravitational collapse in an idealised cloud of gas.  $R_J$  defines a critical length scale above which the cloud may collapse on a free fall timescale and star formation can take place. Analogously,  $M_J$  defines an upper limit of mass. Assuming a spherical clump has a density such that it is Jeans unstable to perturbations at the size of the clump,  $R_J$ , then

$$M_J = 1.9 \left( \frac{\bar{T}_d}{10\text{K}} \right) \left( \frac{R_J}{0.07\text{pc}} \right) M_\odot. \quad (6.2)$$



We use the effective radius of the clump, as determined by clump area (in pixels) from `FELLWALKER` (Table 6.1), as the length scale  $R_J$ . We note that effective radius is a lower limit on clump size. Mean temperature,  $\bar{T}$ , across the clump is calculated directly from our temperature maps.

Whereas mass was calculated on a pixel-by-pixel basis, this is not possible for  $M_J$  as the characteristic length scale of the Jeans instability covers the entire object. Instead we use a mean temperature calculated from our maps. Temperatures and Jeans masses of clumps are also shown in Table 6.1. The masses of clumps calculated with the temperature data in the previous section deviates from the equivalent masses calculated with a uniform mean temperature (set at 15 K) of that clump by 12 per cent on average per clump which is sufficiently similar to allow this analysis.

This method is based on the work by Sadavoy et al. (2010) who performed a similar analysis for starless cores in the Gould belt. They used the assumption of a typical cold (10K) molecular cloud core size of 0.07 pc (Di Francesco et al., 2007). Rosolowsky et al. (2008) determined a range of temperatures of 9 K to 26 K in Perseus (a similar region to Serpens-Aquila) from ammonia observations. This paper goes a step further and is able to use mean temperatures specific to each clump. We determine a mean clump temperature of  $20 \pm 10$  K. The greater uncertainty on this value is indicative of the greater diversity of temperatures than assumed by Sadavoy et al. (2010).

Under the assumption that only internal pressure can balance self-gravity,  $M_J$  sets an upper limit on the mass of a sphere of gas for a given radius. If the observed mass,  $M_{850}$ , is greater than the calculated  $M_J$ , or alternatively  $M_{850}/M_J > 1$ , that would suggest that the clump is unstable to gravitational collapse and hence active star formation is likely (Mairs et al., 2014). An object that has  $M_{850}/M_J \ll 1$  is currently stable and will not collapse (alternatively it has already collapsed and the majority of the mass is now contained within the protostar). Given the uncertainties present in theory and observations, the stability of objects where  $M_{850}/M_J \approx 1$  is ambiguous. Figure 6.2 plots  $M_{850}/M_J$  against the Jeans length scale for the clumps identified in Serpens MWC 297 and reveals that at least three out of a total 22 clumps detected by `FELLWALKER` are Jeans unstable and may contain protostars. Evidence for these are addressed in Section 5. For comparison,  $M_{850}/M_J$  is plotted for the same list of objects, assuming a single clump temperature of 15 K (the red crosses in Figure 6.2). We observe that in a majority of cases using a real temperature has caused the ratio to decrease and we therefore conclude that previous authors who have used a constant temperature of 15 K have underestimated the stability of their clumps.

### 6.3 The SCUBA-2 YSO catalogue

In this section we cross-reference our list of SCUBA-2 clumps, as identified by `FELLWALKER`, with *Spitzer* YSOc catalogues and produce our own SCUBA-2 confirmed YSOc catalogue for the Serpens MWC 297 region.

We calculate the relative distribution of protostars to PMS stars in the region as a measure of dynamical evolution of YSOcs within a star-forming cluster. We produce Spectral Energy Distributions (SEDs) of the YSOcs where supplementary data exist. With the addition of new SCUBA-2 data at 450  $\mu\text{m}$  and 850  $\mu\text{m}$  we update the classification of the YSOcs in the Serpens

Table 6.2: Ratios of protostars (Class 0, I, FS) to PMS stars (Class II, TD, III) in the SGBS and SCUBA-2 catalogue

	Protostars	PMS-stars	Ratio
Control region	0	49	0.0
<i>Herschel</i> 2Jy beam <sup>-1</sup> mask	10	23	0.43
SCUBA-2 3 $\sigma$ mask	8	10	0.80

MWC 297 region.

### 6.3.1 YSO distribution

Kaas et al. (2004), Winston et al. (2007) and Harvey et al. (2007) discuss how evolutionary class (determined by IR spectral index) and spatial distribution in a star-forming region are correlated, finding that Class 0/I and FS sources are concentrated towards the central filaments of Serpens Main region whereas Class II, TD and III sources are much more widely distributed. We incorporate SCUBA-2 data into this method, allowing for direct comparison of evolutionary class spatial distribution with H<sub>2</sub> column density. Our method takes the ratio of the number of protostars to PMS stars. Ratios are calculated for the region within the data reduction mask (a large scale region defined as where *Herschel* 500  $\mu$ m emission is greater than 2 Jy/beam; see Figure 2.3), and the emission ‘cloud’ defined as above the 3 $\sigma$  detection in SCUBA-2 850  $\mu$ m, consistent with the levels set for FELLWALKER clump analysis in Section 4.1. In addition the ratio was calculated for the space outside of the data reduction mask up to the boundaries of the SCUBA-2 data in Figure 2.4 as a control region. Table 6.2 shows the results for these corresponding areas for the YSOcs catalogues listed in Table 2.3 and plotted in Figure 2.4.

Preliminary work by Kaas et al. (2004) suggested that Class I to Class II ratios were 10 times greater within cloud regions of Serpens Main than outside them. Harvey et al. (2007) conducted a similar analysis and found ratios of 0.37 for the whole region and 1.4 and 3.0 for the cloud regions. Whereas our ratios are not as large (0.8), they do follow the same trend of greater numbers of protostars in regions of higher column density, supporting the conclusion that protostars form in regions of high column density and then migrate away from these regions as they evolve into PMS-stars.

### 6.3.2 SCUBA-2 YSOcs

In this section we determine which members of the SCUBA-2 clump catalogue (Table 6.1) are starless and which host YSOs, as FELLWALKER is parameterised to identify both. The FELLWALKER algorithm is ideal for identifying larger scale, often irregular and extended clumps, but not effective for extracting the flux of individual YSOs, which are smaller. We extract a revised catalogue of YSOcs (Table 6.3) based on the position of the clumps listed in Table 6.1 and calculate the flux emission using aperture photometry with a fixed 40'' diameter aperture.

Six clumps are found to contain SGBS YSOcs (Table 2.2) by cross-referencing the SCUBA-

2 clumps in Table 6.1 (Figure 6.4) with IR sources (Table 2.2). Two further clumps (SMM 1 and 3) are found with little or no IR emission but are centrally condensed and have  $M_{850}/M_J > 1$  signifying they are gravitationally unstable and may be early protostellar (Class 0) YSOcs.

The following YSOcs-hosting clumps detected (SMM 1, 2, 3, 6, 10, 11, 16 and 18) are listed in Table 6.3 as SCUBA-2 YSO candidates (S2-YSOc). The remaining clumps listed in Table 6.1 do not contain YSOcs and are considered starless. SMM 4 and 7 are notable as they have relatively high masses (greater than  $1 M_\odot$ ) but are not forming stars. SMM 5 has  $M_{850}/M_J = 1$  but there is no evidence for a  $24 \mu\text{m}$  source there. It could be argued that this is a prestellar object on the cusp of becoming protostellar.

In addition to all those submillimetre objects identified by FELLWALKER, we also include one additional YSOc, S2-YSOc 29, as listed in Table 6.3 and YSOc11 in Table 2.2. This object fulfils the criterion of coincidence with a strong IR source in the *Spitzer*  $24 \mu\text{m}$  MIPS data and a corresponding Class III identification in the SGBS YSOcs catalogue. S2-YSOc 29 registers a  $5\sigma$  detection with one pixel and resembles S2-YSOc 10 and 18 which are also believed to be an isolated, Class III PMS-stars with the remnants of an envelope/cold accretion disc contributing to their observed submillimetre flux.

Apertures were placed over the peak positions of the FELLWALKER clumps (Table 6.1) in addition to the *Spitzer* YSOcs positions and the integrated SCUBA-2 flux calculated with the intention to measure the flux from any dense, protostellar core associated with the SCUBA-2 clump peak and/or Spitzer YSOc. We follow Di Francesco et al. (2007), Sadavoy et al. (2010) and Rygl et al. (2013)'s definition of a core as a gravitationally bound, dense object, of diameter less than 0.05 pc and set apertures at this size ( $40''$  at 250 pc). Some larger scale emission is likely to be observed. However, through careful selection of aperture size we can assume that emission from the core dominates at this length scale.

Figures 2.4 and 6.3 show the locations of the SCUBA-2 YSOcs as well as those catalogued in the SGBS catalog. Figure 6.4 shows the relationship between the submillimetre peaks and the *Spitzer* YSOc position, with the SCUBA-2 fluxes for *Spitzer* YSOcs presented in Table 6.4. The mass of the SCUBA-2 YSOcs are calculated with Equation 7.1, using a constant, mean temperature derived from our maps, and the results presented in Table 6.3.

A small number of *Spitzer* YSOcs inside the *Herschel*  $500 \mu\text{m}$  data reduction mask are consistent with SCUBA-2 YSOcs with identical peak positions, for example in S2-YSOc 18 (Figure 6.4). In some cases, positions appear offset, for example S2-YSOc 2. This anomaly can be explained by virtue of the deeply embedded nature of the source and that *Spitzer* might be observing IR emission from an outflow cavity rather than the YSO itself.

YSOcs classified as 0/I by *Spitzer* should also have evidence of a SCUBA-2 peak at the same position. Those *Spitzer* detected protostars (YSOc16 and 38; Table 2.2) that lie outside of the  $5\sigma$  detection limit at  $850 \mu\text{m}$  and have no obvious peak in emission are unlikely to be YSOcs and discarded as incorrectly classified objects.

A minority of cases detect greater than  $5\sigma$  flux but have no significant peak in emission, for example YSOc15 and 21. Examining these specific cases, both are classified as protostars and are deeply embedded within S2-YSOc13. Figure 6.1c shows how this region is near the centre of the

Figure 6.3: Comparison of flux emission from **FELLWALKER** objects at  $450\text{ }\mu\text{m}$  (contours),  $850\text{ }\mu\text{m}$  (greyscale) and the SGBS YSOcs (markers). Numbers in square brackets correspond to the objects in Table 6.1. Maps show contours of  $450\text{ }\mu\text{m}$  submillimetre flux at 5, 10, 20 and  $30\sigma$  ( $\sigma = 0.016\text{ Jy/pixel}$ ). *Spitzer* YSOcs are indicated by hollow black circles (Class III), solid red circles (Class II) and green hollow circles (Class 0/I). The star indicates the location of the star MWC 297.

Figure 6.4: Submillimetre clumps in Serpens MWC 297 as identified by the **FELLWALKER** clump-finding algorithm. Numbers in square brackets correspond to the objects in Table 6.1. Maps show contours of  $850\text{ }\mu\text{m}$  submillimetre flux at 5, 10, 20 and  $30\sigma$  ( $\sigma = 0.0022\text{ Jy/pixel}$ ) up to the position of peak flux (black cross). The aperture from which SED flux density was calculated is plotted as the scale size of a protostellar core (0.05 pc). Temperature is shown where it is statistically significant and is used to calculate the masses shown in Table 6.3. *Spitzer* YSOcs are indicated by hollow black circles (Class III), solid red circles (Class II) and green hollow circles (Class 0/I). The star indicates the location of the star MWC 297.

reflection nebulae SH2-62 and therefore we interpret YSOc15 and 21 as IR emission from dust heated by the star MWC 297 and not real YSOcs. Many of the remaining *Spitzer* YSOcs detect low level, extended SCUBA-2 flux with no significant peak. No significant flux is detected for objects outside the mask.

### 6.3.3 Spectral energy distributions

SEDs are powerful tools for determining the properties of a star and we use these as an aid to classification through measurement of the spectral index across their IR wavebands, bolometric temperature and luminosity ratio (Evans et al., 2009).

SEDs are constructed from archival Two Micron All Sky Survey (2MASS) fluxes, *Spitzer* fluxes, and from SCUBA-2 fluxes. For the SCUBA-2 fluxes we conducted aperture photometry (as described in Section 5.2) at both  $450\text{ }\mu\text{m}$  and  $850\text{ }\mu\text{m}$  centred on the **FELLWALKER** clump peaks from Table 6.1. None of our sources overlapped sufficiently to make blended emission a problem.

Our primary sources are IRAC and MIPS data from the SGBS. Six out of nine objects are identified in the SGBS YSOc catalogue. We access the full SGBS source catalogue, which includes sources not classified as YSOcs, and find fluxes of each of the remaining three objects. S2-YSOc 1 and 3 are low luminosity objects that cannot be reliably classified as a YSOc by *Spitzer* and are therefore labelled ‘Red’ and ‘Flat’ following a description of their SEDs. Both objects have IRAC and MIPS fluxes that are many orders of magnitude less than their peers. S2-YSOc 16 has been classed as a F5V star. Following the work of Alonso-Albi et al. (2009) we bring together fluxes and present the SEDs in Figure 6.5 with specific cases of individual YSOs discussed in depth the following sections.

Many of the following methods directly use the SEDs constructed in this section to classify YSOs by examining how the flux of the object varies with wavelength.

Table 6.3: Properties of YSO candidates in MWC 297.

ID <sup>a</sup>	$S_{450}^b$ (Jy)	$S_{850}^b$ (Jy)	$M_{850}^c$ (M $_\odot$ )	$T_d^d$ (K)	$T_{bol}^e$ (K)	$\alpha_{IR}^f$	$L_{bol}^e$ (L $_\odot$ )	$L_{smm}/L_{bol}^e$ per cent	SGBS cla
S2-YSOc1	14.4	3.09	5.1(0.5)	10.3(0.5)	30(3)	1.65( 0.08)	1.1(0.1)	5.0(0.5)	'Red'
S2-YSOc2	11.1	1.56	1.3(0.1)	15.6(0.8)	290(30)	0.56(0.05)	2.1(0.2)	1.9(0.2)	'YSOc re
S2-YSOc3	7.0	1.09	0.95(0.08)	14.8(0.7)	8(1)	1.4(0.7)	0.8(0.1)	3.0(0.3)	'Flat'
S2-YSOc6	4.1	0.68	0.62(0.06)	14.2(0.7)	100(10)	0.30(0.05)	0.28(0.03)	5.2(0.5)	'YSOc'
S2-YSOc10	4.5	0.37	0.31(0.03)	15.0(-)	190(20)	0.17(0.05)	0.82(0.08)	1.8(0.2)	'YSOc star+
S2-YSOc11	3.9	0.35	0.22(0.02)	17.6(0.9)	780(60)	-0.43(0.06)	3.3(0.2)	0.3(0.0)	'YSOc'
S2-YSOc16	3.7	0.73	0.60(0.05)	15.0(-)	120(10)	0.9(0.3)	0.73(0.07)	1.9(0.2)	'star F5V
S2-YSOc18	0.1	0.11	0.09(0.02)	15.0(-)	820(50)	-0.17(0.05)	1.32(0.08)	0.1(0.0)	'YSOc star+'
S2-YSOc29	4.0	0.36	0.30(0.03)	15.0(-)	860(50)	-0.49(0.05)	0.34(0.02)	0.1(0.0)	'YSOc star+'
MWC 297	-	1.05	-	-	660(6)	-	422(4)	0.1(0.0)	'2mass'

- a) SCUBA-2 YSOcs (S2-YSOc) as identified by cross-referencing the SCUBA-2 clumps in Table 6.1 (Figure 6.4) with IR sources (Table 2.2).
- b) Integrated fluxes of the YSOcs determined by fixed 40'' diameter aperture photometry. The uncertainty at 450  $\mu$ m is 0.0165 Jy/pixel and at 850  $\mu$ m is 0.0022 Jy/pixel. There is an additional systematic error in calibration of 10.6 per cent and 3.4 per cent at 450  $\mu$ m and 850  $\mu$ m.
- c) Mass as calculated with equation 7.1. Errors in brackets are calculated from error in total flux, described in b., and error in mean temperature of 5 per cent. These results do not include the systematic error in distance (20 per cent) and opacity (factor of two).
- d) Mean temperature as calculated from the temperature maps (Figure 6.1). Where no temperature data is available an arbitrary value of 15K(-) is assigned that is consistent with the literature.
- e) YSOcs are classified using the  $T_{bol}$ ,  $L_{bol}$  and  $L_{smm}/L_{bol}$  methods which are described in Section 5.4.
- f) Values for spectral index are taken from the SGBS catalogue.
- g) SGBS notation is described in Evans et al. (2009).

Table 6.4: SCUBA-2 40'' aperture fluxes for the *Spitzer* YSOc listed in Table 2.2. A full version of this catalogue is available online.

ID	$S_{450}$ Jy	$S_{850}$ Jy	S2-YSOc ID
YSOc1	< 0.72 <sup>b</sup>	< 0.065 <sup>b</sup>	-
YSOc2	< 0.72	0.115 ± 0.013	S2-YSOc18
YSOc3	< 0.72 <sup>b</sup>	< 0.065 <sup>b</sup>	-
YSOc4	< 0.72 <sup>b</sup>	< 0.065 <sup>b</sup>	-
YSOc5	< 0.72 <sup>b</sup>	< 0.065 <sup>b</sup>	-
YSOc6	< 0.72 <sup>b</sup>	< 0.065 <sup>b</sup>	-
YSOc7	< 0.72 <sup>b</sup>	< 0.065 <sup>b</sup>	-
YSOc8	< 0.72 <sup>b</sup>	< 0.065 <sup>b</sup>	-
YSOc9	< 0.72 <sup>b</sup>	< 0.065 <sup>b</sup>	-
YSOc10	< 0.72 <sup>b</sup>	< 0.065 <sup>b</sup>	-
YSOc11	< 0.72	0.154 ± 0.013	S2-YSOc29
YSOc12	< 0.72 <sup>b</sup>	< 0.065 <sup>b</sup>	-
YSOc13	1.73 ± 0.14 <sup>a</sup>	0.184 ± 0.013 <sup>a</sup>	-
YSOc14	< 0.72 <sup>b</sup>	< 0.065 <sup>b</sup>	-
YSOc15	3.30 ± 0.14 <sup>a</sup>	0.408 ± 0.013 <sup>a</sup>	-
YSOc16	2.08 ± 0.14 <sup>a</sup>	0.071 ± 0.013 <sup>a</sup>	-
YSOc17	3.11 ± 0.14	0.362 ± 0.013	S2-YSOc11
YSOc18	2.10 ± 0.14 <sup>a</sup>	0.263 ± 0.013 <sup>a</sup>	-
YSOc19	< 0.72 <sup>b</sup>	< 0.065 <sup>b</sup>	-
YSOc20	1.11 ± 0.14 <sup>a</sup>	0.112 ± 0.013 <sup>a</sup>	-
...	...	...	...

(a) Extended low level emission in aperture. No significant peak at YSOc position ( $> 3\sigma$ ).

(b) Outside data reduction mask. No significant flux detected in initial data reduction stage ( $< 5\sigma$ ).

### 6.3.4 YSO classification

Spectral index,  $\alpha_{\text{IR}}$ , is a direct measurement of the gradient of the SED slope over a range of IR wavelengths (typically 2 to 24  $\mu\text{m}$ ) and is expressed as

$$\alpha_{\text{IR}} = \frac{d \log(\lambda S_\lambda)}{d \log(\lambda)}. \quad (6.3)$$

Gutermuth et al. (2008) calculated  $\alpha_{\text{IR}}$  from the fluxes in the SGBS catalogue and we display these results in Table 6.3 and Table 2.2 for SGBS. As a classification tool for YSOs,  $\alpha_{\text{IR}}$  was developed by Lada & Wilking (1984) and Greene et al. (1994) and is summarised by Evans et al. (2009) who specify the boundaries between

- Class 0/I :  $0.3 \leq \alpha_{\text{IRAC}}$
- Class Flat Spectrum :  $-0.3 \leq \alpha_{\text{IRAC}} \leq 0.3$
- Class II :  $-1.6 \leq \alpha_{\text{IRAC}} \leq -0.3$
- Class III :  $\alpha_{\text{IRAC}} \leq -1.6$

$\alpha_{\text{IR}}$  is one the most commonly used methods for the classification of protostars and consequently is one of the most criticised. Uncertainties on  $\alpha_{\text{IR}}$  typically vary between 10 and 20 per cent. However, measurements have been shown to be highly susceptible to disk geometry and source inclination (Robitaille et al., 2007) whilst extinction is known to cause  $\alpha_{\text{IR}}$  to appear larger. Furthermore, the development of  $\alpha_{\text{IR}}$  predates the identification of the Class 0 protostar (Chandler et al., 1990; Eiroa et al., 1994; André & Motte, 2000) and therefore does not distinguish between Class 0 and Class I when  $\alpha_{\text{IR}}$  is measurable (absence of  $\alpha_{\text{IR}}$  has been taken in this work to define a Class 0). Via the classification scheme outlined above, our sample contains four Class 0/I, two FS and three Class II sources. Saturation of *Spitzer* bands prevent measurement of  $\alpha_{\text{IR}}$  for MWC 297.

We calculate bolometric temperature,  $T_{\text{bol}}$ , and luminosity,  $L_{\text{bol}}$ , as alternative methods of classification of YSOs. We follow the numerical integration method of Myers & Ladd (1993) and Enoch et al. (2009) who calculated the discrete integral of the SED of an object for a given number of recorded fluxes. By adding SCUBA-2 data to that from the SGBS source catalogue, we extend the SEDs (Figure 6.5) for our YSOs into the submillimetre spectrum and allow for a more complete integral from which we calculate  $T_{\text{bol}}$ , the temperature of a black body with the same mean frequency of the observed SED, via

$$T_{\text{bol}} = 1.25 \times 10^{-11} \bar{\nu} (\text{K Hz}^{-1}), \quad (6.4)$$

where  $\bar{\nu}$  is the mean frequency of the whole spectrum,

$$\bar{\nu} = \frac{\int \nu S_\nu d\nu}{\int \nu d\nu}. \quad (6.5)$$

Classification separating boundaries for  $T_{\text{bol}}$  from (Chen et al., 1995).

- Class 0 :  $T_{\text{bol}} < 70K$

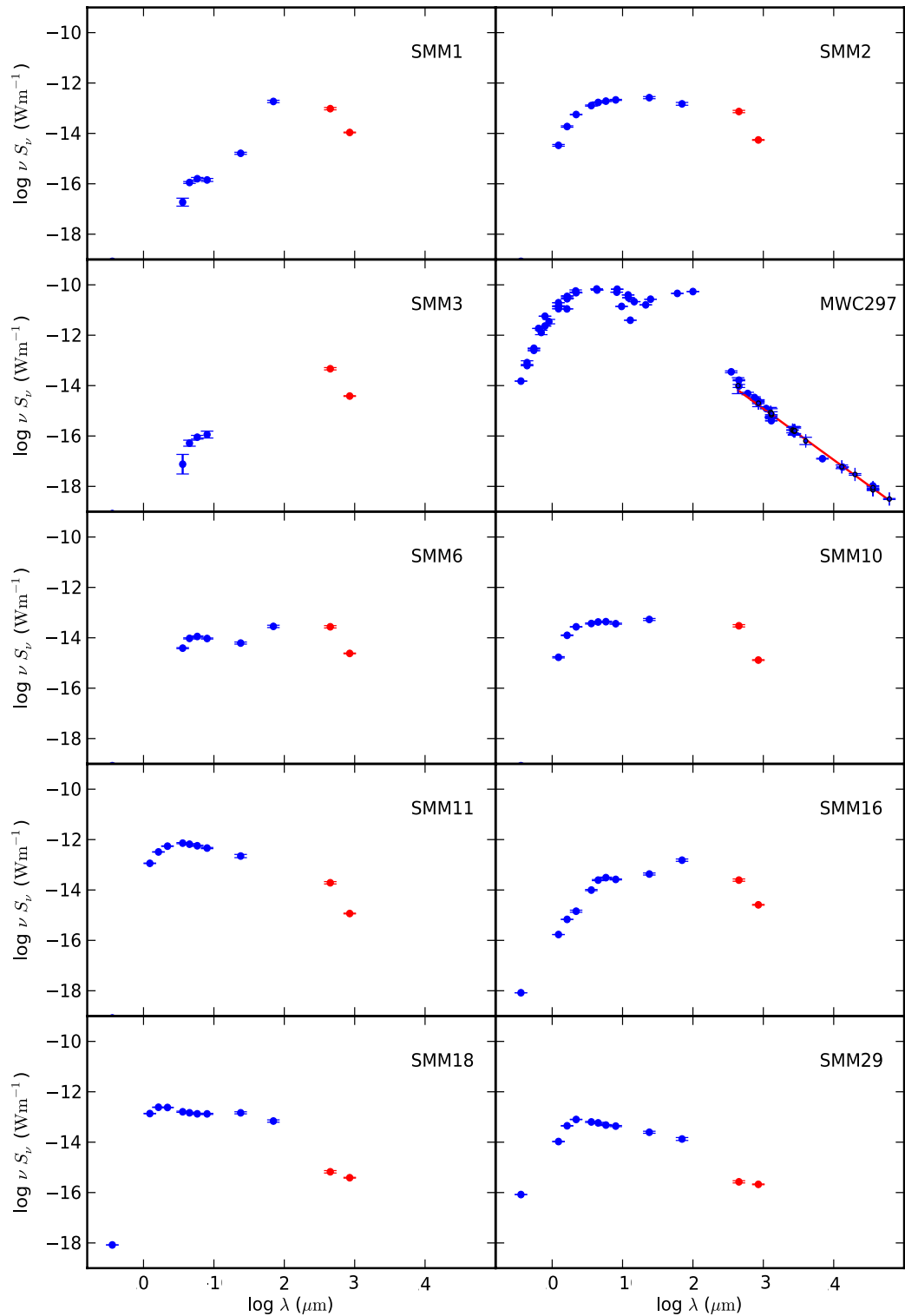


Figure 6.5: Spectral Energy Distributions for YSOs associated with FELLWALKER clumps (Table 6.3). Blue points represent archive data sourced from *Spitzer* and 2MASS. Red points show new data provided by SCUBA-2 at 450  $\mu\text{m}$  and 850  $\mu\text{m}$  (note that the star MWC 297 was not identified by FELLWALKER after free-free contamination was accounted for). The straight line in MWC 297 describes free-free emission from an UCHII region and polar jet/wind with a spectral index  $\alpha=1.03$ .

- Class I :  $70K \leq T_{\text{bol}} \leq 350K$
- Class II :  $350K \leq T_{\text{bol}} \leq 650K$
- Class III :  $650K \leq T_{\text{bol}} \leq 2800K$

$T_{\text{bol}}$  measurements for our sources are listed in Table 6.3. As this method uses more available data it could be considered a more reliable method of classification than  $\alpha_{\text{IR}}$  which only covers IRAC and MIPS bands 2  $\mu\text{m}$  to 24  $\mu\text{m}$ . Furthermore  $T_{\text{bol}}$  provides a quantifiable method for separating Class I and Class 0. Similarly we calculate the ratio of submillimetre luminosity ( $L_{\text{smm}}$ ), defined as  $\geq 350 \mu\text{m}$  by Bontemps et al. (1996), to  $L_{\text{bol}}$  in the method described by Myers et al. (1998) and Rygl et al. (2013), to classify YSOs:

$$L_{\text{bol}} = 4\pi d^2 \int_0^{\infty} S_{\nu} d\nu, \quad (6.6)$$

and likewise for the submillimetre luminosity,

$$L_{\text{smm}} = 4\pi d^2 \int_0^{350 \mu\text{m}} S_{\nu} d\nu. \quad (6.7)$$

This method was developed by André et al. (1993) who originally set the Class 0/I boundary at 0.5 per cent (subsequently used by Visser et al. (2002) and Young et al. (2003)). Maury et al. (2011) and Rygl et al. (2013) revise this upwards to 3 per cent and most recently Sadavoy et al. (2014) has used 1 per cent outlining the lack of consensus on this issue. We follow the work of Rygl et al. (2013) and classify objects with  $L_{\text{smm}}/L_{\text{bol}} \geq 3$  per cent as Class 0 protostars. Likewise, results for  $L_{\text{smm}}/L_{\text{bol}}$  are listed in Table 6.3.

Our sample contains two Class 0 sources, four Class I and three Class II by  $T_{\text{bol}}$  and three Class 0 to six Class I, II & III sources by  $L_{\text{smm}}/L_{\text{bol}}$ .

Uncertainties on  $L_{\text{bol}}$ ,  $L_{\text{smm}}/L_{\text{bol}}$  and  $T_{\text{bol}}$  were calculated using a Monte Carlo method. A normal distribution of fluxes, with the mean on the measured flux at each wavelength for each YSO with a standard deviation equal to the original error on the measurements was produced. From each set of fluxes our classifications were calculated and the standard deviation on results listed in Table 6.3. The size of the uncertainties are consistent with Dunham et al. (2008). Dunham et al. (2008) and Enoch et al. (2009) both study the error on  $L_{\text{bol}}$  and  $T_{\text{bol}}$  and conclude incompleteness of the spectrum is a major source of systematic error in results of order approximately 31 per cent and 21 per cent (respectively) when compared to a complete spectrum. Enoch et al. (2009) find that the omission of the 70  $\mu\text{m}$  flux is particularly critical when interpreting classification, leading to an overestimate of  $L_{\text{bol}}$  by 28 per cent and underestimate of  $T_{\text{bol}}$  by 18 per cent.

Figure 6.6 shows a direct comparison between the  $\alpha_{\text{IR}}$ ,  $L_{\text{smm}}/L_{\text{bol}}$  and  $T_{\text{bol}}$  methods of classifying YSOs. As outlined above, each specialises in classification at different stages of evolution with  $T_{\text{bol}}$  arguably being the most effective for classifying protostars. Young et al. (2005) studied the merits of  $T_{\text{bol}}$  and  $L_{\text{smm}}/L_{\text{bol}}$  and concluded that the latter is the more robust method for classifying Class 0 objects when compared to models of core collapse. However, it is also more sensitive to incompleteness of the submillimetre spectrum. With only two fluxes at wavelengths greater than 350  $\mu\text{m}$  for the majority of the YSOs in MWC 297, we must consider the results from

$L_{\text{smm}}/L_{\text{bol}}$  to be incomplete and therefore less reliable than  $T_{\text{bol}}$ .

Out of the three objects classified as Class 0 by both  $L_{\text{smm}}/L_{\text{bol}}$  and  $T_{\text{bol}}$  methods, only S2-YSOc 1 is consistent in both regimes. This object has a significantly positive value of  $\alpha_{\text{IR}}$  and so we classify this object as Class 0. The other two objects, S2-YSOc 3 and S2-YSOc 6, are forming in close proximity to each other but relatively isolated from the rest of the cloud. With a minimum separation of approximately 10,000 AU it seems likely that these objects formed together and therefore they are likely to be a similar class. S2-YSOc 3 has no noticeable IR flux at 24  $\mu\text{m}$ . However, the S2-YSOc 3 SED (Figure 6.5) shows *Spitzer* data consistent with emission from a heated region and so we conclude that the emission at 24  $\mu\text{m}$  is sufficiently weak that it does not surpass the noise level and therefore does not appear in Figure 6.1c. Such low luminosity emission would be typical of Class 0 and therefore we label it as such. S2-YSOc 6 has a weak, if non-negligible, detection at 24  $\mu\text{m}$  data. Therefore, we label it as Class 0/I. S2-YSOc 2 and 10 consistently fall into the Class I bracket by all three methods.

S2-YSOc 11, 18 and 29 all represent highly evolved and largely isolated cores that are consistently classified as Class II/III objects and have 24  $\mu\text{m}$  detections in Figure 6.1c. Finally we discuss S2-YSOc 16, an object labelled Class I by  $T_{\text{bol}}$  and by  $\alpha_{\text{IR}}$  and with a strong peak in the 24  $\mu\text{m}$  data. Figure 6.4 shows how this object appears deep within an extended dust cloud. This scenario fits the definition of a Class I and the low mass of the object ( $0.60 M_{\odot}$ ) when compared to the mass available in the neighbouring clumps (approximately  $21 M_{\odot}$ ) suggests that this object is early in its accretion life cycle.

## 6.4 Discussion

In this paper we use SCUBA-2 450  $\mu\text{m}$  and 850  $\mu\text{m}$  data and *Spitzer* data to investigate star formation in Serpens MWC 297 region. Taking the ratio of SCUBA-2 fluxes, we produce temperature maps of subregions of Serpens MWC 297 and calculate the properties of YSOs and clumps in the region.

### 6.4.1 The state of star formation in Serpens MWC 297

Star formation is active and ongoing over a wide range of physical stages, from prestellar objects to Class III PMS-stars. We have detected 22 clumps in SCUBA-2 850  $\mu\text{m}$  data using the clump-finding algorithm **FELLWALKER** (Table 6.1), from which we classify eight as YSOcs through consistency with 24  $\mu\text{m}$  data and the SGBS YSOc catalogue. We include an additional *Spitzer*-detected YSOc (YSOc 11) which was missed by **FELLWALKER** to provide us with a sample size of nine (Table 6.3), in addition to the  $10 M_{\odot}$  ZAMS star MWC 297. Seven (YSOc 2, 11, 17, 32, 41, 47, 73) of these are found in the SGBS YSOc catalogues and two in the general SGBS source catalogue. Three Class 0, three Class I and three Class II sources are classified with SCUBA-2 data.

72 Class II/III and 10 Class 0/I sources are listed in the SGBS catalogue for the region. We do not expect to detect a high proportion of the Class II objects or any Class III objects with SCUBA-2. Figure 2.4 shows how few of these objects lie within the  $3\sigma$  detection level. We do

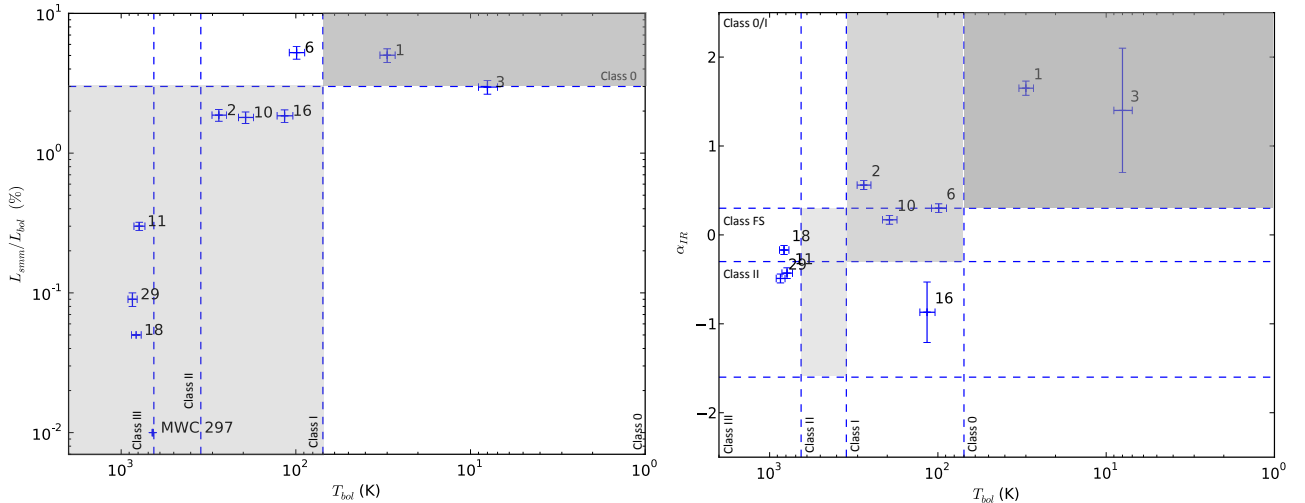


Figure 6.6: Bolometric temperature plotted against  $L_{\text{smm}}/L_{\text{bol}}$  (left) and  $\alpha_{\text{IR}}$  (right) for the 10 YSOs listed in Table 6.3. Dashed lines indicate the boundaries of classification of objects (greyed boxes indicating regions of class space where methods agree).

expect to detect all Class 0 and most Class I objects with SCUBA-2 and therefore four (YSO 15, 16, 21, 38) out of 10 Class 0/I sources listed in the SGBS catalogue that are not associated with SCUBA-2 peaks should be considered with scepticism. The remaining 16 objects identified by `FELLWALKER` are considered to be prestellar objects and diffuse clouds. From the SCUBA-2 catalogue every stage in star formation is represented up to stars on the main sequence. Given the assumed lifetime of each class, star formation has been active in this region for at least 3 Myr.

Star formation is observed at various stages in five large-scale clouds in the region which are composed of a number of fragmented clumps (Figure 7.2), the most evolved of which contain star forming cores. S2-YSOc 1 represents the most massive core we detect at  $5.1 \pm 0.5 M_{\odot}$  and is the most prominent object in a larger cloud of mass  $21 \pm 2 M_{\odot}$  - (see Figure 6.4). S2-YSOc 1 is the coolest YSO we have observed with mean temperature of  $10.3 \pm 0.5$  K and there is no evidence of heating in this region. If all the mass detected in S2-YSOc 1 accretes onto the core, allowing for a star-formation efficiency of 30 per cent (Evans et al., 2009), this object may go on to form an intermediate mass star similar to MWC 297.

A second cloud appears somewhat less fragmented with only two objects as opposed to four but also less massive with a peak core mass of  $1.3 \pm 0.3 M_{\odot}$  and total cloud mass of  $3.5 M_{\odot}$  (Figure 6.4 - S2-YSOc 2). Likewise a 30 per cent star-formation efficiency would limit the final mass to around  $1 M_{\odot}$ . S2-YSOc 3 and 6 (Figures 6.4) form a potentially loosely bound proto-binary composed of a Class 0 and Class I object with separation of 10,000 AU and masses  $0.95 \pm 0.08$  and  $0.62 \pm 0.06 M_{\odot}$ .

In addition to these deeply embedded, less evolved objects, a number of more evolved, isolated objects were observed. S2-YSOc 10, 18 and 29 are detached from the larger clouds and are much less luminous than the younger objects (Figure 6.4). At these stages, PMS-stars are dominated by disks rather than envelopes and we calculate masses of  $0.31 \pm 0.03 M_{\odot}$ ,  $0.09 \pm 0.02 M_{\odot}$

and  $0.30 \pm 0.03 M_{\odot}$  for these objects. The protostar to PMS ratios suggest that these objects may have been formed in a dense region and later ejected or that the associated molecular cloud was larger in the past. Typical core migration speeds of 1 pc per Myr are consistent with the size of the observed region (30' diameter) and birth of these objects in one of the large clouds, most likely that associated with the star MWC 297 as it is the most evolved. S2-YSOc 11 and 16 are likely transition cores between Class I and II stages (Figure 6.4).

The remaining objects are not considered to be star-forming. The most massive of these are SMM 5 and 7 at  $3.5 \pm 0.3$  and  $3.1 \pm 0.2 M_{\odot}$  (see Figure 6.4). We calculate free fall timescales of 2.1 and 1.8 Myrs for these objects. These are significantly larger than the typical protostellar timescale of 0.5 Myr and are therefore unlikely to form stars without accreting mass or cooling further. The mean temperature of starless clumps is over twice that of star-forming cores ( $32 \pm 4$  K to  $15 \pm 2$  K). Our observed core temperature is consistent with the assumption made in Section 4.2 and used by Johnstone et al. (2000) and Kirk et al. (2006). The remaining objects all have masses less than  $1 M_{\odot}$  and are too diffuse to produce reliable temperature data. If these objects go onto to form stars, they are unlikely to form anything more massive than a brown dwarf.

A global analysis of the region reveals that, of a total cloud mass of  $40 M_{\odot}$ , only  $12.5 M_{\odot}$  is not currently associated with ongoing star formation. Assuming a mean YSO mass of  $0.5 M_{\odot}$  based of IMF observations (Chabrier, 2005; Evans et al., 2009), and given a mass of MWC 297 of  $10 M_{\odot}$  (Drew et al., 1997), we conclude that the total stellar (Class II or higher) mass of the region is  $46 M_{\odot}$ . To date, approximately 85 per cent of the original cloud mass has gone into forming stars. From this we conclude that once this current generation of stars are formed, there is unlikely to be any further massive star formation without further mass accreting from the diffuse ISM and as a result we envisage a large distribution of low mass objects with the massive MWC 297 system dominating the region.

#### 6.4.2 What does SCUBA-2 tell us about the star MWC 297?

The B1.5Ve star MWC 297 is a well known object. We comment on its relevant features and refer the reader to Sandell et al. (2011) for a comprehensive review the star's properties.

MWC 297 is considered to be physically associated with the YSOcs within a 1' radius identified in SGBS and the additional YSO catalogues identified in Table 2.3 and displayed in Figure 2.4. MWC 297, objects 2MASS J18273854-0350108 (undetected in SCUBA-2) and 2MASS J18273670-0350047 (detected as S2-YSOc 11 in SCUBA-2) were found to have a mean group velocity of 0.01'' per year (Röser et al., 2008; Zacharias & Zacharias, 2012; Zacharias et al., 2013) providing evidence they were formed from same cloud. Further evidence in 24  $\mu$ m data shown in Figure 6.1c shows how emission from warm dust heated by MWC 297, associated with SH2-62, is consistent with the location of dust clouds in the SCUBA-2 data. The angular distance between MWC 297 and the nearest clump (SMM 4) detected in SCUBA-2 amounts to a minimum physical separation of 5,000 AU, approximately half the size of our definition of a core (0.05 pc, Rygl et al. 2013).

Previous observations have interpreted a submillimetre source consistent with the location of MWC 297 as an accretion disk or circumstellar envelope (Di Francesco et al., 1994; Drew et al.,

1997; Di Francesco et al., 1998). We believe that these observations can now be explained as free-free emission. Manoj et al. (2007) constrain the disk radius with radio observations to 80 AU and calculate a disk mass of  $M = 0.07 M_{\odot}$ . These results are supported by Alonso-Albi et al. (2009) who conclude that this ‘exceptionally low’ disk mass is partly due to photoionisation by an UCHII region. Further work by Alonso-Albi et al. (2009) argues for the presence of a cold circumstellar envelope. Free-free does not account for emission at 70  $\mu\text{m}$  and 100  $\mu\text{m}$  as shown in the SED for MWC 297 (Figure 6.5) due to the exponential cutoff of the free-free power law as emission becomes optically thick at shorter wavelengths.

Our results do not rule out the presence of a disk or residual envelope following subtraction of the free-free emission, but they do confirm that any residual disk is low mass, though with a high degree of uncertainty as the submillimetre flux observed at the position of MWC 297 likely contains a component from the clump SMM 4 which overlaps this location. Temperature information about MWC 297 is also limited by the diminished size of the residual emission. We note that throughout this paper we have assumed a constant value of  $\beta = 1.8$ . We have argued this a fair assumption for the ISM and extended envelope but this does not hold for the local environment of the protostar where the value of  $\beta$  is known to be lower, leading to higher dust temperatures (see Figure 5.1).

Based on these observations we suggest the following arrangement whereby we are observing both the B star, MWC 297, and the companion A star, OSCA. MWC 297 has evolved further to the extent that it is producing the UCHII region observed. We find it unlikely that such a system could still be accreting matter on a large scale, or that the magnetic fields required to produce collimated jets could survive the UCHII region, and therefore we associate the jet emission observed by Skinner et al. (1993) to OSCA, an object that may be less evolved and more likely to still be in the accreting phase. Further evidence for active accretion onto OSCA has been provided by Damiani et al. (2006) who found substantial X-ray flaring from the object. A more massive disk structure would likely exist around the lower mass, and therefore less evolved, OSCA than MWC 297 and therefore this is likely the source of any residual SCUBA-2 flux and *Spitzer* MIPS flux observed in the combined SED. The separation at 850 AU is too small to resolve the two objects with the JCMT beam.

#### 6.4.3 Is there evidence for radiative feedback in Serpens MWC 297?

The star MWC 297 is directly associated with the star-forming clumps identified in the SCUBA-2 data and the B star is directly heating those objects, none more so than SMM 4 where our result suggests that MWC 297 is directly influencing its evolution. A mean temperature of  $46 \pm 2$  K for SMM 4 was calculated, almost a factor of three times higher than the typical clump temperature of 15 K. The standard deviation of pixels of this clump is high at 11 K. The clump is warmest around the exterior with temperatures peaking above 55 K (potentially contributed to by edge effects) but it appears to have a cooler centre of 29 K (Figure 6.4). This is warmer than the mean temperature (18 K) of all the other clumps (discounting SMM 22 on account of its small size) detected by FELLWALKER. Heating of this object is not internal and the ISRF is not sufficient to produce such high temperatures. Only MWC 297 can provide sufficient external heating.

SMM 4 has a dust mass of  $0.91 \pm 0.05 M_{\odot}$  but is the fourth most luminous clump in the region with a well defined, centrally condensed core. Raised temperatures mean that the object is gravitationally stable with a  $M_{850}/M_{\mathrm{J}}$  ratio of 0.12. From these results we conclude that, in the past, SMM 4 may have begun collapse on a similar timescale to MWC 297; however upon the B star producing sufficient radiation, MWC 297 has directly heated the larger part of the neighbouring clump to the extent that gravitational collapse is no longer possible, in effect suppressing, or even halting, the star formation process. Whether or not the low mass of SMM 4 or the power of MWC 297 is the limiting factor in this process remains unknown.

The majority of the other clumps detected show little or no external heating and no objects show evidence of internal heating. Table 6.1 outlines a range of mean clump dust temperatures, between 10 and 46 K, across the region. This is wider than the range of 12 to 20 K assumed by Motte et al. (1998) for Ophiuchus. Examining the mean temperatures of the Class 0 objects we find values of  $12.6 \pm 0.9$  K, below the assumed 15 K used by Johnstone et al. (2000) and Kirk et al. (2006) but within the range of Motte et al. (1998). Of the six Class 0/I objects, two (S2-YSOc 2 and 10) lie within the nebulosity whereas the remainder lie in regions with little significant emission from large scale heated dust as shown in Figure 6.4. None of the YSOcs show significant heating. However, use of a constant  $\beta$  may not hold towards the centre of a protostar and our use of  $\beta = 1.8$  specifically for large structures maybe be systematically underestimating temperatures in these regions.

Starless object SMM 7 shows heating (Figure 6.4) along its eastern edge which is not consistent with the  $24 \mu\text{m}$  emission. We suspect we are observing the ‘edge effect’ artefact produced in the map making process and this consequently increases temperature to  $25 \pm 2$  K. Conversely SMM 5 shows evidence of heated gas along its western edge in  $24 \mu\text{m}$  emission (Figure 6.1c) but is relatively cool and homogenous in Figure 6.4 with a mean temperature of  $18.2 \pm 0.9$  K. Prohibitively high noise in the  $450 \mu\text{m}$  data prevent wider examination of this feature.

## 6.5 Conclusion

We observed Serpens MWC 297 region with SCUBA-2 at  $450 \mu\text{m}$  and  $850 \mu\text{m}$  as part of the JCMT Gould Belt Survey of nearby star-forming regions. The observations covers a  $30'$  diameter circular region centred on RA(J2000) =  $18^{\mathrm{h}} 28^{\mathrm{m}} 138$ , Dec. (J2000) =  $-03^{\circ} 44' 1.7''$  including the B1.5Ve Herbig Be star MWC 297 and a collection of local dense clouds. We use the clump-finding algorithm `FELLWALKER` to identify submillimetre clumps in the data and compare our catalogue to YSOc catalogues produced by the *Spitzer* Gould Belt Survey (SGBS), and to *Spitzer*  $24 \mu\text{m}$  data of the region. The latter shows heating of surrounding clouds associated with the star MWC 297 and the optical nebula SH2-62, providing evidence that the two are physically located in space.

We account for sources of submillimetre contamination, finding an insignificant CO contamination estimated at 13 per cent but a significant amount from free-free emission as the result of an ultra-compact HII region and polar winds/jets associated with the star MWC 297. We use the ratio of  $450 \mu\text{m}$  and  $850 \mu\text{m}$  to build maps of dust temperature for Serpens MWC 297 with the aim of investigating evidence for radiative heating in the region. To do this we employed a method

whereby each dataset is convolved with both the primary and secondary beam components of the JCMT beam at the other wavelength to achieve like resolution of  $19.9''$  before calculating the flux ratio and consequently temperature.

Our key results are:

1. Our temperature method uses both the primary and secondary components of the JCMT beam as this better reflects the shape of the real beam. The two component model decreases temperatures between 5 and 9 per cent in the warmest and coolest regions respectively.
2. We detect 22 clumps. By cross referencing this list with *Spitzer* YSOcs and a comparison of mass to Jeans mass as a test of gravitational stability, we identify nine YSOcs
3. We calculated masses based on calculated temperatures (as opposed to an assumed value) across the whole region. Clump masses range between  $0.02\text{-}19 M_{\odot}$  and core masses range between  $0.09\text{-}5.1 M_{\odot}$ . Starless clumps are consistently warmer than star forming cores with mean temperatures of  $32 \pm 4$  K compared to  $15 \pm 2$  K.
4. We classify the YSOs using  $T_{\text{bol}}$  and  $L_{\text{smm}}/L_{\text{bol}}$  as two Class 0, one Class 0/I, three Class I and three Class II sources. 30 per cent of Class 0/I objects and 8 per cent of Class II objects catalogued in SGBS were also detected by SCUBA-2. No Class III objects were detected by SCUBA-2. SCUBA-2 detected two potential Class 0 and one Class I/II YSOcs that were not included in the SGBS YSOc catalogue.
5. We modelled free-free emission from MWC 297 as a point-source with a spectral index of  $\alpha = 1.03 \pm 0.02$ . This contamination accounted for 73 per cent and 83 per cent of peak flux at  $450 \mu\text{m}$  and  $850 \mu\text{m}$  respectively. Residual peak fluxes were  $51 \pm 10$  mJy and  $15 \pm 3$  mJy respectively. The residual submillimetre emission for MWC 297 was insufficiently bright to be distinguishable from a larger clump (SMM 4) projected behind it on the sky.
6. We conclude that radiative heating from one generation of stars is directly influencing the formation of another, but we note that the effect is not large across the region. Our findings suggest that clump SMM 4 had begun collapsing before radiative heating from MWC 297 raised the temperatures to  $46 \pm 2$  K, to the extent that gravitational collapse is now suppressed or even halted.

Serpens MWC 297 region represents a low mass star-forming region with a limited number of YSOcs. We believe that in the future, this region will become dominated by the HII region associated with the star MWC 297. The expansion and shock front of this region will likely play an important role in the subsequent evolution of the cores and clumps we have detected. Further work will look at expanding these methods to produce temperature maps for larger regions within Serpens-Aquila, with a particular eye to possible free-free contamination where OB stars are observed to be forming.

# 7

## Radiative heating in W40 Complex

### 7.1 Temperature maps of the W40 complex

The results of the common resolution convolution kernel maps in the form of SCUBA-2 spectral index  $\alpha$  and temperature are presented in Figures ?? and 7.1 respectively. The range of dust temperatures in the W40 complex are comparable, if warmer than those calculated from SCUBA-2 data in NGC1333 by Hatchell et al. (2013) and in Serpens MWC 297 by Rumble et al. (2015).

The Dust Arc shows a large range of temperatures along its length. Lowest temperatures of  $16\pm2$  K are recorded in the far west of Arc. From there temperatures increase from west to east over a range of approximately 23 K to 33 K. The Arc appears fragmented into a number clumps. These clumps have cooler interiors, with temperatures around  $20\pm1$  K, and significantly warmer exteriors with temperature approaches 50 K with uncertainties between 20 to 30%. The northern side of the Dust Arc has a slight over density of warmer pixels compare to the souther side. It is notable however that the temperature around OS2a are the lowest in the whole region at  $11\pm2$  in spite of allowing for free-free and CO emission.

W40-N is a little studied object as it is not in close proximity to the OB association and star cluster. W40-NA, B and C have a remarkably consistent temperatures with standard deviation of 5 K (compared to 8 K in the Dust Arc). It is significantly cooler than the Dust Arc with a mean temperature of  $21\pm4$  K compared to  $26\pm4$  K.

W40-S is a filament composed of four major clouds. The bulk of the filament is on the periphery of the H II region/nebulosity SH-64. There is a sharp contrast between the temperatures of the four clouds with B and D the warmer bodies both at  $20\pm3$  and  $20\pm3$  K. A and C are significantly cooler with temperatures of  $14\pm1$  and  $16\pm2$  K. In addition to W40-S there are a number of smaller clouds of similar temperatures that are not associated with the three identified regions of

Table 7.1: A sample of submillimetre clumps and their respective SCUBA-2 and *Herschel* fluxes. The full table is available online.

Index <sup>a</sup>	Object name <sup>a</sup>	70 μm flux <sup>b</sup> (MJy/Sr)	450 μm flux <sup>c</sup> (Jy)	850 μm flux <sup>c</sup> (Jy)	21 cm flux <sup>d</sup> (Jy)
W40-SMM1	JCMTLSG J18h31m20.9909s -02d06m20.2932s	8304	93.50	10.44	0.0
W40-SMM2	JCMTLSG J18h31m10.1841s -02d04m41.2862s	3834	56.38	6.77	0.0
W40-SMM3	JCMTLSG J18h31m10.3844s -02d03m50.2869s	3622	71.64	9.26	0.0
W40-SMM4	JCMTLSG J18h31m09.5833s -02d06m26.2843s	1982	26.72	3.06	0.0
W40-SMM5	JCMTLSG J18h31m21.1910s -02d06m56.2928s	5007	41.98	4.73	0.0
W40-SMM6	JCMTLSG J18h31m10.5841s -02d05m41.2859s	2322	54.28	6.54	0.0
W40-SMM7	JCMTLSG J18h31m16.7880s -02d07m05.2899s	4854	62.94	6.87	0.0
W40-SMM8	JCMTLSG J18h31m46.8079s -02d04m26.2952s	2185	46.21	5.96	0.0
W40-SMM9	JCMTLSG J18h31m38.8027s -02d03m35.2982s	3533	32.30	3.77	0.0
W40-SMM10	JCMTLSG J18h31m03.7784s -02d09m50.2738s	344	24.63	3.57	0.0

<sup>a</sup>Position of the highest value pixel in each clump (at 850 μm).

<sup>b</sup>Mean *Herschel* 70 μm flux of the clumps.

<sup>c</sup>Integrated SCUBA-2 fluxes of the clumps. The uncertainty at 450 μm is 0.017 Jy and at 850 μm is 0.0025 Jy. There is an additional systematic error in calibration of 10.6 and 3.4 % at 450 and 850 μm.

<sup>d</sup>Absolute mean VLA 21 cm flux of the clumps.

the W40 complex.

## 7.2 The SCUBA-2 clump catalogue

In this section we use the Starlink `fellwalker` algorithm to identify clumps in the SCUBA-2 850 μm, CO subtracted, 4' filtered, free-free subtracted data. We determine clumps' fluxes, temperatures, column densities and YSO densities. We calculate masses, Jeans masses, Jeans stability and projected distance between each clump and OS1aS (from here on in referred to as OS1a), the primary ionising star in the OB association.

### 7.2.1 Clumpfinding analysis

In this section we use the clump-finding algorithm `fellwalker` (Berry, 2014) to extract a catalogue of irregular clumps from the SCUBA-2 850 μm data (Figure 2.3). Each clump then forms the basis of a mask for the temperature map (Figure 7.1) so that a single clump temperatures can be found and used to calculate various additional properties.

Details of how we apply `fellwalker` to SCUBA-2 data are given in Rumble et al. (2015). By setting the parameter `MinDip` =  $3\sigma$ , `fellwalker` is tuned to breakup large-scale continuous clouds with multiple bright cores into discrete clumps. Noise and `MinHeight` parameters were set to  $5\sigma$  and `MaxJump` was set to one pixel ensuring that all extracted clumps were significant detections but allowing for fragmentation peaks. By setting `MinPix` to four pixels, a large number of single pixel objects which were likely noise artefacts were removed from the catalogue.

The original observations also include objects that are part of Serpens South which is located near to the W40 complex on the sky. There is no physically defined point in the SCUBA-2

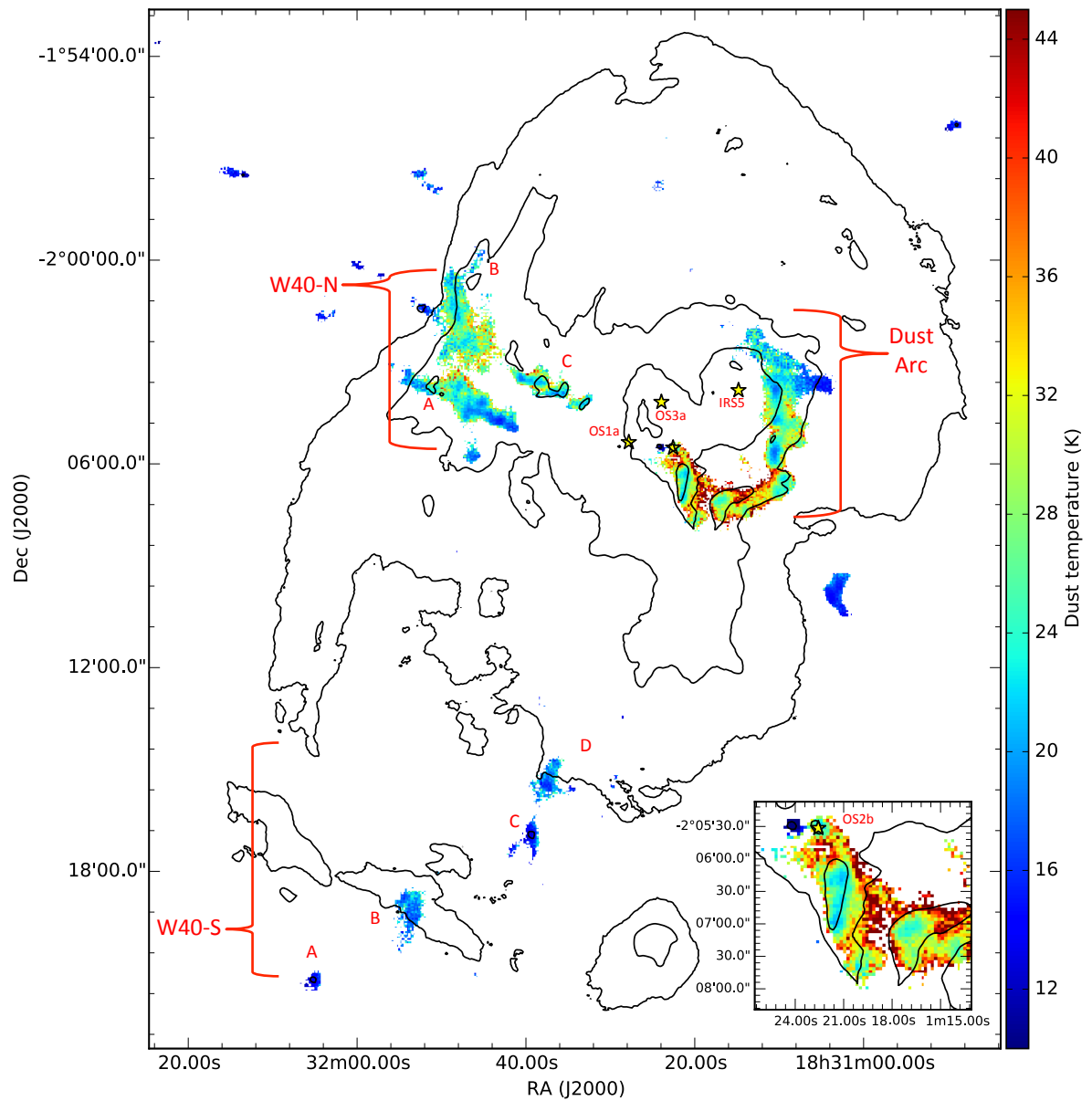


Figure 7.1: Temperature map of the W40 complex with *Herschel* 70  $\mu\text{m}$  contours at 300, 1200, 4800 and 12000 MJy/Sr.

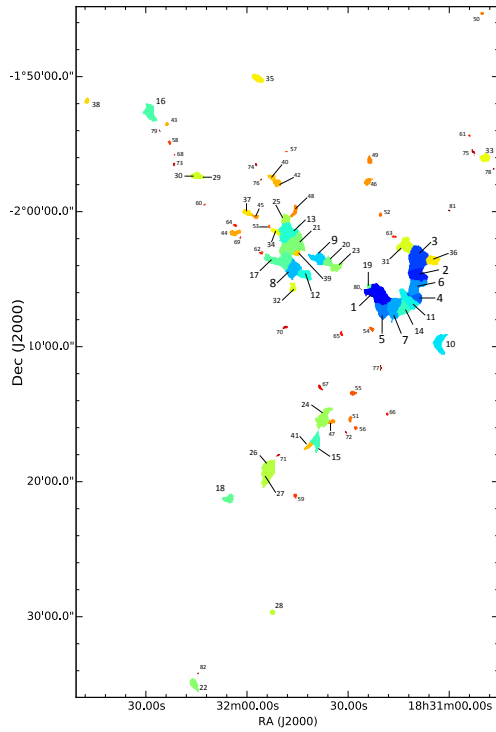


Figure 7.2: Clumps identified in the SCUBA-2 CO subtracted, 4' filtered and free-free subtracted 850  $\mu\text{m}$  data using the Starlink clump-finding algorithm `fellwalker`. Clumps are indexed in order of highest to lowest flux density which matches the order presented in Tables 7.1 and 7.2.

data that describes where the W40 complex ends and Serpens South begins and so we define an arbitrary cut off along the line of  $\text{RA}(\text{J2000}) = 18:30:40$  with all eastward points belonging to the W40 complex and westward points belonging to Serpens South. Whilst this approach may risk associating some clumps with the wrong cloud, we estimate this will affect less than 5% of members overall. We identify 82 clumps in the W40 complex and their fluxes at 70, 450, 850  $\mu\text{m}$  and 21 cm are presented in Table 7.1. Clump positions are presented in Figure 7.2.

### 7.2.2 Clump Temperatures

The mean temperature for clumps in the W40 complex is calculated and presented in Table 7.2. 21 clumps detected at 850  $\mu\text{m}$  are not detected at 450  $\mu\text{m}$  and therefore do not have associated temperature data. For these cases we assign a temperature of  $15 \pm 2$  K, consistent with Rumble et al. (2015). Where temperature data only partially covers the 850  $\mu\text{m}$  clump we assume the vacant pixels have a temperature equal to the mean of the occupied pixels. The W40 complex has a broad spread of temperatures between 10 and 37 K (as shown in Figure 7.3) with a modal value of 17 K.

The mean percentage error in temperature across all clumps is 16% due to calibration uncertainty. This corresponds to an uncertainty of 3 K on the mean clump temperature of 19 K. This mean clump temperature is larger than the  $15 \pm 2$  K found by Rumble et al. (2015) in the Serpens MWC 297 region. The Dust Arc is notably warmer than the other major clouds in the region with

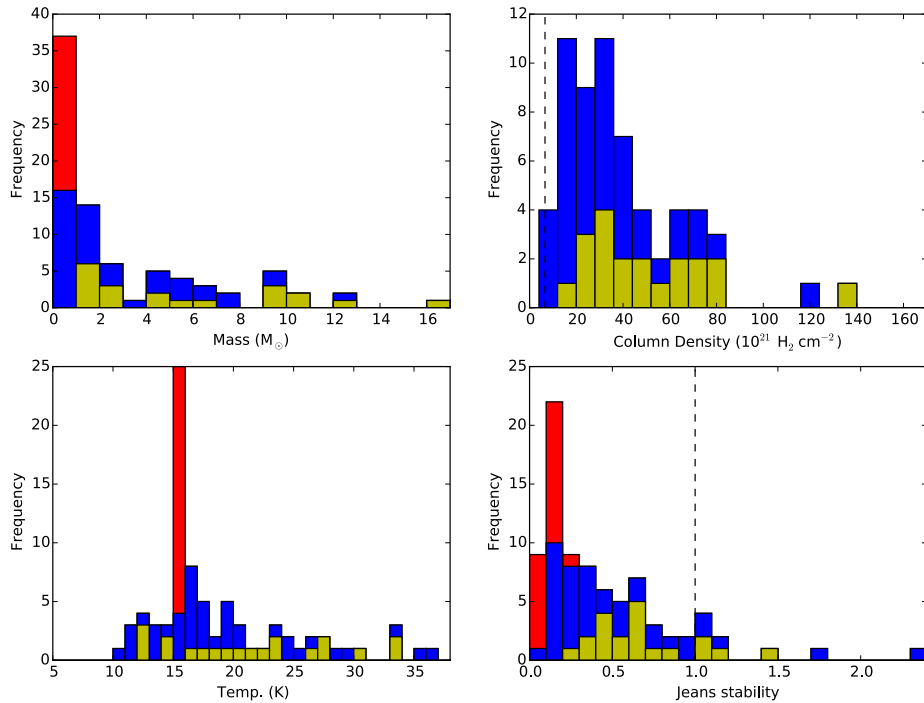


Figure 7.3: Histograms of the properties of clumps within the W40 complex. Top left) describes mass segregation, top right) column density segregation, bottom left) temperature distribution of clumps and bottom right) Jeans stability of clumps. Total height of bars includes the full set of clumps. Blue is a subset of clumps that have real, calculated temperature, yellow is further subset of clumps with real temperature and at least one YSO present within the body of the cloud. Red bars show those clumps where no temperature data is available therefore a value of  $15 \pm 2 \text{ K}$  (Rumble et al., 2015) has been assumed for the purpose of these calculations.

Table 7.2: The properties of a sample of submillimetre clumps in the W40 complex. The full table is available online.

Index	$S_{850}^a$ (Jy)	Mass <sup>b</sup> ( $M_\odot$ )	Temp <sup>c</sup> . (K)	Column density <sup>d</sup> ( $H_2 \text{ cm}^{-2}$ )	YSO density <sup>e</sup> (YSO pc <sup>2</sup> )	Protostars <sup>e</sup> (per clump)	$M_J^f$ ( $M_\odot$ )	M/ <sup>f</sup>
W40-SMM1	10.44	$12.5 \pm 2.6$	$33.6 \pm 5.7$	$75 \pm 16 \times 10^{21}$	147	4	$20.6 \pm 3.5$	0.6
W40-SMM2	6.77	$9.65 \pm 1.66$	$28.1 \pm 3.7$	$69 \pm 12 \times 10^{21}$	17	0	$12.9 \pm 1.7$	0.8
W40-SMM3	9.26	$16.63 \pm 3.32$	$23.0 \pm 3.2$	$83 \pm 17 \times 10^{21}$	22	1	$14.6 \pm 2.0$	1.1
W40-SMM4	3.06	$4.01 \pm 0.67$	$30.2 \pm 3.9$	$62 \pm 10 \times 10^{21}$	26	1	$9.2 \pm 1.2$	0.4
W40-SMM5	4.73	$5.55 \pm 1.15$	$33.1 \pm 5.5$	$57 \pm 12 \times 10^{21}$	86	1	$13.8 \pm 2.3$	0.4
W40-SMM6	6.54	$9.92 \pm 1.66$	$27.8 \pm 3.7$	$73 \pm 12 \times 10^{21}$	21	1	$12.9 \pm 1.7$	0.8
W40-SMM7	6.87	$7.3 \pm 1.48$	$35.8 \pm 6.0$	$44 \pm 8.8 \times 10^{21}$	47	0	$18.1 \pm 3.0$	0.4
W40-SMM8	5.96	$10.82 \pm 1.72$	$23.8 \pm 2.8$	$60 \pm 10 \times 10^{21}$	25	1	$10.6 \pm 1.3$	1.0
W40-SMM9	3.77	$5.97 \pm 1.24$	$26.3 \pm 4.2$	$48 \pm 10 \times 10^{21}$	56	0	$10.4 \pm 1.6$	0.6
W40-SMM10	3.57	$10.52 \pm 1.78$	$16.5 \pm 1.6$	$80 \pm 14 \times 10^{21}$	36	2	$7.3 \pm 0.7$	1.5

<sup>a</sup>Integrated SCUBA-2 850  $\mu\text{m}$  fluxes of the clumps. The 850  $\mu\text{m}$  uncertainty is 0.0025 Jy. There is an additional systematic error in calibration of 3.4 %.

<sup>b</sup>As calculated with equation 7.1. These results do not include the systematic error in distance (10 %) or opacity (100 %).

<sup>c</sup>Mean temperature as calculated from the temperature maps. Where no temperature data is available an arbitrary value of  $15 \pm 2$  K is assigned that is consistent with previous authors (Johnstone et al. 2000, Kirk et al., 2006, Rumble et al. 2015).

<sup>d</sup>Peak column density of the clamp. These results do not include the systematic error in distance (10 %) or opacity (100 %).

<sup>e</sup>Calculated from composite YSO catalogue outlined in Section 2.3.

<sup>f</sup>As calculated with Equation 7.3. These results have a systematic uncertainty due to distance of 10 %.

<sup>g</sup>Projected distance between clump and OS1a, the primary ionising star in the W40 complex OB association.

a mean temperature of  $26 \pm 4$  K compared to W40-N ( $21 \pm 4$  K) and W40-S ( $17 \pm 3$  K). The mean temperature of the peripheral clumps is  $15 \pm 2$  K. Given that these mean temperatures are calculated from clumps with measured temperatures only, it is remarkable that the mean temperatures for an isolated clump is identical to that in the Serpens MWC 297 region (Rumble et al., 2015) and completely consistent with the assumptions used by Johnstone et al. (2000) and Sadavoy et al. (2010).

W40-SMM 35 is the coolest of the regular clumps with a temperature of  $10 \pm 1$  K. This temperature is comparable with the Class 0 object S2-YSOc1 detected in the Serpens MWC 297 region (Rumble et al., 2015) and we find that this small clump contains a single YSO. The clump is isolated from the rest for the W40 complex, outside the main nebulosity Sh-64, and away from any active areas of star-formation as it has limited *Herschel* 70  $\mu\text{m}$  flux of 1300 MJy/Sr. W40-SMM 7 and 14 are the warmest clumps detected both with temperatures of  $36 \pm 6$  K. Both are neighbouring clumps found in the Dust Arc, approximately 0.5 pc from OS1a.

### 7.2.3 Clump column density and mass

SCUBA-2 850  $\mu\text{m}$  fluxes,  $S_{850}$ , listed in Table 7.1 are used to calculate the mass of the clumps in the W40 complex by assuming a single temperature grey body spectrum (Hildebrand, 1983). We follow the standard method for calculating clump mass for a given distance,  $d$ , and dust opacity,  $\kappa_{850}$ , (Johnstone et al. 2000; Kirk et al. 2006; Sadavoy et al. 2010; Enoch et al. 2011). Masses are calculated by summing fluxes over pixels  $i$  using

$$M = 0.39 \sum_i S_{850,i} \left[ \exp\left(\frac{17\text{ K}}{T_{d,i}}\right) - 1 \right] \times \left( \frac{d}{250\text{ pc}} \right)^2 \left( \frac{\kappa_{850}}{0.012\text{ cm}^2\text{ g}^{-1}} \right)^{-1}. \quad (7.1)$$

There is a high degree of uncertainty in the value of  $\kappa_{850}$ . We follow the popular OH5 model of opacities in dense ISM, with a specific gas to dust ratio of 161, giving  $\alpha = 0.012\text{ cm}^2\text{ g}^{-1}$  though Henning & Sablotny (1995) finds that  $\kappa_{850}$  can vary by up to a factor of two. This model is consistent with  $\beta = 1.8$  over a wavelength range of 30  $\mu\text{m}$ –1.3 mm. We assume a distance  $d = 500 \pm 50$  pc following Mallick et al. (2013) as outlined in Section 1.

Figure 7.3 shows the distribution of clump masses in the W40 complex. The total mass of all clumps in the W40 complex is  $239 \pm 9 M_\odot$ . 50% of all clumps have a mass of  $1.2 M_\odot$  or less whereas the 12 most massive clumps contain more mass than all the others combined. Five clumps have masses greater than  $10 M_\odot$  with W40-SMM3 the most massive clump at  $17 \pm 3 M_\odot$ . The Dust Arc, W40-N and W40-S have collective masses of  $87 \pm 6$ ,  $73 \pm 5$  and  $31 \pm 3 M_\odot$  respectively confirming the Dust Arc as the most massive structure in the W40 complex. W40-SMM 10 and 16 are two clouds that, with masses of  $11 \pm 2$  and  $12 \pm 2 M_\odot$ , are amongst the most massive in the complex. However, they are isolated clouds well outside of Sh2-64. Like W40-SMM 22, 33 and 35, these peripheral clouds all have relatively low temperatures often less than 15 K.

Maps of column density are presented in Figure 7.4 and 7.3. Previous authors (Johnstone et al., 2000; Sadavoy et al., 2010) have often used an assumed constant temperature in this cal-

culation. However, we can now incorporate temperature measurements alongside the SCUBA-2 850  $\mu\text{m}$  fluxes to calculate column densities from pixel masses,  $M_i$ , using the standard method of mass per unit area,  $A_i$  and the mean molecular mass, per H<sub>2</sub>, ( $\mu=2.8$ , Kauffmann et al. 2008),

$$N_{i,\text{H}_2} = \frac{M_i}{\mu_{\text{H}_2} m_p A_i}. \quad (7.2)$$

We find the range of peak column densities across our sample of clumps to be 8 to 136  $\times 10^{21}$  H<sub>2</sub> cm<sup>-2</sup>. The median clump column density is  $22 \times 10^{21}$  H<sub>2</sub> cm<sup>-2</sup> which is larger than the  $7 \times 10^{21}$  H<sub>2</sub> cm<sup>-2</sup> reported by Konyves et al. (2015) using *Herschel* data because the atmospheric subtraction with of SCUBA-2 results in a selection basis that omits the low column density clumps from the sample (Ward-Thompson et al., 2015).

We calculate the average volume density along the line of sight for clumps from peak column density and mean clump size along the x and y axis, as calculated by **FELLWALKER**, to obtain a lower limit on clump density. From this we define a list of ‘dense cores’ where the density limit is greater than  $10^5$  cm<sup>-3</sup> (the threshold density of star-formation) and the effective size is greater than the typical core diameter of 0.05 pc (Rygl et al., 2013). In total, 33 dense cores are listed in Table 7.3, along with any known YSO within the clump and the Jeans stability of the clump. The Dust Arc has nine cores, W40-N has nine cores, W40-S has four and there are 11 isolated dense cores. In total 40% of the cores have densities greater than  $10^{-5}$  cm<sup>-3</sup> confirming that significant proportion of clumps in the W40 complex are likely undergoing star-formation.

W40-SMM 19 is the densest core with a peak column density of  $135 \pm 29 \times 10^{21}$  H<sub>2</sub> per cm<sup>-2</sup> (volume density  $13.8 \times 10^5$  cm<sup>-3</sup>). As outlined in Section 4.21, the SCUBA-2 spectral index for this object, after accounting for free-free emission, is suspiciously low. Given its prominent location at the centre of the stellar cluster (YSO-density of 234 YSOs pc<sup>-2</sup>) and the confirmed presence of an UCH<sub>II</sub> region associated with the Herbig Be star, we have reason to believe the minimum temperature of 8.8 K calculated for this clump, and therefore the density, is unreliable.

W40-SMM 16 has a peak column density of  $120 \pm 19 \times 10^{21}$  H<sub>2</sub> per cm<sup>-2</sup> which is comparable to W40-SMM 19. However the volume density is approximately a third at  $3.7 \times 10^5$  cm<sup>-3</sup>. For the reasons outlined, we believe that this core is a cool, massive, isolated core and therefore the calculated high densities of W40-SMM 16 are reliable.

#### 7.2.4 Clump Stability

The Jeans instability (Jeans, 1902) defines a critical ratio, above which the force of gravitational collapse will overwhelm thermal support in a idealised cloud of gas, causing it to collapse and begin star-formation (Sadavoy et al., 2010; Mairs et al., 2014). The condition for collapse is defined as when the mass of a clump,  $M_{850}$ , is greater than the Jeans mass,

$$M_J = 1.9 \left( \frac{\bar{T}_d}{10 \text{ K}} \right) \left( \frac{R_J}{0.07 \text{ pc}} \right) M_\odot, \quad (7.3)$$

where  $\bar{T}_d$  is mean clump temperature and  $R_J$  is the effective radius of the clump, as determined by clump area (in pixels) from **FELLWALKER**, assuming spherical structure and that the

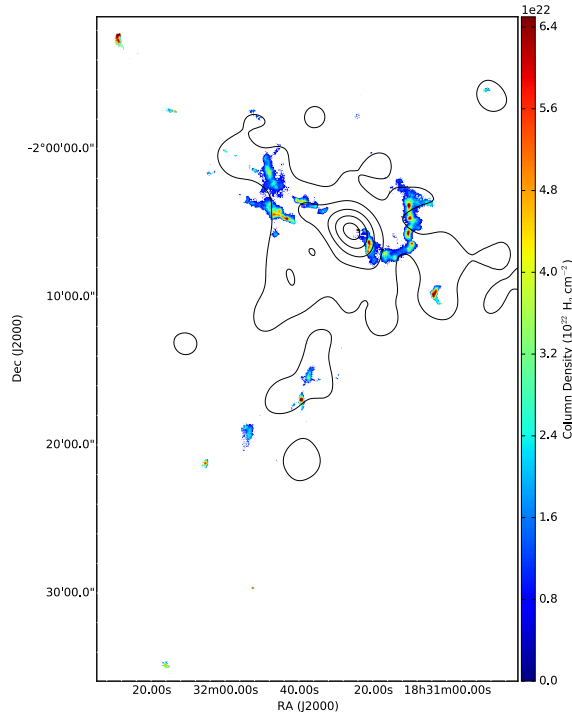


Figure 7.4: SCUBA-2 column density map of the major parts of the W40 complex. Prepared using temperature maps presenting in Figure 7.1 for a constant  $\beta = 1.8$ . Contours describe YSO surface density with levels at 20, 60, 110, 160 and 210 YSO pc $^{-2}$ .

effective radius is less than that of the clump. Alternatively the condition of Jeans instability can be written as  $M_{850}/M_J \geq 1$ . Rumble et al. (2015) covers this method in more detail.

Clump instability is presented in Table 7.2 and Figure 7.3. Of the 82 clumps in the W40 complex, we find that 10 are unstable. We have confidence that W40-SMM 16, 35 and potentially 10 are unstable and may collapse to form stars because they have  $M_{850}/M_J \geq 1.5$ . Again, all three of these objects are cool clumps on the periphery of the OB association, with projected distances of approximately 2.9, 2.4 and 1.1 pc from OS1a.

Despite having the most mass in the region, the clumps in the Dust Arc are mostly below the threshold required for collapse. The same is true for the clumps in W40-N. It is important to note that whilst the Dust Arc is significantly warmer than W40-N ( $26 \pm 4$  K to  $21 \pm 4$  K) giving it a mean Jeans mass of  $9.8 M_\odot$ , Figure 7.4 shows dense cores along the breadth of the filament. Contrast that with W40-N where dense cores are confined to W40-SMM 8 and 12. For overdensities like these to occur suggests that these respective clumps have already begun to collapse, despite not being Jeans critical, suggesting that external pressure could be contributing to overcoming thermal support.

By contrast, W40-S contains four major clumps where column density appears correlated with stability. W40-SMM 15 and 18 are Jeans critical and both have high column densities of  $79 \pm 15$  and  $61 \pm 11 \times 10^{21} \text{ H}_2 \text{ cm}^{-2}$  whereas W40-SMM 24 and 27 have lower densities of  $38 \pm 10$  and  $32 \pm 8 \times 10^{21} \text{ H}_2 \text{ cm}^{-2}$  and are both sub-critical. Stability is listed alongside the dense cores in Table 7.3.

Table 7.3: Dense cores in the W40 complex.

Clump ID (W40-SMM)	Radius <sup>a</sup> (pc)	Density <sup>b</sup> ( $\times 10^5$ cm $^{-3}$ )	Protostars	M/M <sub>J</sub>
1	0.14	1.7	4	0.6±0.2
2	0.10	2.2	-	0.8±0.2
3	0.14	1.9	1	1.1±0.3
4	0.07	3.0	1	0.4±0.1
5	0.12	1.7	1	0.4±0.1
6	0.12	1.9	1	0.8±0.2
7	0.12	1.2	-	0.4±0.1
8	0.10	1.9	1	1.0±0.2
9	0.09	1.7	-	0.6±0.2
10	0.11	2.4	2	1.5±0.3
12	0.09	2.7	-	1.0±0.2
13	0.13	1.1	1	0.7±0.2
14	0.10	1.1	-	0.3±0.1
15	0.09	3.0	-	1.1±0.2
16	0.10	3.7	-	2.3±0.4
18	0.07	3.0	-	1.0±0.2
20	0.07	1.6	-	0.3±0.1
22	0.07	2.5	n/a <sup>c</sup>	1.0±0.2
23	0.07	1.2	-	0.3±0.1
25	0.07	1.4	-	0.3±0.1
26	0.06	2.1	-	0.4±0.1
30	0.06	1.9	-	0.6±0.1
32	0.06	1.2	1	0.3±0.1
33	0.07	1.8	2	0.7±0.2
34	0.06	1.7	1	0.4±0.1
35	0.08	2.1	-	1.8±0.4
36	0.09	1.1	-	0.9±0.2
37	0.06	1.7	1	0.8±0.2
40	0.05	1.3	-	0.3±0.1
41	0.06	1.2	-	0.4±0.1
42	0.06	1.1	1	0.3±0.1
44	0.07	1.1	-	0.5±0.2
46	0.60	1.1	-	0.3±0.1

<sup>a</sup> Effective radius calculated from effective area by the clump-finding algorithm `fellwalker`.<sup>b</sup> A lower limit of the average volume density of a dense core along the line of sight.<sup>c</sup> Clumps beyond the coverage of our composite YSO catalogue.

### 7.2.5 YSO distribution

In this section we consider the YSO distribution based on the composite YSO catalogue produced from the SGBS merged with the catalogues published by Kuhn et al. (2010), Rodríguez et al. (2010), Maury et al. (2011) and Mallick et al. (2013). The YSO distribution was mapped by convolving the YSO positions with a 2' FWHM gaussian to produce a surface density map up to units of YSOs per pc<sup>2</sup> as shown in Figure 7.4. The stellar cluster is visible in Figure 7.4 and has a FWHM size of approximately 3'30'' × 2'30''. The Dust Arc has its east end located towards the centre of the star cluster where density peaks at 232 YSOs pc<sup>2</sup>. However, this value quickly drops off to 20 YSOs pc<sup>2</sup> at its western edge at W40-SMM 31. Overall the Dust Arc has an average density of 61 YSOs pc<sup>2</sup> which is significantly more than either W40-N (26 YSOs pc<sup>2</sup>) or W40-S (17 YSOs pc<sup>2</sup>).

In addition to the surface density, the absolute number of YSOs located within the body of the clump was also recorded. Given its proximity to the peak YSO surface density and the size of the clump, it is unsurprising that W40-SMM 1 has the largest number of embedded YSOs at nine. A total of 21/82 clumps have at least one Class 0/I protostar.

In addition to low mass stars, the proximity of clumps to high mass stars is also estimated through the projected distance between the clump and the primary ionising star OS1a. The ability of this star to heat its surroundings is evidenced through the presence of an H II region producing the radio emission seen in Figure 4.1 where gas temperatures are at a minimum of 10,000 K. Comparisons between clump temperature and distance can be used to determine what effect, if any, the massive stars in the W40 complex are having on the dust temperatures.

## 7.3 Discussion

In this paper, we use SCUBA-2 450 and 850  $\mu\text{m}$  data to investigate the role of radiative feedback in star-formation in the W40 complex, whilst accounting for known sources of submillimetre contamination. We observed  $^{12}\text{CO}$  3–2 345 GHz line emission which is known to contaminate the SCUBA-2 850  $\mu\text{m}$  band (Drabek et al., 2012) and analysed archival VLA 3.6 (Rodríguez et al., 2010) and 21 cm (Condon & Kaplan, 1998) data for traces of free-free emission (Olonon, 1975) from both large-scale H II and small-scale UCH II regions .

We conduct a clump analysis, using the clump-finding algorithm `fellwalker` (Berry, 2014), on the 850  $\mu\text{m}$  flux density maps of the W40 complex and we calculate masses, column densities, Jeans masses and stability of 82 clumps in the region using real temperatures calculated from flux ratio using a constant  $\beta$  of 1.8 and a model convolution kernel (Aniano et al., 2011; Pattle et al., 2015). We can now compare our results for clumps to various features of the W40 complex, namely proximity of YSO populations, massive stars and the H II region.

In this discussion section we first examine the evidence for radiative feedback from internal and external sources influencing clump temperature. We then look at what SCUBA-2 and HARP data, as well as *Herschel* and VLA data, can tell us about the stars that have formed and are currently forming, before addressing whether there is evidence that radiative feedback is influencing the star-formation process.

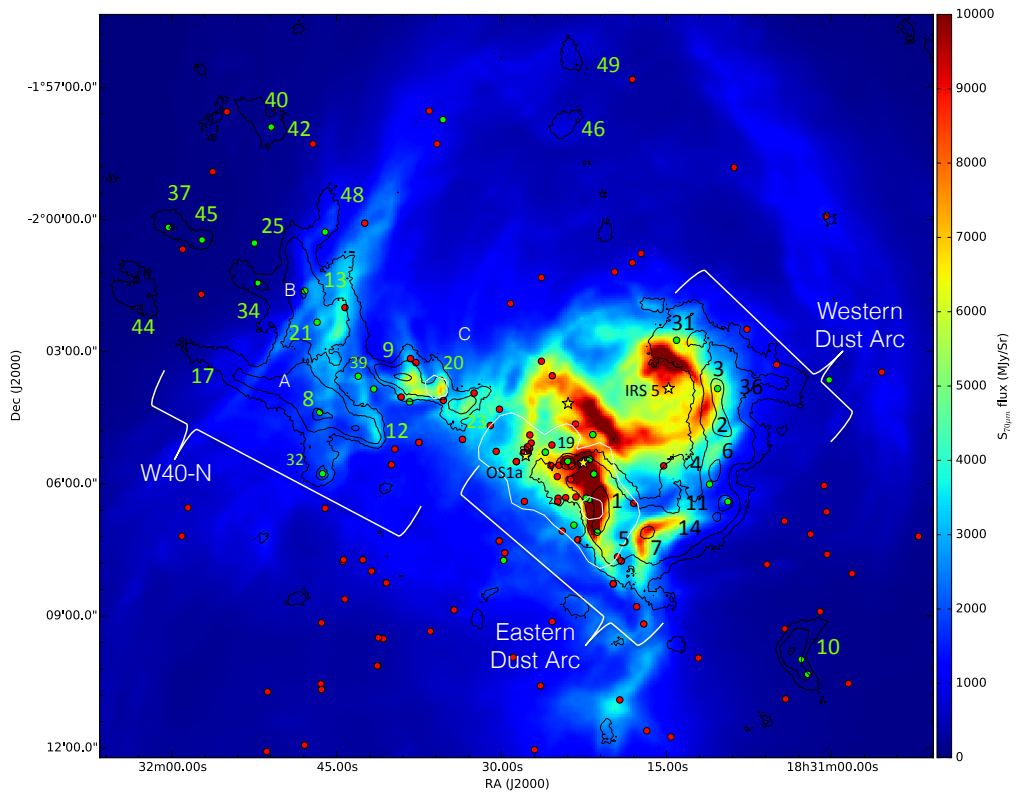


Figure 7.5: *Herschel* 70  $\mu\text{m}$  flux density map of the W40 complex. Morphological features of W40-N and the Dust Arc are labelled along side major clumps detected in SCUBA-2 850  $\mu\text{m}$  emission (see Figure 7.2 for accurate clumps positions). Black contours show SCUBA-2 850  $\mu\text{m}$  at the 5 $\sigma$  and 50 $\sigma$  level. Red contours show HARP  $^{12}\text{CO}$  3–2 redshifted ( $10.5 \text{ km s}^{-2}$ ) emission at 5, 25 and 75  $\text{K km s}^{-1}$ . White contours show archival VLA 21 cm emission at 5 $\sigma$  and 25 $\sigma$  (Condon & Kaplan, 1998).

### 7.3.1 What evidence is there of radiative feedback heating the clumps in the W40 complex?

The W40 complex is home to a number of prominent sources of radiative feedback. Photons from OS1a and its companion B stars are ionising molecular hydrogen gas that is subsequently detected as free-free emission at radio wavelengths as seen in Figure 4.1. Lower energy photons have produced the nebulosity SH2-64 which is detected by *Herschel* at 70  $\mu\text{m}$  where dust is being heated. In addition to this, Pirogov et al. (2013) argues that IRS 5 is powering a secondary H II region, a secondary bubble nebulosity is observed around IRS 5 in the *Herschel* 70  $\mu\text{m}$  flux data shown in Figure 7.5. *Chandra* observations by Kuhn et al. (2010) have revealed a significant PMS-star cluster alongside the OB association. Submillimetre observations by Maury et al. (2011) have found populations of protostars embedded deep within the molecular clouds which we confirm with SCUBA-2 supported by up to 12 molecular outflows identified in  $^{12}\text{CO}$  3–2 observations (Figure ??).

### 7.3.2 External heating

We first address the sources of external heating in the W40 complex (see Figure 7.6). We find that there is a strong correlation between clump temperature and proximity to OS1a. The population of clumps at distances greater than 1.2 pc (marked) has an average temperature of  $16 \pm 3$  K, again consistent with the isolated clumps and the literature (Johnstone et al. 2000, Kirk et al. 2006 and Rumble et al. 2015). At distances less than 1.2 pc there is a strong negative correlation between temperature and proximity to OS1a, with the exception of W40-SMM 19 (which has an anomalous spectral index, as discussed in Section 5).

VLA 21 cm emission traces free-free continuum emission. As discussed in Section 1, low density H II regions have temperatures of at least 10,000 K required to ionise hydrogen. Figures 4.1 and 4.6 shows the extent of the H II region. Relative to the nebulosity, the H II region is small in size, however it does coincide with several of the SCUBA-2 clumps in the Dust Arc and W40-N. Of the clumps that overlap the H II region, none have a temperature of less than 21 K (ignoring the anomaly of W40-SMM 19) and the mean clump temperature of 29 K is almost twice that of the typical clump temperature of 15 K (Johnstone et al. 2000, Kirk et al. 2006 and Rumble et al. 2015).

This step in clump temperatures is also observed when temperature is plotted as a function of YSO density (Figure 7.6). Above a density of  $45 \text{ YSO pc}^{-2}$  (marked) the mean clump temperature is 28 K whereas below the mean is 19 K. There is deficit of warm clumps at low densities with no clumps exceeding temperatures of 20 K below  $10 \text{ YSO pc}^{-2}$ . As discussed, our YSO catalogue does not distinguish between embedded protostars and free-floating PMS-stars and therefore the YSO density will be an over-estimate of the density of objects embedded within the clump.

Each temperature relation plotted in Figure 7.6 show some correlation indicative of clump temperature increasing to over double the literature value (15 K) of a star-forming core towards the centre of the cluster. None of our tests, proximity to OB stars, YSO density or an H II region, are mutually exclusive from the others so critical evaluation is required to determine which is the

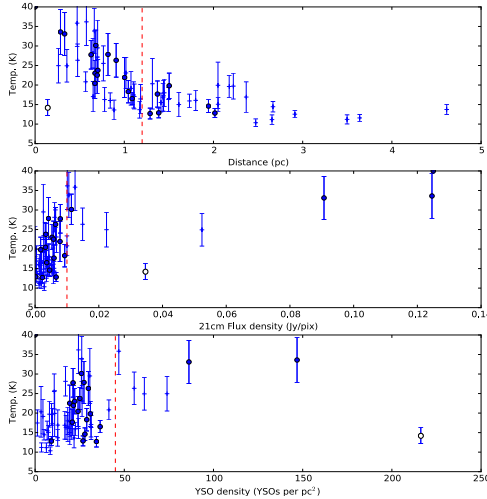


Figure 7.6: Plots describing clump temperature as a function of; top) distance, in pc, to OS1a, the most powerful star in the W40 complex, middle) mean VLA 21 cm flux detected in the area of each clump and bottom) YSO surface density. Circle markers indicate that that clump has at least one YSO detected within it.

dominant factor, and which, if any, influence on clump temperature.

Evaluating these results, we find that the FWHM of the YSO surface density and the  $5\sigma$  level of 21 cm flux have a similar size of approximately  $3'30'' \times 2'30''$ , and are both centred on OS1a. We therefore conclude that the similarity of trends between the H II region and the YSO surface density is likely coincidental. Given the uncertainties inherent in our YSO catalogue outlined in Section 1, we conclude that the radiative feedback from OS1a that is producing the H II region is dominating over any potential heating by embedded YSO within this region. The size of the H II region corresponds to a 0.17 pc radius, however Figure 7.6 shows temperatures increasing by 1/radius from OS1a out to 1.2 pc ( $8' 15''$ ). Our conclusions support those of Matzner (2002) in that radiative feedback from the OB association (including ionising and non-ionising photons) is the dominant mechanism for heating clumps.

### 7.3.3 Internal heating

Addressing internal sources of radiative feedback requires an assessment of embedded star-formation occurring within the clumps. The individual locations of YSOs in our composite catalogue, described in Section 2.2, are plotted in Figure 7.7 with green markers indicating Class 0/I protostars and red markers indicating Class II/III PMS-stars. Yellow bars in Figure 7.3 show how the distribution of protostars appears largely random compared to mass ( $\geq 1 M_{\odot}$ ), column density ( $\geq 12 \times 10^{21} H_2 \text{ cm}^{-2}$ ), temperature and stability suggesting that the presence of a protostar in a clump has a negligible impact on these properties.

OS2b appears embedded in the tip of W40-SMM1 in Figure 4.7 and an unresolved peak in SCUBA-2 emission at 450 and 850  $\mu\text{m}$  is detected, suggesting that we are observing a protostellar envelope. This provides a good case to examine as to whether massive protostars are significantly

heating their environment. The B4 classification of the star lead us to conclude that the electron density is insufficient for the free-free emission to be optically thick in the submillimetre. With negligible free-free contribution and CO contamination, we are confident that the temperatures presented in the Figure 7.1 are accurate to the best of our knowledge.

We record a mean temperature for the object of  $31 \pm 1$  K for a beam sized aperture centred on OS2b. This is over twice the temperature of a typical star-forming core but consistent with the average temperature of W40-SMM1 ( $34 \pm 6$  K). Given the proximity to the OB association, we might expect the outer layers of this core to be heated by radiative feedback from OS1a. A better test of whether this object is providing significant internal heating is to measure of the temperature of the dust at the centre of the core (defined as the peak of local SCUBA-2 emission) which is  $21 \pm 2$  K. This is comparable to the central temperatures of cores with low mass protostars in the Dust Arc and W40-N (19 K). We therefore conclude that there is no evidence that stars up to B4 in class can significantly heat their protostellar environment.

There is evidence that significantly powerful protostellar outflows can contribute additional localised dust heating through shocks (Buckle et al., 2015). Outflows have been detected in the W40 complex by Zeilik & Lada (1978) and more recently van der Wiel et al. (2014) found red and blue shifted line wings in the eastern Dust Arc. Our HARP data extends this coverage to the whole of the Dust Arc and W40-N (Figure 3.1). We detect 12 potential molecular outflows which are presented in Figure ???. The highest velocity line-wings of  $8.7 \text{ km s}^{-1}$  are recorded in outflow B5-4, thought to be associated with a protostar in W40-SMM2. Line-wings found in Serpens Main by Graves et al. (2010) are detected out to  $-30 \text{ km s}^{-1}$  and  $+37 \text{ km s}^{-1}$  from an ambient cloud of similar velocities to the W40 complex. We conclude that the outflows in the W40 complex are relatively weak and that the radiative feedback from outflows is negligible, relative to the levels of the radiative feedback from the protostar itself.

We therefore conclude that, whilst there is evidence for internal feedback mechanisms through embedded protostars and outflows, there is no evidence that protostars up to B4 in class can significantly heat the dust.

### 7.3.4 What is the state of star-formation in the W40 complex?

Our results show significant heating of filaments and dust clouds by radiative feedback from the OB association in the W40 complex. We now discuss what evidence exists to suggests that stars are forming in the W40 complex, and whether radiative feedback is influencing this.

### 7.3.5 First generation star-formation

The first generation of star-formation concerns the OB association, associated stellar cluster and their immediate environment. Figure 7.7 shows the FWHM contour of YSO surface density for this cluster from which we calculate an effective cluster width of  $3'(0.44 \text{ pc})$ . The association of the stellar cluster and the OB stars OS1a, OS2b and OS3a is well known. Accounting for the mass of the OB stars (Table 4.1, Shuping et al. 2012) and a population of 36 PMS-stars within the cluster (based on the modal mass of  $1 M_{\odot}$ ), we estimate that the total mass required to form this first

generation of stars was  $76 M_{\odot}$  with a high-to-low stellar cluster mass ratio (the ratio of OB stars to all other stars) of approximately 1:1. Allowing for a regional star-formation efficiency (SFE) of 40% (Konyves et al., 2015), this would require  $190 M_{\odot}$  to form. This value is approximately 79% of the total mass detected by SCUBA-2, inferring that an upper limit of stellar cluster that could form in a second generation would be at most 25% more massive than the first generation cluster.

The bulk of the stellar cluster and H II region lie in a cavity in the SCUBA-2 emission, with the exception of the eastern end of the Dust Arc. In the previous section we argued that such extreme proximity to the OB association, as opposed to the stellar cluster, was a significant factor in the raised temperatures observed in the eastern Dust Arc. Figure 7.7 shows how W40-SMM 1 and 5 contains a population of protostars but also a significant density of PMS-stars. By definition, all PMS-stars will have shed the majority, if not all of their pre-stellar envelopes and therefore we would not anticipate that they would be embedded in a filament at this stage of their life. Assuming that these PMS-stars are instead cluster members of OS1a would likely place them inside H II region surrounding this star and any embedding we observe would likely be caused by chance for/background alignment of the Dust Arc with the cluster.

HARP data is found to contain two clouds at  $5 \text{ km s}^{-1}$  and  $10 \text{ km s}^{-1}$  that trace different morphological structures (Figure 3.4). The redshifted filament starts in W40-N and traces a line from this cloud to the tip of the Dust Arc. The emission from  $^{12}\text{CO}$  3–2 is detected in SCUBA-2 850  $\mu\text{m}$  and closely fits the HARP data, albeit at high SNRs, as shown in Figure 3.4 and 7.5. The red filament appears passes directly through the stellar cluster, enveloping the location of OS1a and H II region shown in Figure 7.5.

CO gas undergoes photodissociation in H II regions and this would lead us to believe that this filament is either shielding CO gas from the UV photons, or that the gas is sufficiently in the foreground or background to the extent they are not located within the H II region. SCUBA-2 does not detect a significant dust filament consistent with redshifted CO and therefore we discount the former premis. Figure 7.5 shows how clumps W40-SMM 12, 13, 20, 21, 23 and 39 are consistent both with bright rimmed clouds (BRCs) observed in *Herschel* 70  $\mu\text{m}$  data and also peaks of redshifted CO emission. This confirms that the CO gas is within the nebulosity, but outside of the H II region. This is consistent with the findings of Shimoikura et al. (2015) who concludes the redshifted filament is a shell of heated CO gas swept up in the expanding shock wave of the around the H II region and we can conclude that many of the line-wing detections in Figure ?? are likely caused by shocks as opposed to protostellar outflows.

The size of the H II region is measured as  $6' \times 3'$  by Sharpless (1959) and Vallee & MacLeod (1991). Based on *Herschel* 70  $\mu\text{m}$  data we measure the size of the wider nebulosity SH2-64 as approximately  $11' \times 28'$ . Given that the CO gas filament runs parallel to the major-axis of the H II region, and assuming ellipsoidal symmetry, we place a lower limit of distance of the redshifted emission at 0.22 pc in the foreground/background relative to OS1a. BRCs are found along the length of W40-N and the eastern Dust Arc and confirm that they are located within the nebulosity. We find these features are located along the ‘neck’ of SH2-64. Assuming typical hourglass structure (Rodney & Reipurth, 2008) for the larger nebulosity we can place an upper limit of the distance of OS1a to the nearest edge of SH2-64 at 0.8 pc.

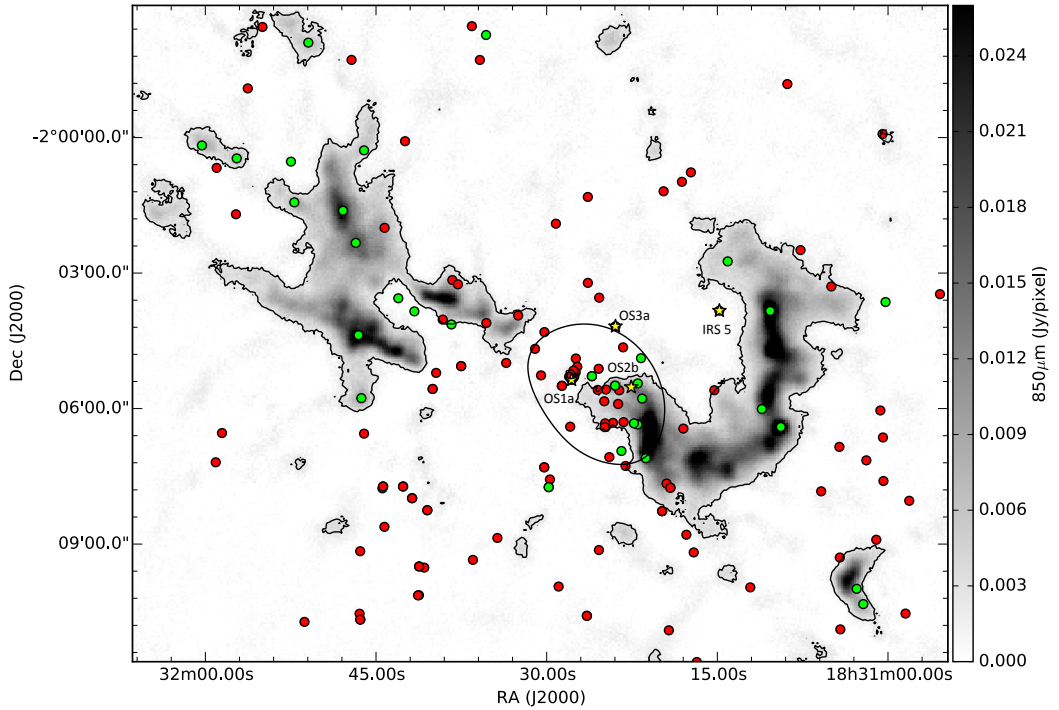


Figure 7.7: SCUBA-2  $850\text{ }\mu\text{m}$  flux density map. The 4 OB stars OS1a, 2a, 3a and IRS 5 are marked in yellow. YSOs from our composite catalogue are displayed. OB stars are marked in yellow, protostars (Class 0/I) are marked as green and PMS-stars (Class II/III) are marked as red. The black contour indicates the  $5\sigma$  level of the SCUBA-2  $850\text{ }\mu\text{m}$  flux. The FWHM of the YSO surface density (an effective size of the stellar cluster) is also shown.

The SGBS detects a significant number of free-floating Class II objects that formed in the first generation of stars and have subsequently dispersed (Figure 7.7). However only one of these PMS-stars is detected as low mass (less than  $1 M_{\odot}$ ) disc by SCUBA-2. This implies that these PMS-stars are sufficiently distant that their discs are too faint to be detected by the JCMT. This is not the case of PMS-stars in the Serpens MWC 297 region which is believed to be part of the less distant Aquila rift (250 pc). The non-detection of PMS stellar discs in the W40 complex is further evidence that this region is at greater distance than the Serpens South region.

Based on the evidence presented and discussed, we conclude that the initial phase of star-formation in the W40 complex used approximately 44% of the initial cloud mass available to produce three OB stars and a stellar clusters of PMS-stars. This system lies offset, along the line of sight, from the Dust Arc and W40-N by approximately 0.58 and 1.60 pc such that the filaments observed by SCUBA-2 lie outside of the H II region, but within the larger nebulosity SH2-64.

### 7.3.6 Second generation star-formation

Secondly we consider the current generation of stars that are forming in the W40 complex. Nominal these are where dense cores (Table 7.3) are found within the filaments and clouds. We find that 13 out of 33 of our dense cores contain a protostar and the remaining cores are likely starless.

W40-S resembles a typical star-forming filament that has undergone collapse and fragmen-

tation into a row of clouds such as Chamaeleon region (Boulanger et al., 1998; Young et al., 2005; Belloche et al., 2011). At this stage the morphology of the clouds resemble a filament running SE to NW that has undergone collapse and fragmentation into four major sub-clouds. A and C have column densities in excess of  $60 \times 10^{21} \text{ H}_2 \text{ cm}^{-2}$ , over twice that of B and D. SGBS has not detected any protostars within any of these clouds, inferring that they are starless. Assuming a SFE of 40% (Konyves et al., 2015), we estimate that clouds A and C will go onto form stars of between 1 to  $2 M_\odot$ . At present the temperatures of B and D are around 20 K, whereas A and C have a mean temperature of 15 K. If B and D were to cool sufficiently they could collapse and form stars. All four clouds in W40-S have a mean mass of  $6 \pm 1 M_\odot$ , but exactly what has caused A and C to begin collapse whilst B and D remain stable remains an open question.

W40-N is a large and fairly continuous cloud with nine dense cores. It has a comparable mass, temperature and number of dense cores to the Dust Arc. Four out of nine contain a protostar in W40-N and five out of nine contain a protostar in the Dust Arc and we therefore conclude that they are at a similar stage of evolution. Many of the dense cores in W40-N have corresponding BRCs (Figure 7.5). Exposure to radiation pressure from OS1a may have triggered the star-formation process in these cores, whereas those clumps less exposed have yet to become Jeans unstable and start collapsing. However, we cannot rule out the possibility that these dense cores existed prior to massive stars, and that the radiation from OS1a has cleared the low density extremities of the envelope to expose the cores.

We therefore conclude that, like W40-S, W40-N is in the process of forming its first generation of stars, yet unlike W40-S, W40-N does not appear to be fragmented into starless clouds, perhaps as a result of the larger scale merger of two massive filaments (Mallick et al., 2013). There is  $73 \pm 5 M_\odot$  of dust and gas available to form a new star cluster with up to one accompanying massive star. However it is important to note that the future path of star-formation in W40-N will be greatly influenced by the development of OS1a and its H II region.

The Dust Arc is a very complex filament and its nature is much debated. Our discussion of star-formation the Dust Arc is split into the relatively simple western Dust Arc and the more complex eastern Dust Arc.

The western Dust Arc leads from W40-SMM 31 southeast towards W40-SMM 11 and includes the B1 star IRS 5 which appears to be producing a secondary nebulosity (visible in *Herschel* 70  $\mu\text{m}$  data, Figure 7.5, that is consistent with H $\alpha$  emission presented in Mallick et al. (2013)). A population of Class 0/I protostars are observed in the western Dust Arc (Maury et al., 2011), some of which coincide with dense cores W40-SMM 2, 3, 4 and 6. Typical mass of each star-forming clump is  $9 M_\odot$  with the most massive clump (W40-SMM 3,  $17 \pm 3 M_\odot$ ) having the potential to form a B-type star. This filament lies well outside of the main stellar cluster associated with OS1a and has a with a YSO density of  $22 \text{ YSO pc}^{-2}$ , is comparable to W40-N.

Some of the most potent outflows we detect are found in the western Dust Arc. Figure ?? shows the outflow B5-4 subtending 3' (0.43 pc) in length from the the protostar W40-MM5 (Maury et al., 2011) in W40-SMM3 supporting the detection of Class 0 objects in the western Dust Arc. As discussed in Section 6.1, the size of these line-wings are not particularly exceptional and given a clump mass of  $12.5 \pm 2.6 M_\odot$  we would anticipate that low-to-intermediate mass star-

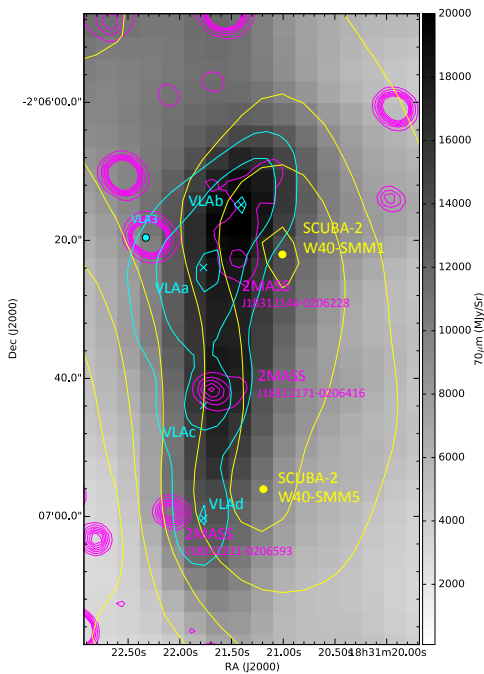


Figure 7.8: Archival Herschel 70  $\mu\text{m}$  data. Magenta contours (560, 570, 580, 590, 600, 610, 620 mag.) show a number of 2MASS point sources embedded within the eastern Dust Arc (shown in the yellow SCUBA-2 850  $\mu\text{m}$  5, 10, 20, 40, 60, 80 $\sigma$  contours with circle markers at the peaks of the W40-SMM1 and 5 clumps). Cyan crosses show the four peaks in Archival AUI/NRAO 3.6 cm map (contours at 0.01, 0.016 and 0.021 Jy/beam). The Rodriguez et al. 2010 YSO ‘VLA3’ is also shown.

formation to be occurring. W40-SMM2 is the only significant clump in the western Dust Arc that does not have a protostar recorded in our composite YSO catalogue. No significant CO line-wing emission is detected, confirming that this clump is starless.

Despite its classification as a B1V star, we do not include IRS 5 in the main OB association for the following reasons. Firstly, it has no corresponding H II region that is detected at 21 cm by the VLA (Figure 4.1). Its own nebulosity appears not only much smaller than OS1a (2.75' compared 11') suggesting that it is considerably less evolved, but also that it appears as a distinct bubble within SH2-64. The distances measured by Shuping et al. (2012) places IRS 5 in the foreground, relative to the OB association, and in all likelihood outside of the main nebulosity. Typical ‘chevron’ shaped BRCs from the secondary nebulosity are observed pointing back towards IRS 5 (as opposed to OS1a, W40-SMM7 Figure 7.5) in the western Dust Arc. We therefore conclude that the western Dust Arc is also outside of the nebulosity, though the connection to the eastern Dust Arc confirms that the total line of sight distance between OS1a and IRS 5 is of the order 1 pc. Likewise BRCs in the eastern Dust Arc confirm that this filament lies within the nebulosity produced by OS1a.

The eastern Dust Arc is a very complex region of star-formation running from W40-SMM 19 to 14 in Figure 7.2. We have discussed how there is evidence for two cloud components in the HARP data and how emission from W40-SMM 1 is the brightest across *Herschel*, SCUBA-2 and VLA wavebands. We have summarised how we believe this region to lie close to, but outside the main stellar cluster and H II region around the OB association.

Significant heating is observed around the outside of the clumps in the eastern Dust Arc (see insert Figure 7.1) and all the clumps (excluding W40-SMM 19) are Jeans stable. A mean clump temperature of  $35 \pm 5$  K is the highest of all clumps in the W40 complex. Such high temperatures, as a result of exposure to radiative feedback from OS1a, are leading to increased stability of the clouds, making gravitational collapse due to (lack of) thermal support less likely.

$^{12}\text{CO}$  3–2 (Figure ??) shows many line-wing sources to the north and south of W40-SMM1 from both the 5 and  $10\text{ km s}^{-1}$  clouds. Given that this clump contains four protostars (Table 7.3) with a further one in W40-SMM5, it is not possible to assign individual outflows to protostars, or to rule out that the line-wings could be caused by shocked gas swept up in a shell where the H II region interacts with the filament. The absence of CO line-wing sources in the vicinity of the YSOs near OS2b does suggest that either; these are particularly low mass protostars with weak outflows, that the majority of the  $^{12}\text{CO}$  3–2 has been photo-ionised by the H II region or that protostars detected here are false detections.

Compact radio sources in part of the eastern Dust Arc are observed by Rodríguez et al. (2010) and are plotted in Figure 4.3 where they are aligned with the lower resolution archival AUI/NRAO 3.6 cm data and the 2MASS source catalogue. Rodríguez et al. (2010) does not cover the four brightest peaks in the AUI/NRAO 3.6 cm data that lie to the south west, referred to as VLAA, b, c and d (Figure 7.8). These objects are orders of magnitude more bright than the Rodríguez et al. (2010) sources and appear in close proximity to strong  $850\text{ }\mu\text{m}$  emission. Examining the 2MASS source catalogue we find that J18312171-0206416 is consistent with the location of VLAc. J18312144-0206228 is misaligned from VLAA and b by an average of  $6.5''$

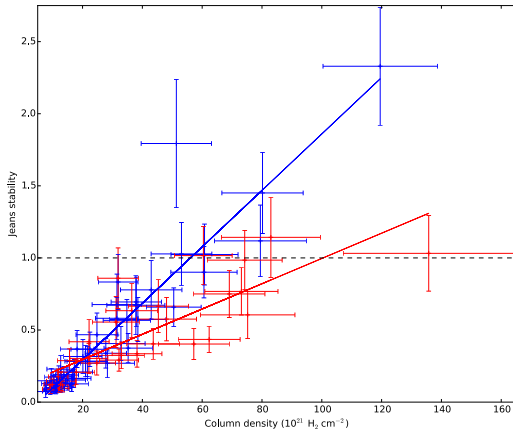


Figure 7.9: Jeans stability as a function of column density. Exterior periphery clumps (defined as having a mean *Herschel* 70  $\mu\text{m}$  flux of less than 1000 MJy/Sr) are marked in blue, interior clumps within the nebulosity SH2-64 are marked in red. The unweighted linear regression fit to each population is marked as a line of the same colour.

whilst J18312211-0206593 is misaligned from VLAd by 5''. Each 2MASS source is deeply reddened, consistent with an embedded YSO suggesting that these could be young massive protostars. Examining the 70  $\mu\text{m}$  data, where the blackbody spectrum of a star is at its peak, FIR emission is brightest in W40-SMM1 around the location of J18312144-0206228. There is also significant emission from location of J18312171-0206416 but not from J18312211-0206593 as shown in Figure 7.8.

We interpret bright *Herschel* 70  $\mu\text{m}$  emission consistent with bright free-free emission as heated dust and dense, ionised hydrogen along the surface of the filament detected in SCUBA-2. There are two potential scenarios that could be providing this. Firstly, this is a shock/ionisation front from where the OS1a H II region is interacting with the eastern Dust Arc (Vallee & MacLeod, 1991). Using Kurtz et al. (1994)'s Equation 4 we calculate a Lyman photon density of  $4.0 \times 10^{46} \text{ s}^{-1}$  required to produce a total flux density of 0.167 Jy for all four unidentified VLA sources at 3.6 cm. We compare this value to the Lyman photon density produced by OS1a, a 09.5v star which is the primary ionising source of the H II region. We assume a minimum distance of 3', consistent with Vallee & MacLeod (1991), and calculate that the proposed ionisation would be exposed to at most 2.1% Lyman photons produced by OS1a at this distance, corresponding to a Lyman photon density of at least  $1.67 \times 10^{46} \text{ s}^{-1}$ . The shortfall in photon density is equivalent to that of a single B0.5 star.

The second scenario proposes that the free-free emission detected is produced by a second generation of massive star-formation blistering from the eastern Dust Arc. This claim is supported by the detection of deeply reddened 2MASS objects which coincide with the peak in *Herschel* 70  $\mu\text{m}$  emission, and by the shortfall in Lyman photons provided by OS1a indicating further massive stars are required to ionise all the gas observed. Pirogov et al. (2013) observes CS 2–1 line emission and finds evidence of infalling motion in the eastern Dust Arc and concludes that massive star formation is probably occurring. <sup>12</sup>CO 3–2 is heavily affected by self-absorption in this complex region so a search for outflows and line-wings is of no further help here (Figure ??). Assuming the 1:1 high-to-low stellar cluster mass ratio would allocate approximately  $18 \pm 3 M_{\odot}$

of material available to form massive star which, given a SFE of 40%, would be sufficient to form an B0.5 protostar as proposed.

Having weighed up the evidence we conclude that the majority of the 3.6 cm flux detected in W40-SMM1 is likely caused by ionisation from OS1a where the high density filament interacts with the boundary of the H II region. However there is a case to be made for the formation of at least one massive star within the filament (most likely J18312171-0206416), albeit extremely embedded. Further high resolution radio imaging of this region is required to confirm whether the radio emission is amorphous or ultra-compact in nature.

With regard to the Dust Arc as a whole, we conclude that we are observing a diverse filament that is in the early stages of star-formation. The filament could be of the order one pc in length, running from near the interior of the SH2-64, where dust is heated by the OB association and massive stars may be forming, to beyond the nebulosity where IRS 5 has formed alongside a number of dense cores.

Finally, in addition to a second generation of stars forming in the major clouds in the W40 complex, there are many isolated clouds, some of which are forming stars. The vast majority of these are low mass, low column density and rarely contain YSOs. Two notable exceptions are W40-SMM 10 and 16, which are the two most massive and dense cores in the sample of isolated clouds. It is likely that these are fragmented clouds of the filaments feeding the complex that have become sufficiently cool that they can collapse and likely form a small cluster of medium to low mass stars.

### 7.3.7 What evidence is there of radiative feedback influencing star-formation in the W40 complex?

Evidence from the Serpens MWC 297 region suggests that radiative feedback from massive stars can raise the temperature and potentially suppress star-formation in neighbouring clumps (Rumble et al., 2015). In the prior sections we have concluded that there are several sources of internal and external heating in the W40 complex. It is extremely difficult to disentangle these mechanisms in the eastern Dust Arc, but we can confirm that the dust clouds here are being heated, and we proceed to address the question of whether or not this is influencing star-formation.

We conclude that the eastern Dust Arc is positioned outside of the H II region, but inside of the nebulosity SH2-64. There is evidence to suggest that a single B0.5 star may be forming, in addition to a small number of low mass protostars and starless clouds, in keeping with a high-to-low stellar cluster mass ratio of 1:1 as observed in the star cluster around OS1a. Raised temperatures mean the clumps in the eastern Dust Arc are a factor of two from Jeans instability so these clumps would need to cool significantly before collapse and further star-formation can occur. Given the impending expansion of the H II region around OS1a and any additional massive stars, this seems an unlikely scenario.

In contrast, the more massive clumps in the western Dust Arc are borderline Jeans unstable. We find that five dense cores have formed, three of which contain protostars. We conclude that in the past these clumps were sufficiently cool as to induce collapse. Subsequent radiative heating by IRS 5 may have warmed the less dense, outer layers of these cores, though this nebulosity is

still in its infancy. An alternative explanation could be that pressure exerted on the filament by the radiative bubble triggered the collapse of sub-critical cores. Such an argument would forego the requirement for pre-existing over-densities in a filament. However, we observe density peaks along the length of the filament, not just limited to where the radiative bubble of IRS 5 is interacting with it, and therefore we believe this alternative explanation to be less valid.

Given a common CO gas velocity (Figure 3.1) we have reason to believe that the Dust Arc, as a whole, is a continuous filament, and therefore we might expect it to evolve on similar timescales. In the east we observe a number of low-mass protostars with no significant CO outflows (Figure ??) or SCUBA-2 peaks (Figure 7.7) suggesting that these objects are more evolved, potentially Class I objects. In the west the protostars are typically found at the centre of dense cores and we identify associated outflows, suggesting that these protostars are less evolved, Class 0 objects. These findings fit with those of Maury et al. (2011), Mallick et al. (2013) and Pirogov et al. (2013) who conclude that the eastern Dust Arc is more evolved than the western end.

We find that the eastern filament appears largely stable whereas the west of the Dust Arc is less stable and appears to be cooling and fragmenting into star-forming dense cores, behaviour that is typical for filaments, as observed in W40-S. We believe that we may be observing two stages in the evolution of the Dust Arc. In the first phase, prior to the maturity of OS1a, the filament cooled and began to collapse. In the second stage, radiative feedback and interaction from the H II region is heating the filament in the east, increasing stability and potentially preventing further fragmentation of collapse of the low-to-intermediate density dust clouds. In the west the clumps have continued to evolve relatively unperturbed, prior to IRS 5 reaching maturity.

We further examine the impact of radiative feedback from the OB association on the global sample of clumps in the W40 complex by comparing the stability of the population inside the nebulosity to the outside. The limit of the nebulosity is defined as where the mean  $70\text{ }\mu\text{m}$  flux is less than  $1000\text{ MJy/Sr}$  and these populations plotted in Figure 7.9. A degree of correlation is expected as both Jeans stability and column density are derived from our flux and temperature data. Two correlations are observed with a clear divergence between the two clump populations. Clumps with the same peak column densities found within the nebulosity are more likely to be stable than those on outside.

We conclude that Figure 7.9 provides direct evidence that radiative heating from the OB association is directly influencing the stability and the star-formation within SH2-64. We note that whilst the divergence is prominent amongst clumps with high column densities, the two populations have similar distributions below  $55 \times 10^{21}\text{ H}_2\text{ cm}^{-2}$ . This supports our conclusions that the influence of radiative heating on clump stability is more prominent where collapse has already begun, and that photons are proficient at heating the low density outer envelope but much less effective at heating the dense interior of a core.

## 7.4 Conclusion

We observed the W40 complex with SCUBA-2 at 450 and  $850\text{ }\mu\text{m}$  as part of the JCMT GBS of nearby star-forming regions. The observations covers four,  $30'$  diameter PONG regions that were

subsequently mosaiced together. The  $^{12}\text{CO}$  3–2 line at 345.796 GHz was observed separately using HARP. The observations cover two sets of four basket-weaving scan maps covering an area of approximately  $7'\times18'$  centred on RA(J2000) = 18:31:29.0, Dec.(J2000) = -02:03:45.4. HARP data was used to run a CO subtraction from the SCUBA-2 850  $\mu\text{m}$  map. Archival radio data from Condon & Kaplan (1998) and Rodríguez et al. (2010) are examined to asses the large and small scale free-free contribution of the massive stars in the W40 complex OB association to both SCUBA-2 bands.

By taking the ratio of SCUBA-2 fluxes, for constant dust spectral index,  $\beta = 1.8$ , we produce maps of dust temperature and column density and calculate the Jeans stability of submillimetre clumps, as identified by the clump-finding algorithm `fellwalker`. Our method uses a model beam convolution kernel which convolves the 450  $\mu\text{m}$  map up to the 850  $\mu\text{m}$  resolution of 14.6''. We examine clump temperatures, in conjunction with our composite YSO candidate catalogue, to draw conclusions about whether there is evidence that dust is being heated, whether this is caused by internal or external mechanisms and what implications this has for star-formation in the region. Throughout this paper we refer to the Dust Arc, W40-N, W40-S and isolated clumps as various morphological features of the W40 complex.

Our key results on the clouds are as follows:

1. We find evidence for two velocity clouds (at 5  $\text{km s}^{-1}$  and 10  $\text{km s}^{-1}$ ) in the HARP data that trace different structure within the W40 complex.  $^{12}\text{CO}$  3–2 contamination of the 850  $\mu\text{m}$  band ranges between 3 and 10% in the majority of the filaments and in a minority of areas reaches up to 20%. Removing the  $^{12}\text{CO}$  3–2 contamination significantly increases the calculated dust temperatures.
2. There is evidence for five confirmed and seven candidate outflows in the W40 complex. The most significant outflow has a line-wing of 8.7  $\text{km s}^{-1}$  which is relatively weak compared to those in the nearby Serpens Main region (Graves et al., 2010). Due to the complex nature of the region it is difficult to distinguish between protostellar outflows and shocked shell material around the H II region. We note that dense clouds at 7  $\text{km s}^{-1}$  are extinguishing  $^{12}\text{CO}$  3–2 line emission and as a result at most 50% of outflows will be detected.
3. Large scale free-free emission from an existing H II region (spectral index of  $\alpha_{\text{ff}} = -0.1$ ) powered by the primary ionising star OS1a contributes 0.5% of flux at 450  $\mu\text{m}$  and 5% at 850  $\mu\text{m}$ .
4. The contribution of small scale free-free emission from UCH II regions around six massive stars (spectral index of  $\alpha_{\text{ff}} = 0.6$  to 1.0) is analysed. Free-free emission from OS2a contributes 9 and 12% at 450 and 850  $\mu\text{m}$  whilst the OS1a cluster contributes 62% at 850  $\mu\text{m}$  and was not detected at 450  $\mu\text{m}$ . Free-free emission for both large and small scale sources was found to have a non-negligible, if limited impact on dust temperature, often within the calculated uncertainties.
5. 82 clumps were detected by `fellwalker`. 21 of these were found to have at least one protostar embedded within them. Clump temperature ranges from 10 to 36 K. The mean temperature of clumps in the Dust Arc, W40-N, W40-S is  $25\pm4$ ,  $20\pm4$  and  $17\pm3$  K. The mean

temperature of the isolated clumps is  $15 \pm 2$  K. This matches the literature values (Johnstone et al., 2000) and those observed in Serpens MWC 297 by Rumble et al. (2015).

6. We find that clump temperature correlates with proximity to OS1a and the H II region. We conclude that external radiative feedback from the OB association is raising the temperature of the clumps. There is no evidence that embedded protostars are internally heating the filaments on a micro or macroscopic scale, though external influences may be masking this. As a result of external radiative feedback the eastern Dust Arc has exceptionally high temperatures (mean  $35 \pm 5$  K) and Jeans stable clouds (mean  $M/M_J = 0.43$ ).
7. It is estimated that  $190 M_\odot$  of material was required for the first generation of star-formation in the W40 complex. The high-to-low cluster mass ratio (OB stars to other cluster members) is approximately 1:1.  $239 \pm 9 M_\odot$  remain placing an upper limit on the second generation of stars of 25% more than the first generation. The Dust Arc is the most massive cloud at  $87 \pm 6 M_\odot$ , followed by W40-N at  $73 \pm 5 M_\odot$  and W40-S at  $31 \pm 3 M_\odot$ .
8. 33 dense cores (volume density greater than  $10^5 \text{ cm}^{-3}$  and effective radius greater than 0.05 pc) are identified, 39% of which contain embedded Class 0/I protostars. Nine dense cores are found in the Dust Arc, nine in W40-N and four in W40-S suggesting that the filaments are evolving under similar timescales. Bright rimmed clouds (BRCs) are observed in *Herschel* 70  $\mu\text{m}$  data along the length of the eastern Dust Arc and W40-N having been formed by the OS1a, confirming that these filaments lie outside of the H II region but inside the nebulosity of SH2-64. BRCs are also observed in the western Dust Arc. However these are formed by the secondary nebulosity around the young B1V star IRS 5 which we consider to be outside of SH2-64.
9. We observe that W40-SMM1 in the eastern Dust Arc has peak flux across all bands we study. We interpret this as where an H II region is interacting with a dense filament. We find that the Lyman photon density from OS1a is insufficient to power this entirely and suggest that at least one reddened and deeply embedded 2MASS source may be a young B0.5ve star to accommodate this shortfall.
10. We find the global population of clumps within the nebulosity SH2-64 are more stable, as a function of peak column density, than those outside. We believe there is sufficient evidence to argue that partial radiative heating of the Dust Arc (internally and/or externally) has influenced the evolution of stars in the filament, favouring massive star growth in the warm east and fragmentation in the cool west.

The W40 complex represents a high-mass star-forming region with a significant cluster of evolved PMS-stars and massive filaments forming new protostars from dense, starless clouds. The region is complex and requires careful study to appreciate which radiative mechanisms, from external and internal sources, are heating clumps of gas and dust. The region is dominated by an OB association that is powering an H II region. In the near future we can expect this H II region to expand and envelop many of surrounding filaments. Within a few Myrs we can expect OS1a to go supernova. This event will have a cataclysmic impact on star-formation within the region. Any filament mass that has not been converted into stars, or eroded by the H II region, will likely be

destroyed at this point, bringing an end to star-formation in the W40 complex in its current format.

# 8

## Radiative heating in JCMT GBS

### **8.1 Temperature maps of the JCMT GBS**

### **8.2 Catalogues**

#### **8.2.1 OB stars**

#### **8.2.2 YSO populations**

### **8.3 The SCUBA-2 clump catalogue**

#### **8.3.1 Clumpfinding analysis**

#### **8.3.2 Clump Temperatures**

#### **8.3.3 Clump column density and mass**

#### **8.3.4 Clump Stability**

#### **8.3.5 YSO distribution**

### **8.4 Global analysis**

#### **8.4.1 Do populations of OB stars influence clump temperature?**

#### **8.4.2 Do populations of YSOs influence clump temperature?**

#### **8.4.3 How do SCUBA-2 temperatures compare to Herschel temperatures?**

# 9

## Conclusions

This thesis has conclusions.

### 9.1 Further work

## Bibliography

- Alonso-Albi T., Fuente A., Bachiller R., Neri R., Planesas P., Testi L., 2008, ApJ, 680, 1289
- Alonso-Albi T., Fuente A., Bachiller R., Neri R., Planesas P., Testi L., Berné O., Joblin C., 2009, A&A, 497, 117
- Altenhoff W. J., Downes D., Goad L., Maxwell A., Rinehart R., 1970, A&AS, 1, 319
- André P., Men'shchikov A., Bontemps S., Könyves V., Motte F., Schneider N., Didelon P., Minier V., Saraceno P., Ward-Thompson D., 2010, A&A, 518, L102
- André P., Motte F., 2000, in Favata F., Kaas A., Wilson A., eds, Star Formation from the Small to the Large Scale Vol. 445 of ESA Special Publication, FIRST and the Earliest Stages of Star Formation. p. 219
- André P., Ward-Thompson D., Barsony M., 1993, ApJ, 406, 122
- Aniano G., Draine B. T., Gordon K. D., Sandstrom K., 2011, PASP, 123, 1218
- Arce H. G., Goodman A. A., 1999, ApJ, 517, 264
- Bate M. R., 2009, MNRAS, 392, 1363
- Belloche A., Parise B., Schuller F., André P., Bontemps S., Menten K. M., 2011, A&A, 535, A2
- Bergner Y. K., Kozlov V. P., Krivtsov A. A., Miroshnichenko A. S., Yudin R. V., Yutanov N. Y., Dzhakusheva K. G., Kuratov K. S., Mukanov B. D., 1988, Astrofizika, 28, 529
- Berrilli F., Corciulo G., Ingrosso G., Lorenzetti D., Nisini B., Strafella F., 1992, ApJ, 398, 254
- Berry D., 2014, ArXiv:1411.6267
- Berry D. S., Reinhold K., Jenness T., Economou F., 2007, in Shaw R. A., Hill F., Bell D. J., eds, Astronomical Data Analysis Software and Systems XVI Vol. 376 of Astronomical Society of the Pacific Conference Series, CUPID: A Clump Identification and Analysis Package. p. 425
- Berry D. S., Reinhold K., Jenness T., Economou F., , 2013, CUPID: Clump Identification and Analysis Package
- Bonnor W. B., 1956, MNRAS, 116, 351

- Bontemps S., André P., Könyves V., Men'shchikov A., Schneider N., Maury A., Peretto N., Arzoumanian D., Attard M., Motte F., Minier V., 2010, *A&A*, 518, L85
- Bontemps S., André P., Terebey S., Cabrit S., 1996, *A&A*, 311, 858
- Boulanger F., Bronfman L., Dame T. M., Thaddeus P., 1998, *A&A*, 332, 273
- Buckle J. V., Drabek-Maunder E., Greaves J., Richer J. S., Matthews B. C., Johnstone D., Kirk H., 2015, *MNRAS*, 449, 2472
- Buckle J. V., Hills R. E., Smith H., Dent W. R. F., Bell G., Curtis E. I., Dace R., Gibson H., Graves S. F., Leech J., Richer J. S., Williamson R., Withington S., Yassin G., 2009, *MNRAS*, 399, 1026
- Calvet N., Gullbring E., 1998, *ApJ*, 509, 802
- Cambrésy L., 1999, *A&A*, 345, 965
- Canto J., Rodriguez L. F., Calvet N., Levreault R. M., 1984, *ApJ*, 282, 631
- Casali M. M., Eiroa C., Duncan W. D., 1993, *A&A*, 275, 195
- Chabrier G., 2005, in Corbelli E., Palla F., Zinnecker H., eds, *The Initial Mass Function 50 Years Later* Vol. 327 of *Astrophysics and Space Science Library*, *The Initial Mass Function: from Salpeter 1955 to 2005*. p. 41
- Chandler C. J., Gear W. K., Sandell G., Hayashi S., Duncan W. D., Griffin M. J., Hazella S., 1990, *MNRAS*, 243, 330
- Chapin E. L., Berry D. S., Gibb A. G., Jenness T., Scott D., Tilanus R. P. J., Economou F., Holland W. S., 2013, *MNRAS*, 430, 2545
- Chavarria-K. C., de Lara E., Finkenzeller U., Mendoza E. E., Ocegueda J., 1988, *A&A*, 197, 151
- Chen H., Myers P. C., Ladd E. F., Wood D. O. S., 1995, *ApJ*, 445, 377
- Clark F. O., 1991, *ApJS*, 75, 611
- Cohen M., Kuhi L. V., 1979, *ApJS*, 41, 743
- Condon J. J., Kaplan D. L., 1998, *VizieR Online Data Catalog*, 211, 70361
- Connelley M. S., Greene T. P., 2010, *AJ*, 140, 1214
- Connelley M. S., Reipurth B., Tokunaga A. T., 2007, *AJ*, 133, 1528
- Curtis E. I., Richer J. S., Swift J. J., Williams J. P., 2010, *MNRAS*, 408, 1516
- Dale J. E., Bonnell I., 2011, *MNRAS*, 414, 321
- Dale J. E., Bonnell I. A., Clarke C. J., Bate M. R., 2005, *MNRAS*, 358, 291
- Dale J. E., Ercolano B., Bonnell I. A., 2012, *MNRAS*, 424, 377

- Dame T. M., Hartmann D., Thaddeus P., 2001, *ApJ*, 547, 792
- Dame T. M., Thaddeus P., 1985, *ApJ*, 297, 751
- Dame T. M., Ungerechts H., Cohen R. S., de Geus E. J., Grenier I. A., May J., Murphy D. C., Nyman L.-A., Thaddeus P., 1987, *ApJ*, 322, 706
- Damiani F., Micela G., Sciortino S., 2006, *A&A*, 447, 1041
- Davis C. J., Dent W. R. F., Matthews H. E., Coulson I. M., McCaughrean M. J., 2000, *MNRAS*, 318, 952
- Davis C. J., Matthews H. E., Ray T. P., Dent W. R. F., Richer J. S., 1999, *MNRAS*, 309, 141
- Deharveng L., Zavagno A., Anderson L. D., Motte F., Abergel A., André P., Bontemps S., Leleu G., Roussel H., Russeil D., 2012, *A&A*, 546, A74
- Dempsey J. T., Friberg P., Jenness T., Tilanus R. P. J., Thomas H. S., Holland W. S., Bintley D., Berry D. S., Chapin E. L., Chrysostomou A., Davis G. R., Gibb A. G., Parsons H., Robson E. I., 2013, *MNRAS*, 430, 2534
- Di Francesco J., Evans II N. J., Caselli P., Myers P. C., Shirley Y., Aikawa Y., Tafalla M., 2007, *Protostars and Planets V*, pp 17–32
- Di Francesco J., Evans II N. J., Harvey P. M., Mundy L. G., Butner H. M., 1994, *ApJ*, 432, 710
- Di Francesco J., Evans II N. J., Harvey P. M., Mundy L. G., Butner H. M., 1998, *ApJ*, 509, 324
- Djupvik A. A., André P., Bontemps S., Motte F., Olofsson G., Gålfalk M., Florén H.-G., 2006, *A&A*, 458, 789
- Dobashi K., Uehara H., Kandori R., Sakurai T., Kaiden M., Umemoto T., Sato F., 2005, *VizieR Online Data Catalog*, 7244, 0
- Drabek E., Hatchell J., Friberg P., Richer J., Graves S., Buckle J. V., Nutter D., Johnstone D., Di Francesco J., 2012, *MNRAS*, 426, 23
- Drew J. E., Busfield G., Hoare M. G., Murdoch K. A., Nixon C. A., Oudmaijer R. D., 1997, *MNRAS*, 286, 538
- Dunham M. M., Crapsi A., Evans II N. J., Bourke T. L., Huard T. L., Myers P. C., Kauffmann J., 2008, *ApJS*, 179, 249
- Dzib S., Loinard L., Mioduszewski A. J., Boden A. F., Rodríguez L. F., Torres R. M., 2010, *ApJ*, 718, 610
- Dzib S., Loinard L., Mioduszewski A. J., Boden A. F., Rodríguez L. F., Torres R. M., 2011, in *Revista Mexicana de Astronomia y Astrofisica Conference Series* Vol. 40 of *Revista Mexicana de Astronomia y Astrofisica Conference Series*, VLBA astrometry of the AeBe star EC 95 in Serpens. pp 231–232

- Ebert R., 1955, , 37, 217
- Eiroa C., Casali M. M., 1992, A&A, 262, 468
- Eiroa C., Casali M. M., Miranda L. F., Ortiz E., 1994, A&A, 290, 599
- Eiroa C., Djupvik A. A., Casali M. M., 2008, in Reipurth B., ed., , Handbook of Star Forming Regions, Volume II. Monograph, p. 693
- Eiroa C., Torrelles J. M., Curiel S., Djupvik A. A., 2005, AJ, 130, 643
- Enoch M. L., Corder S., Duchêne G., Bock D. C., Bolatto A. D., Culverhouse T. L., Kwon W., Lamb J. W., Leitch E. M., Marrone D. P., Muchovej S. J., Pérez L. M., Scott S. L., Teuben P. J., Wright M. C. H., Zauderer B. A., 2011, ApJS, 195, 21
- Enoch M. L., Corder S., Dunham M. M., Duchêne G., 2009, ApJ, 707, 103
- Enoch M. L., Evans II N. J., Sargent A. I., Glenn J., 2009, ApJ, 692, 973
- Evans II N. J., Allen L. E., Blake G. A., Boogert A. C. A., Bourke T., Harvey P. M., Kessler J. E., Koerner D. W., Lee C. W., Mundy L. G., Myers P. C., Padgett D. L., Pontoppidan K., Sargent A. I., Stapelfeldt K. R., van Dishoeck E. F., Young C. H., Young K. E., 2003, PASP, 115, 965
- Evans N. J. II., Allen L. E., Blake G. A., Boogert A. C. A., Bourke T., Harvey P. M., Kessler J. E., Koerner D. W., Lee C. W., Mundy L. G., Myers P. C., Padgett D. L., Pontoppidan K., Sargent A. I., Stapelfeldt K. R., van Dishoeck E. F., Young C. H., Young K. E., 2003, PASP, 115, 965
- Evans N. J. II., Dunham M. M., Jørgensen J. K., Enoch M. L., Merín B., van Dishoeck E. F., Alcalá J. M., Myers P. C., Stapelfeldt K. R., 2009, ApJS, 181, 321
- Evans N. J. II., Harvey P. M., Dunham M., Huard T., Mundy L., Lai S.-p., Chapman N., Brooke T., Enoch M., Stapelfeldt K., 2007, Technical report, Final Delivery of Data from the c2d Legacy Project: IRAC and MIPS. Spitzer Science Center, Pasadena, CA
- Fazio G. G., Hora J. L., Allen L. E., Ashby M. L. N., Barmby P., Deutsch L. K., Huang J.-S., Kleiner S., 2004, ApJS, 154, 10
- Fich M., Dahl G. P., Treffers R. R., 1990, AJ, 99, 622
- Font A. S., Mitchell G. F., Sandell G., 2001, ApJ, 555, 950
- Fuente A., Martín-Pintado J., Bachiller R., Rodríguez-Franco A., Palla F., 2002, A&A, 387, 977
- Gordon M. A., 1995, A&A, 301, 853
- Graves S. F., Richer J. S., Buckle J. V., Duarte-Cabral A., Fuller G. A., Hogerheijde M. R., Owen J. E., Brunt C., 2010, MNRAS, 409, 1412
- Greene T. P., Wilking B. A., Andre P., Young E. T., Lada C. J., 1994, ApJ, 434, 614

- Greenstein J. L., 1973, ApJL, 184, L23
- Gutermuth R. A., Bourke T. L., Allen L. E., Myers P. C., Megeath S. T., Matthews B. C., Jørgensen J. K., Di Francesco J., Ward-Thompson D., Huard T. L., Brooke T. Y., Dunham M. M., Cieza L. A., Harvey P. M., Chapman N. L., 2008, ApJL, 673, L151
- Gutermuth R. A., Megeath S. T., Myers P. C., Allen L. E., Pipher J. L., Fazio G. G., 2009, ApJS, 184, 18
- Habart E., Testi L., Natta A., Vanzi L., 2003, A&A, 400, 575
- Harvey P., Merín B., Huard T. L., Rebull L. M., Chapman N., Evans II N. J., Myers P. C., 2007, ApJ, 663, 1149
- Harvey P. M., Huard T. L., Jørgensen J. K., Gutermuth R. A., Mamajek E. E., Bourke T. L., Merín B., Cieza L., Brooke T., Chapman N., Alcalá J. M., Allen L. E., Evans II N. J., Di Francesco J., Kirk J. M., 2008, ApJ, 680, 495
- Harvey P. M., Thronson Jr. H. A., Gatley I., 1979, ApJ, 231, 115
- Hatchell J., Dunham M. M., 2009, A&A, 502, 139
- Hatchell J., Fuller G. A., Richer J. S., 2007, A&A, 472, 187
- Hatchell J., Fuller G. A., Richer J. S., Harries T. J., Ladd E. F., 2007, A&A, 468, 1009
- Hatchell J., Richer J. S., Fuller G. A., Qualtrough C. J., Ladd E. F., Chandler C. J., 2005, A&A, 440, 151
- Hatchell J., Terebey S., Huard T., Mamajek E. E., Allen L., Bourke T. L., Dunham M. M., Gutermuth R., Harvey P. M., Jørgensen J. K., Merín B., Noriega-Crespo A., Peterson D. E., 2012, ApJ, 754, 104
- Hatchell J., Wilson T., Drabek E., Curtis E., Richer J., Nutter D., Di Francesco J., Ward-Thompson D., JCMT GBS Consortium 2013, MNRAS, 429, L10
- Hennebelle P., Chabrier G., 2011, ApJL, 743, L29
- Henning T., Sablotny R. M., 1995, Advances in Space Research, 16, 17
- Herbig G. H., 1960, ApJS, 4, 337
- Hernández J., Calvet N., Briceño C., Hartmann L., Berlind P., 2004, AJ, 127, 1682
- Hildebrand R. H., 1983, QJRAS, 24, 267
- Hillenbrand L. A., Strom S. E., Vrba F. J., Keene J., 1992, ApJ, 397, 613

- Holland W., MacIntosh M., Fairley A., Kelly D., Montgomery D., Gostick D., Atad-Ettedgui E., Ellis M., Robson I., Hollister M., Woodcraft A., 2006, in Society of Photo-Optical Instrumentation Engineers (SPIE) Conference Series Vol. 6275 of Society of Photo-Optical Instrumentation Engineers (SPIE) Conference Series, SCUBA-2: a 10,000-pixel submillimeter camera for the James Clerk Maxwell Telescope
- Holland W. S., Bintley D., Chapin E. L., Chrysostomou A., Davis G. R., Dempsey J. T., Duncan W. D., Fich M., Friberg P., Halpern M., Irwin K. D., Jenness T., Kelly B. D., MacIntosh M. J., Robson E. I., 2013, MNRAS, 430, 2513
- Huttemeister S., Wilson T. L., Henkel C., Mauersberger R., 1993, A&A, 276, 445
- Jeans J. H., 1902, Royal Society of London Philosophical Transactions Series A, 199, 1
- Jenness T., Chapin E. L., Berry D. S., Gibb A. G., Tilanus R. P. J., Balfour J., Tilanus V., Currie M. J., , 2013, SMURF: SubMillimeter User Reduction Facility
- Jenness T., Currie M. J., Tilanus R. P. J., Cavanagh B., Berry D. S., Leech J., Rizzi L., 2015, MNRAS, 453, 73
- Johnstone D., Boonman A. M. S., van Dishoeck E. F., 2003, A&A, 412, 157
- Johnstone D., Wilson C. D., Moriarty-Schieven G., Joncas G., Smith G., Gregersen E., Fich M., 2000, ApJ, 545, 327
- Juvela M., Ristorcelli I., Pelkonen V.-M., Marshall D. J., Montier L. A., Bernard J.-P., Paladini R., Lunttila T., 2011, A&A, 527, A111
- Kaas A. A., Olofsson G., bontemps S., André P., Nordh L., Huldtgren M., Prusti T., Persi P., Delgado A. J., Motte F., Abergel A., 2004, A&A, 421, 623
- Kauffmann J., Bertoldi F., Bourke T. L., Evans II N. J., Lee C. W., 2008, A&A, 487, 993
- Kirk H., Johnstone D., Di Francesco J., 2006, ApJ, 646, 1009
- Kirk J. M., Ward-Thompson D., Di Francesco J., Bourke T. L., Evans N. J., Merín B., Allen L. E., Cieza L. A., Dunham M. M., Harvey P., Huard T., Jørgensen J. K., Miller J. F., Noriega-Crespo A., Peterson D., Ray T. P., Rebull L. M., 2009, ApJS, 185, 198
- Koenig X. P., Allen L. E., Gutermuth R. A., Hora J. L., Brunt C. M., Muzerolle J., 2008, ApJ, 688, 1142
- Konyves V., Andre P., Men'shchikov A., Palmeirim P., Arzoumanian D., Schneider N., Roy A., Didelon P., Maury A., Shimajiri Y., Di Francesco J., Bontemps S., Peretto N., Benedettini M., 2015, ArXiv e-prints
- Könyves V., André P., Men'shchikov A., Schneider N., Arzoumanian D., Bontemps S., Attard M., Motte F., Didelon P., 2010, A&A, 518, L106

- Kraemer K. E., Jackson J. M., Kassis M., Deutsch L. K., Hora J. L., Simon R., Hoffmann W. F., Fazio G. G., Dayal A., Bania T. M., Clemens D. P., Heyer M. H., 2003, ApJ, 588, 918
- Kuhn M. A., Getman K. V., Feigelson E. D., Reipurth B., Rodney S. A., Garmire G. P., 2010, ApJ, 725, 2485
- Kurtz S., 2005, in Cesaroni R., Felli M., Churchwell E., Walmsley M., eds, Massive Star Birth: A Crossroads of Astrophysics Vol. 227 of IAU Symposium, Hypercompact HII regions. pp 111–119
- Kurtz S., Churchwell E., Wood D. O. S., 1994, ApJS, 91, 659
- Lada C. J., Wilking B. A., 1984, ApJ, 287, 610
- Ladd E. F., Myers P. C., Goodman A. A., 1994, ApJ, 433, 117
- Lefloch B., Lazareff B., 1994, A&A, 289, 559
- Mairs S., Johnstone D., Offner S. S. R., Schnee S., 2014, ApJ, 783, 60
- Malbet F., Benisty M., de Wit W.-J., Kraus S., Meilland A., Millour F., Tatulli E., Berger J.-P., Chesneau O., Hofmann K.-H., Isella A., Natta A., Petrov R. G., Preibisch T., Stee P., Testi L., Weigelt G., Antonelli P., Beckmann U., 2007, A&A, 464, 43
- Mallick K. K., Kumar M. S. N., Ojha D. K., Bachiller R., Samal M. R., Pirogov L., 2013, ApJ, 779, 113
- Mannings V., 1994, MNRAS, 271, 587
- Manoj P., Ho P. T. P., Ohashi N., Zhang Q., Hasegawa T., Chen H.-R., Bhatt H. C., Ashok N. M., 2007, ApJL, 667, L187
- Mathis J. S., Mezger P. G., Panagia N., 1983, A&A, 128, 212
- Matzner C. D., 2002, ApJ, 566, 302
- Maury A. J., André P., Men'shchikov A., Könyves V., Bontemps S., 2011, A&A, 535, A77
- McKee C. F., Tan J. C., 2003, ApJ, 585, 850
- McMullin J. P., Mundy L. G., Blake G. A., Wilking B. A., Mangum J. G., Latter W. B., 2000, ApJ, 536, 845
- Men'shchikov A., André P., Didelon P., Könyves V., Schneider N., Motte F., Bontemps S., Arzoumanian D., Attard M., Abergel A., Baluteau J.-P., Bernard J.-P., Cambrésy L., 2010, A&A, 518, L103
- Mezger P. G., Henderson A. P., 1967, ApJ, 147, 471
- Mitchell G. F., Johnstone D., Moriarty-Schieven G., Fich M., Tothill N. F. H., 2001, ApJ, 556, 215

- Molinari S., Brand J., Cesaroni R., Palla F., Palumbo G. G. C., 1998, A&A, 336, 339
- Motte F., Andre P., Neri R., 1998, A&A, 336, 150
- Myers P. C., Adams F. C., Chen H., Schaff E., 1998, ApJ, 492, 703
- Myers P. C., Ladd E. F., 1993, ApJL, 413, L47
- Natta A., Prusti T., Neri R., Wooden D., Grinin V. P., Mannings V., 2001, A&A, 371, 186
- Nutter D., Ward-Thompson D., 2007, MNRAS, 374, 1413
- Offner S. S. R., Klein R. I., McKee C. F., Krumholz M. R., 2009, ApJ, 703, 131
- Olnon F. M., 1975, A&A, 39, 217
- Ossenkopf V., Henning T., 1994, A&A, 291, 943
- Oster L., 1961, ApJ, 134, 1010
- Panagia N., Felli M., 1975, A&A, 39, 1
- Pattle K., Ward-Thompson D., Kirk J. M., White G. J., Drabek-Maunder E., 2015, MNRAS, 450, 1094
- Persi P., Palagi F., Felli M., 1994, A&A, 291, 577
- Peterson D. E., Caratti o Garatti A., Bourke T. L., Forbrich J., Gutermuth R. A., Jørgensen J. K., Allen L. E., Patten B. M., Dunham M. M., Harvey P. M., Merín B., Chapman N. L., Cieza L. A., Huard T. L., Knez C., Prager B., Evans N. J., 2011, ApJS, 194, 43
- Pilbratt G. L., Riedinger J. R., Passvogel T., Crone G., Doyle D., Gageur U., Heras A. M., Jewell C., Metcalfe L., Ott S., Schmidt M., 2010, A&A, 518, L1
- Pirogov L., Ojha D. K., Thomasson M., Wu Y.-F., Zinchenko I., 2013, MNRAS, 436, 3186
- Pontoppidan K. M., Dullemond C. P., Blake G. A., Boogert A. C. A., van Dishoeck E. F., Evans II N. J., Kessler-Silacci J., Lahuis F., 2007, ApJ, 656, 980
- Pontoppidan K. M., Dullemond C. P., Blake G. A., Evans II N. J., Geers V. C., Harvey P. M., Spiesman W., 2007, ApJ, 656, 991
- Preibisch T., 2003, A&A, 410, 951
- Racine R., 1968, AJ, 73, 233
- Reid M. A., Wilson C. D., 2005, ApJ, 625, 891
- Reynolds S. P., 1986, ApJ, 304, 713
- Ridge N. A., Wilson T. L., Megeath S. T., Allen L. E., Myers P. C., 2003, AJ, 126, 286

- Rieke G. H., Young E. T., Engelbracht C. W., Kelly D. M., Low F. J., Haller E. E., Beeman J. W., 2004, ApJS, 154, 25
- Robitaille T. P., Whitney B. A., Indebetouw R., Wood K., 2007, ApJS, 169, 328
- Rodney S. A., Reipurth B., 2008, The W40 Cloud Complex. p. 683
- Rodríguez L. F., Rodney S. A., Reipurth B., 2010, AJ, 140, 968
- Rodríguez L. F., Zapata L. A., Dzib S. A., Ortiz-León G. N., Loinard L., Macías E., Anglada G., 2014, ApJL, 793, L21
- Röser S., Schilbach E., Schwan H., Kharchenko N. V., Piskunov A. E., Scholz R.-D., 2008, A&A, 488, 401
- Rosolowsky E., Leroy A., 2006, PASP, 118, 590
- Rosolowsky E. W., Pineda J. E., Foster J. B., Borkin M. A., Kauffmann J., Caselli P., Myers P. C., Goodman A. A., 2008, ApJS, 175, 509
- Rumble D., Hatchell J., Gutermuth R. A., Kirk H., Buckle J., Beaulieu S. F., Berry D. S., Broekhoven-Fiene H., 2015, MNRAS, 448, 1551
- Rygl K. L. J., Benedettini M., Schisano E., Elia D., Molinari S., Pezzuto S., André P., Bernard J. P., White G. J., Polychroni D., Bontemps S., Cox N. L. J., Di Francesco J., 2013, A&A, 549, L1
- Sadavoy S. I., Di Francesco J., André P., Pezzuto S., Bernard J.-P., Maury A., Men'shchikov A., Motte F., 2014, ApJL, 787, L18
- Sadavoy S. I., Di Francesco J., Bontemps S., Megeath S. T., Rebull L. M., Allgaier E., Carey S., Gutermuth R., Hora J., Huard T., McCabe C.-E., Muñoz-Crespo A., Padgett D., Terebey S., 2010, ApJ, 710, 1247
- Sadavoy S. I., Di Francesco J., Johnstone D., Currie M. J., Drabek E., Hatchell J., Nutter D., André P., Arzoumanian D., Benedettini M., 2013, ApJ, 767, 126
- Salji C., 2014, in Protostars and Planets VI Posters Filament identification and characterisation in Gould Belt Clouds. p. 19
- Sandell G., Weintraub D. A., Hamidouche M., 2011, ApJ, 727, 26
- Schnee S., Mason B., Di Francesco J., Friesen R., Li D., Sadavoy S., Stanke T., 2014, MNRAS, 444, 2303
- Schnee S. L., Ridge N. A., Goodman A. A., Li J. G., 2005, ApJ, 634, 442
- Sharpless S., 1959, ApJS, 4, 257

- Shimoikura T., Dobashi K., Nakamura F., Hara C., Tanaka T., Shimajiri Y., Sugitani K., Kawabe R., 2015, *ApJ*, 806, 201
- Shirley Y. L., Evans II N. J., Rawlings J. M. C., 2002, *ApJ*, 575, 337
- Shirley Y. L., Evans II N. J., Rawlings J. M. C., Gregersen E. M., 2000, *ApJS*, 131, 249
- Shuping R. Y., Vacca W. D., Kassis M., Yu K. C., 2012, *AJ*, 144, 116
- Skinner S. L., Brown A., Stewart R. T., 1993, *ApJS*, 87, 217
- Smith J., Bentley A., Castelaz M., Gehrz R. D., Grasdalen G. L., Hackwell J. A., 1985, *ApJ*, 291, 571
- Spezzi L., Vernazza P., Merín B., Allen L. E., Evans II N. J., Jørgensen J. K., Bourke T. L., Cieza L. A., Dunham M. M., Harvey P. M., Huard T. L., Peterson D., Tothill N. F. H., The Gould's Belt Team 2011, *ApJ*, 730, 65
- Straizys V., Černis K., Bartašiūtė S., 2003, *A&A*, 405, 585
- Strom S. E., Grasdalen G. L., Strom K. M., 1974, *ApJ*, 191, 111
- Stutz A., Launhardt R., Linz H., Krause O., Henning T., Kainulainen J., Nielbock M., Steinacker J., André P., 2010, *A&A*, 518, L87
- Szymczak M., Hrynek G., Kus A. J., 2000, *A&AS*, 143, 269
- Tafoya D., Gómez Y., Rodríguez L. F., 2004, *ApJ*, 610, 827
- Thompson M. A., White G. J., Morgan L. K., Miao J., Fridlund C. V. M., Huldtgren-White M., 2004, *A&A*, 414, 1017
- Tothill N. F. H., White G. J., Matthews H. E., McCutcheon W. H., McCaughrean M. J., Kenworthy M. A., 2002, *ApJ*, 580, 285
- Ubach C., Maddison S. T., Wright C. M., Wilner D. J., Lommen D. J. P., Koribalski B., 2012, *MNRAS*, 425, 3137
- Urquhart J. S., Morgan L. K., Thompson M. A., 2009, *A&A*, 497, 789
- Vallee J. P., 1987, *A&A*, 178, 237
- Vallee J. P., MacLeod J. M., 1991, *A&A*, 250, 143
- van der Wiel M. H. D., Naylor D. A., Kamp I., Ménard F., Thi W.-F., Woitke P., Olofsson G., Pontoppidan K. M., Di Francesco J., Glauser A. M., Greaves J. S., Ivison R. J., 2014, *MNRAS*, 444, 3911
- Vink J. S., O'Neill P. M., Els S. G., Drew J. E., 2005, *A&A*, 438, L21
- Visser A. E., Richer J. S., Chandler C. J., 2002, *AJ*, 124, 2756

- Walsh A. J., Burton M. G., Hyland A. R., Robinson G., 1998, MNRAS, 301, 640
- Wang Y., Wu Y., Zhang Q., Mao R.-Q., Miller M., 2007, A&A, 461, 197
- Ward-Thompson D., Di Francesco J., Hatchell J., Hogerheijde M. R., Nutter D., Bastien P., Basu S., Bonnell I., Bowey J., Brunt C., Buckle J., 2007, PASP, 119, 855
- Ward-Thompson D., Pattle K., Kirk J. M., André P., Di Francesco J., 2015, ArXiv e-prints
- Watson M., 2010, MSc thesis, University of Hertfordshire.
- White G. J., Casali M. M., Eiroa C., 1995, A&A, 298, 594
- Williams J.P. Myers P., 2000, ApJ, 537
- Winston E., Megeath S. T., Wolk S. J., Muzerolle J., Gutermuth R., Hora J. L., Allen L. E., Spitzbart B., Myers P., Fazio G. G., 2007, ApJ, 669, 493
- Wood D. O. S., Churchwell E., 1989, ApJS, 69, 831
- Wood D. O. S., Myers P. C., Daugherty D. A., 1994, ApJS, 95, 457
- Wright A. E., Barlow M. J., 1975, MNRAS, 170, 41
- Wu Y., Zhang Q., Yu W., Miller M., Mao R., Sun K., Wang Y., 2006, A&A, 450, 607
- Yorke H. W., Tenorio-Tagle G., Bodenheimer P., Rozyczka M., 1989, A&A, 216, 207
- Young C. H., Shirley Y. L., Evans II N. J., Rawlings J. M. C., 2003, ApJS, 145, 111
- Young K. E., Harvey P. M., Brooke T. Y., Chapman N., Kauffmann J., Bertoldi F., Lai S.-P., Alcalá J., Bourke T. L., Spiesman W., Allen L. E., Blake G. A., Evans II N. J., 2005, ApJ, 628, 283
- Zacharias M., Zacharias N., 2012, in IAU Joint Discussion Vol. 7 of IAU Joint Discussion, Radio-optical reference frame offsets from CTIO and UCAC4 data. p. 13P
- Zacharias N., Finch C. T., Girard T. M., Henden A., Bartlett J. L., Monet D. G., Zacharias M. I., 2013, AJ, 145, 44
- Zelik II M., Lada C. J., 1978, ApJ, 222, 896
- Zhang C. Y., Laureijs R. J., Clark F. O., 1988, A&A, 196, 236
- Zhu L., Wu Y.-F., Wei Y., 2006, , 6, 61
- Ziener R., Eisloffel J., 1999, A&A, 347, 565